Water Wave Scattering by Floating Elastic Plates with Application to Sea-Ice

This thesis is for examination purposes only and may not be consulted or referred to by any persons other than the examiner.

Alison L. Kohout
November 2008

Supervised by
Dr. Michael H. Meylan

A thesis submitted for the degree of
Doctor of Philosophy in Mathematics
at the University of Auckland, New Zealand

Abstract

This thesis considers the scattering of small amplitude water waves, obliquely incident on a set of floating elastic plates occupying the entire water surface. The problem is two-dimensional and assumes invariance in the width of the plates. All non-linear physical effects are neglected. The plates are floating on a body of water of finite depth and each plate has uniquely defined properties. The problem is formulated by imposing boundary conditions on the eigenfunction expansion of Laplace's equation. A set of transmission and reflection coefficients is generated, which is solved by applying the edge conditions and matching at each plate boundary. We label this solution method the Matched Eigenfunction Expansion Method (MEEM). The problem is solved for a variety of edge conditions including free, clamped, sliding, springed and hinged. To verify the MEEM results, the problem is also solved using a Green Function Method. The convergence of the two methods is compared and found to be almost identical. The MEEM is used to simulate wave–ice interaction in the Marginal Ice Zone (MIZ). The model removes the resonance effects and predicts that the transmitted energy is independent of floe length, provided the wavelength is more than three times the floe length. The model predicts an exponential decay of wave energy with distance of propagation through the MIZ, which agrees with experimental findings. The results have been summarised in a graph with the attenuation coefficient expressed as a function of period for various floe thicknesses. We also provide an estimate of the attenuation coefficient using an approximation theory. The displacements of the MEEM are compared against a series of laboratory experiments performed in a two-dimensional wave-tank and show good agreement. The attenuation model results are compared against a series of field experiments carried out in the Arctic and off the West Antarctic Peninsula. Generally, the decay rates of the model agree well with the field experiments in diffuse ice. We suggest that factors other than wave scatter are relevant in models of wave-attenuation in non-diffuse ice.

Acknowledgements

Many people have helped make this thesis possible. Firstly, and most importantly, I would like to thank my supervisor, Mike Meylan. Mike has proved to be a fantastic mentor whose expertise and encouragement have played a vital role in making this thesis run smoothly and enjoyably. Mike has been a committed supervisor, who throughout the last three years has put in a considerable amount of effort and has been very generous with his time.

A vital section of this thesis has relied on experimental and field data. I would like to thank Shigeki Sakai and his team for their work on the wave-tank experimental data. I would also like to thank Will Perrie and Daniel Hayes for providing us with their field data.

The development of the code used in this thesis was assisted by Pierre Leman, Damien Brossard and Tim Williams. I would further like to thank the Otago team including Vernon Squire, Tim Williams, Gareth Vaughan and Pat Langehorne for their time and valuable advice throughout this thesis. Towards the end of the thesis, Malte also proved to be invaluable in providing advice and I greatly appreciate his efforts in the arduous task of proof reading my thesis. I would also like to acknowledge Garry Tee for his valuable assistance proof reading our papers.

Throughout my PhD, I have been heavily reliant on my PhD Scholarship, which was funded by Marsden Grant U00308 from the New Zealand government. This has covered my PhD fees and living expenses. I have also been fortunate during my PhD and have had the opportunity to travel to both local and international conferences and workshops. This has been possible thanks to the financial support from the Auckland University Department of Mathematics, the Auckland University Research Fund, the New Zealand Study Abroad Award and Svalbard University.

Last, but certainly not least, I would like to thank my family and my partner Chris for their invaluable support in many ways throughout this PhD.

Contents

List of Figures

List of Tables

Nomenclature

a	Attenuation coefficient 90
$\breve{a}$	Attenuation coefficient from field Experiments 120
$\tilde{a}$	Approximated attenuation coefficient 108
A	Wave amplitude 99
α	Frequency squared 23
β	Stiffness constant 23
$\mathcal{C}$	Term appearing in the Green's Function 48
C	Concentration of ice 120
CI	Confidence Interval 121
D	Rigidity constant 20
$\mathcal{D}$	Energy balance coefficient 72
E	Transmitted energy 80
η	Displacement 18
η^s	Shallow water displacement 42
η^I	Incident displacement 50
$\eta^+(x'_n)$	Right edge of the n^{th} discontinuity 65
$\eta^-(x'_n)$	Left edge of the n^{th} discontinuity 65
f	Rayleigh's distribution 82
g	Gravitational constant 19
G	Free-Surface Green Function for a floating elastic plate 47
$\mathcal{G}$	Simplifying term in the Green Function 50
GFM	Green Function Method 1
γ	Mass constant 22
H_s	Significant wave height 102
ω	Frequency 18
h	Water depth 18
I	Incident wave amplitude in potential 28
$\Im$	The imaginary part of a complex number 72
k	Wave number in the z direction 26
κ	Wave number in the x direction 26
k_y	Wave number in the y direction 18
k^f	Free surface wave number in the z direction 27

1
Introduction

The study of linear wave propagation through a region of water containing floating elastic plates has been the subject of significant research. In this thesis, we consider wave scatter under a set of plates, each with unique (but constant) properties and floating on a body of water of arbitrary finite depth. The problem is formulated by imposing boundary conditions on the eigenfunction expansion of Laplace's equation. The wave modes are generated by solving the dispersion equation, which is derived from the boundary conditions. A set of transmission and reflection coefficients is generated, which is solved by applying the plate edge conditions and matching the velocity potential and its derivatives at each plate boundary. Throughout this thesis, we label this solution method the Matched Eigenfunction Expansion Method (MEEM). To verify the MEEM, the problem is also solved via a Green Function Method (GFM), which is computationally more efficient but can only solve for plates of constant rigidity.

The original motivation for this study was to understand wave propagation in ice-covered seas. Large plates of floating ice are found in polar regions. This sea-ice plays a key role in driving the world's oceanic circulatory system and hence the world's climatic system. It also harbours an entire ecosystem and its existence has a large impact on the survival of many species. Sea-ice is highly influenced by the surrounding ocean and its dynamic and unrelenting nature, and is constantly moving, breaking and re-forming. Our global

climate is changing. A warmer climate in the Arctic is melting sea-ice and reducing its extent. Further warming will intensify storm activity and hence increase wave energy and its penetration into sea-ice, which will potentially increase floe breakup and further reduce sea-ice extent.

Interest in understanding wave–ice interaction began towards the end of the nineteenth century. Due to the remoteness of the study area, wave–ice related field studies have always been logistically challenging and expensive, and the available experimental data is limited in quality and quantity. There however have been useful measurements of wave-attenuation through sea-ice. Unfortunately, significant work is required for the most sophisticated three-dimensional wave–ice models to reach a point where predictions of wave-attenuation are possible and such predictions require large computational resources, so that no summary of the attenuation coefficient as a function of various parameters has been possible. One of the aims of this study is to simulate wave scatter through sea-ice, using our simplified but flexible two-dimensional (one vertical and one horizontal) solution. This solution is compared against laboratory experiments, and is also used to model wave-attenuation which is compared to experimental data.

The study of wave interaction with floating plates can also be applied to the construction of very large floating structures. Our world has a growing population and a corresponding expansion of urban development in land-scarce countries. Engineers have proposed the construction of very large floating structures, which involves connecting a series of floating plates, for industrial space, airports, storage facilities and even habitation. By allowing for articulated plates, our two-dimensional solution can be applied to these very large floating structures.

We begin this thesis by providing some background information on this research field. The importance of sea-ice, models of wave–ice interaction and the attenuation of waves through ice are discussed. We also discuss strain within an ice floe and floe breakup. The research surrounding man-made very large floating structures is also briefly covered. In Chapter 3, we introduce the assumptions, boundary conditions and formulation of the two-dimensional problem. Chapter 4 deals with a mathematical explanation of the MEEM. To ease into the final solution, we begin by solving for two semi-infinite plates which leads onto solving for a set of plates. In Chapter 5, we use the GFM to solve for a large homogeneous plate with multiple cracks. We include this method as it is a useful tool to verify the results of the MEEM. In Chapter 6, we solve for various cases of articulated plates, which have many applications including engineering problems asso-

ciated with very large floating structures. The accuracy and efficiency of the solutions is considered in Chapter 7. We check that the system is in energy balance and compare the MEEM with the GFM and a finite-floe model. In Chapter 8, we use the MEEM to simulate an idealised Marginal Ice Zone and produce a wave attenuation model. In Chapter 9, an approximation theory is derived which estimates the wave-attenuation, using only the reflected and transmitted waves from a wave travelling from open water into a semi-infinite plate. In Chapter 10, we test our theory and models against wave-tank and field experiments. In our final chapter we summarise and conclude the thesis.

2
Background

2.1 Sea-Ice and the Marginal Ice Zone (MIZ)

Sea-ice surrounds the poles of our planet and occupies about 7% of the total area of the world's oceans (Wadhams, 2000). These ice-covered seas represent the cold end of the enormous heat engine which enables our planet to sustain temperatures suitable for human life. Sea-ice creates a barrier between the ocean and the atmosphere and prevents the transfer of heat and gases across the interface. Water has a high heat capacity, and without a barrier can transfer a large amount of heat to the polar atmosphere. When sea-ice is present, the atmosphere can cool by up to 30°C (Ruddiman, 2001). Sea-ice also has a strong impact on the albedo and reflects up to 80% solar radiation while water only reflects 10% (Wadhams, 2000). Increasing the sea-ice extent, increases the albedo which decreases the absorbed heat and increases cooling. Satellite data from 1979 to 2007, has shown that the sea-ice area and extent in the Arctic is retreating by 10% - 11% per decade (Comiso et al., 2008). It is unknown whether Arctic summer sea-ice will even exist in years to come. Sea-ice also has an influence on the ocean circulation system. The formation of sea-ice creates salty dense water which sinks and carries oxygen and dissolved carbon dioxide to the ocean depths. These convection regions drive a three-dimensional global pattern of deep and shallow currents which spread nutrient and oxygen rich waters

throughout the globe (Wadhams, 2000). Sea-ice also plays a major role in supporting polar marine ecosystems. Several species of copepods, amphipods and two species of krill have adapted to life in close association with sea-ice, where they feed on ice algae and seek shelter from predators. It is these organisms and their predators that are being affected most by warming (Smetacek and Nicol, 2005).

The interfacial region between the open ocean and the ice-covered seas is known as the Marginal Ice Zone (MIZ). This region consists of neither open ocean, nor frozen ocean, but consists of a patchwork of ice floes and open water. The MIZ is a dynamic and at times turbulent region, which is formed by wave-induced breaking of continuous ice. This process is balanced by wave scatter within the MIZ which partially shields the continuous ice from the destructive wave energy. There are two aspects which need to be understood to model this process: the first is the wave-induced breaking of the continuous ice, and the second is the wave scattering in the MIZ (Squire et al., 1995). The greatest amount of breakup, and thus the smallest floes, are found closest to the ice edge. If the wind is blowing towards the ice edge from the open sea, it compresses the MIZ and produces a compact ice field. If the wind is blowing away from the ice edge, most of the MIZ becomes diffuse. The outermost edge can sometimes organise itself into a series of compact ice edge bands which are separated by completely open water and lie with their long axes roughly perpendicular to the wind. In winter, new ice can form in these open water bands (Wadhams, 2000). The four major MIZ regions of the world are located in the Greenland Sea, Labrador Sea, Bering Sea and circumpolar Antarctic ice edge.

2.2 Wave–Ice Modelling

It is a well known fact that sea-ice has the effect of reducing incoming swell. The distance at which waves are found to penetrate into ice varies considerably. Modelling this process requires understanding of the physical processes involved in wave-attenuation. In this section, we summarise some of the wave–ice modelling techniques to date. We begin by briefly introducing some of the early concepts and research techniques. Following this we discuss in some detail wave scatter modelling, which is applicable to diffuse ice fields and is the focus of this thesis. Various solution methods and problems are discussed. Finally, we briefly discuss viscous models which are applicable to compact ice fields. A review of the interaction between waves and ice is summarised in Squire et al. (1995) and Squire (2007).

2.2.1 Early Findings

As early as 1887, scientists developed an interest in understanding waves and how they interact with floating ice; Greenhill (1887) found an expression for the velocity of waves through ice where the ice sheet is modelled as a thin elastic beam. During the 1930's and 50's, Greenhill's ideas were developed through a series of field experiments and analyses (Roethlisberger, 1972). Waves were artificially generated by detonation blasts, and the elastic and flexural ice-coupled wave propagation in ice of various types was studied, where the ice was treated as a plate rather than a beam. The artificial waves were also used to measure the Young's modulus of ice. During the 50's, the theoretical aspect of wave propagation through ice was also studied. Keller and Weitz (1953) focused on the boundary value problem at the ice edge and the calculation of the transmission and reflection coefficients. Here the ice is treated as a floating material of uniform surface density with no elastic properties nor viscosity. This problem is solved completely and the solution method may be particularly useful in modelling wave propagation through frazil or pancake ice. During a voyage, Robin (1963) confirmed visually that ice floes bend. It has consequently become standard to model ice floes as thin elastic plates.

2.2.2 Scattering Models

For ice conditions consisting of discrete solitary floes, it has been assumed that the major physical factor influencing wave-attenuation is the redistribution of wave energy due to scattering by the floes (Squire et al., 1995). Within each floe, energy propagates with an altered dispersion relation. The ice floe therefore scatters incoming ocean wave energy due to a mismatched mode of propagation between each plate (Squire et al., 1995). This scattering energy generates an energy reflection and transmission wave.

Solitary plates and two semi-infinite plates

Initially the problem of wave scatter through floating elastic plates, was solved for two semi-infinite plates with identical properties. Kouzov (1963) solved this problem explicitly using the Riemann–Hilbert technique. More recently this problem has been reconsidered by Squire and Dixon (2000) and Williams and Squire (2002), who solve it using a Green Function method. Their method is applicable to infinitely deep water and they extend the problem to oblique wave incidence.

A more challenging problem involves solving for two semi-infinite plates with arbitrary properties. The first significant work on this problem was done by Evans and Davies

(1968), who presented a solution method for evaluating the transmission and reflection of waves, propagating from a semi-infinite region of open water into a semi-infinite region of a floating elastic plate. The method of solution was based on the Wiener–Hopf technique. Evans and Davies (1968), however, only solved explicitly for the case of shallow water. They presented only the formulation for the finite-depth case, as they were unable to compute the transmission and reflection coefficients. Wadhams (1986) presents an alternative method (the eigenfunction expansion method), which he developed in the early 1970's. It was the first based on a solution for a single finite-floe surrounded by water. Unfortunately, no numerical method to solve the problem for a single floe had been developed at the time, and the reflection and transmission coefficients were only derived approximately, as only a subset of the evanescent waves were included. Fox and Squire (1994) returned to the problem of a wave propagating from a semi-infinite region of open water into a semi-infinite region covered by a floating elastic plate. Their method is derived from the work of Wadhams (1986) and they extend by matching along the entire water column at the plate edge and solve for oblique incidence. Soon after, Barrett and Squire (1996) extended the solution of Fox and Squire (1994) to two plates of arbitrary properties. Meylan and Squire (1994) solve for a single ice floe using dry mode eigenfunctions to construct a Green function for the plate and used a second Green function for the water. A Fredholm integral equation is assembled for the velocity potential at the surface which is solved using the Nystrom method. Recently, the computational difficulties associated with the Wiener–Hopf solution of Evans and Davies (1968) have been overcome and solved explicitly by several authors, including Balmforth and Craster (1999); Chakrabarti (2000); Tkacheva (2001); Chung and Fox (2002). Chung and Linton (2005) have also solved the problem of open water and a semi-infinite plate using the residue calculus technique, a method which is closely related to the Wiener–Hopf method.

Attention has also been focused towards constructing physically more realistic ice sheets such as solving for pressure ridges, open and refrozen leads and sudden or gradual changes in thickness (Porter and Porter, 2004; Williams and Squire, 2004; Chung and Linton, 2005; Gayen et al., 2007). Authors, including Bennetts et al. (2007); Porter and Porter (2004) have incorporated sea-ice draft into their models. Marchenko (1996); Marchenko and Voliak (1997); Vaughan et al. (2007) attempt to estimate floe thickness and other parameters from the wave propagation through real sea-ice terrain using in situ wave data. The three-dimensional floating circular ice floe is solved in Meylan and Squire (1996) via an extension of Meylan and Squire (1994) and Peter et al. (2004) solve for the finite depth case using matched eigenfunctions. Meylan (2002) solves for arbitrary floe shapes where the dry modes are substituted into the integral equation for water to give a linear sys-

tem of equations for the coefficients used to expand the ice floe motion. The modes are determined generally using a finite element approach.

Multiple plates

The next major development in wave scattering theory was in the consideration of wave propagation through multiple plates. Squire and Dixon (2001) extend the single crack problem to a multiple crack problem, in which the semi-infinite regions are separated by a region consisting of a finite number of plates of finite size with all plates having identical properties. Evans and Porter (2003); Porter and Evans (2005) consider the multiple crack problem for finitely-deep water and derive a simple solution. Hermans (2004) also present a solution for multiple plates, based on an earlier solution for a single plate (Hermans, 2003), and is for a set of finite elastic plates of arbitrary properties. Hermans (2004) solves the problem using Green's theorem to obtain an integral equation for the deflection. Ogasawara and Sakai (2006) numerically solve for a set of arbitrary plates using a time-domain solution incorporating the boundary element method and the finite-element method proposed by Liu and Sakai (2002). Bukatov and Bukatov (1999) consider the influence of floating broken ice on the displacement of non-linear surface waves. Sophisticated three-dimensional models have also been developed. (Masson and LeBlond, 1989; Meylan et al., 1997; Meylan and Masson, 2006) couple the solutions for individual ice floes with a transport equation. Also, for a finite number of arbitrary plates, the three-dimensional problem is solved by Peter and Meylan (2004). A number of works consider periodic infinite or semi-infinite arrays. Chou (1998) solves for wave propagation through an infinite array of periodically arranged surface scatterers or plates by an extension of Floquet's Theorem. Wang et al. (2007) solve for an infinite array using a periodic Green function, while Peter et al. (2006) and Peter and Meylan (2007) solve the infinite and semi-infinite array problem respectively using an interaction theory.

In this study, we consider a two-dimensional multiple floating elastic plate solution, which is solved exactly via an extension of Fox and Squire (1994)'s matched eigenfunction expansion method (Kohout et al., 2007). The only physical parameters which are considered are length, mass and elastic stiffness. All non-linear effects, floe collisions and ice-creep are neglected so that the problem is only applicable to discrete floes which are large relative to thickness and non-extreme wave conditions. We consider this simplified model for its flexibility, computational efficiency and as a practical tool to help understand the key physical processes in wave scattering.

2.2.3 Viscous Models

In more compact ice fields, the interactions between floes increase and it may no longer be realistic to consider the ice field as being composed of individual floes (Wadhams, 2000). Instead, floes collide or are held together by the stress of an on-ice wind or by freezing of brash, pancake or frazil ice. Here the ice field is approaching the condition of being a single entity, yet does not possess the bulk property of being a uniform elastic sheet (Wadhams, 2000). It is tempting to ignore the detailed physics of the various energy consuming, ice-water and ice-ice interaction processes and model a material with its sea surface and wave-attenuation properties determined empirically. Weber (1987) was the first to introduce the idea of considering such an ice-cover as a thin, highly viscous fluid. The viscosity is included in the free surface condition as a dampening term. Liu and Mollo-Christensen (1988) describe a physically more realistic model for wave decay which assumes that attenuation is due to the viscous boundary layer under ice. It is assumed that in a highly compact ice-cover, waves disperse as though propagating beneath a thin elastic sheet. An oscillating boundary layer develops under the ice, causing energy loss.

2.3 Wave Attenuation

Experiments have shown that waves attenuate exponentially with distance of propagation through ice, and the attenuation coefficient decreases with increasing wave period. There is evidence of a "rollover", where a trend of decreasing attenuation occurs at periods less than 6-8 s. This rollover may be explained by an increase in energy at short periods due to local generation of waves by wind (Squire and Wadhams, 1985). The point of rollover depends on ice conditions, especially ice thickness (Liu et al., 1991).

There are several factors which influence the attenuation of waves through ice. It is, however, not fully understood what these factors are and how much influence they have. The most influential factor in diffuse ice is thought to be due to wave scatter (Section 2.2.2). In compact ice, viscous losses are thought to have the most influence (Section 2.2.3). According to Shen and Squire (1998), other factors which may be relevant include: the absorption due to hysteresis as floes deform on the passing wave field, the absorption in the water column from processes such as wave breaking and the absorption due to collisions and other interactions between floes. Shen et al. (1998) however find that collisional stresses are only small and McKenna and Crocker (1990) conclude that floe collisions cannot account for the observed decrease in wave energy.

2.3.1 Wave Attenuation Models

Wadhams (1986) was a significant paper, as it showed how to estimate the transmitted energy through a set of floes in terms of the transmitted energy through a single floe, so that an attenuation coefficient could be estimated. The possible paths of each wave vector through the ice field are considered, and the final forward vector summed through all possible multiple reflections. Dixon and Squire (2001) model wave scatter in the Marginal Ice Zone, using the coherent potential approximation to compute the energy transport velocity and derive an attenuation coefficient, which unfortunately does not compare well to experimental results. Liu and Mollo-Christensen (1988) describe a model for wave decay, which assumes attenuation is due to the viscous boundary layer under ice (Section 2.2.3). They parametrise the energy loss by a tuning parameter, the eddy viscosity, which is related to actual flow conditions. Their model agrees well with experimental data. Perrie and Hu (1996) develop a model which is based on Masson and LeBlond (1989)'s model and use a rigid cylindrical floe model (Isaacson, 1982). The scattering model is incorporated into an operational wave model. The model suffers from the requirement that the ice floes be small enough to be modelled as rigid cylinders so that it is only applicable to ice fields with small floes. For the most sophisticated wave–ice models, significant work is required to reach the point where predictions of the attenuation coefficients are possible and such predictions would require large computational resources so that no summary of the attenuation coefficient as a function of various parameters has been possible. It would be interesting to see how Perrie and Hu (1996)'s model would perform using a more sophisticated three-dimensional ice floe model, such as the model of Meylan (2002).

The attenuation model we present in this thesis is also limited, as the only physics considered is the elastic bending of the floes. The numerical values for the wave-attenuation, however, can be determined relatively straightforwardly and without using a tuning parameter (Section 8.6) (Kohout and Meylan, 2008b).

2.3.2 Wave Attenuation Field Experiments

Theory and experiment need to work together to understand complicated geophysical phenomena such as wave–ice interaction. It is important to realise that recently, for wave–ice interaction, there has been much more progress with modelling than with experiments. This is highly unsatisfactory, and from a modeller's perspective we have great need for more experimental results.

Methods

It is not at all surprising that models have surpassed experiments in this field. Scientists have to work in remote locations and contend with some of the world's toughest environmental conditions including freezing air temperatures, icy seas and at times wild winds and turbulent waves. In such conditions, scientists must calculate the wave spectrum simultaneously (or near simultaneously) at constant intervals from the ice edge to deep into the ice zone. The measurements need to be along the direction of the swell and the scientists need to record a thorough analysis of the ice conditions at the time of the experiment. A number of different methods are discussed below.

Early measurements
The first measurements of wave decay in the zone of discrete ice floes near an unconfined ice margin were made by shipborne wave recorder (Robin, 1963) and reported in Wadhams (1979, 1986). Later measurements were made by upward-looking echo sounder from a submerged hovering submarine Wadhams (1972, 1978) and by airborne laser profilometer Wadhams (1975).

Wave buoys
Wave buoys have been the standard instrument for measuring waves for many years. The most recent buoys use ultra-sensitive tiltmeters and novel re-zeroing techniques to autonomously gather wave data. These modern buoys use Iridium satellite communication systems to recover data continuously and to remotely control the instrument. For over two years now, there have been several of these buoys drifting independently and successfully recording wave data. Unfortunately, while these buoys can successfully record many useful properties, they can not record wave-attenuation data. Attaining wave-attenuation data requires deployment of a series of wave buoys along the direction of swell to measure the local wave spectrum. The ice conditions at the time of the experiment, such as floe thickness and size, must also be measured. It is difficult to obtain accurate wave-attenuation data using wave buoys, as it requires extensive logistical support to measure wave properties simultaneously (or near simultaneously), and results can be skewed by changes in the swell conditions during the experiment and difference in the swell direction for different periods or multi-directional swell.

Remote Sensing
Remote sensing can be used to obtain sea-ice information on a continuous basis. Due to their all weather capability, microwave sensors like synthetic aperture radar (SAR) or the

radiometer play an important role in this context. Radiometric systems like the Special Sensor Microwave Imager (SSM/I) (Bjørgo et al., 1997) with a resolution between 10 and 50 km, are mainly used to measure sea-ice coverage and sea-ice type. SAR imagery as acquired by the European Remote Sensing Satellite (ERS), has a resolution of about 20 m and thus allows the study of processes in the MIZ on a smaller scale (Schulz-Stellenfleth and Lehner, 2002). SAR can be used to observe the spatial properties of a wave field in sea-ice (Larouche and Cariou, 1992) and is useful for collecting wave direction information. SAR has been used to examine waves propagating through pancake ice fields (Wadhams et al., 2002) and to estimate pancake ice thickness (Wadhams et al., 2004). Unfortunately, however, the use of SAR has not been found to be practical in measuring wave-attenuation through discrete floes.

Autonomous Underwater Vehicle (AUV)
In these experiments, an upward looking Acoustic Doppler Current Profiler (ADCP) is mounted on an autonomous underwater vehicle (AUV). The AUV is a promising device which can sample at high resolution and can sample a large portion of the MIZ over short time scales (Hayes et al., 2007).

Available Data Sets

Early Data Sets
The wave decay measurements from the 60's and early 70's are available and have been summarised and compared against wave-attenuation theory in Wadhams (1986).

The Scott Polar Research Institution (SPRI) Experiments
The most substantial set of experiments to measure wave-attenuation in the MIZ were carried out by the SPRI in the late 1970's and early 1980's (Squire and Moore, 1980; Wadhams et al., 1986, 1988). During these experiments, a helicopter was used to visit floes at intervals within the ice fields along the major axis of the incoming wave spectrum. At each site a wave buoy was inserted between floes to measure the local wave spectrum. The flexural, heave and surge responses of the experimental floe were measured with accelerometers and strain-meters. A mean thickness of the floes was determined by coring at each of the experimental floes. Floe size distributions along the flight path into the ice were derived from overlapping vertical photographs taken from helicopter. The main sources of experimental error were changes in the swell conditions during the experiment, difficulties in determining the ice floe size distribution and thickness, and difference in the swell direction for different periods or multi-directional swell.

The attenuation coefficients from the experiments in the Greenland Sea in September 1978, September 1979 and July 1983 are given in Wadhams et al. (1988) and are used in this study. We also use the attenuation coefficients from the Bering Sea in March 1979 and February 1983. Unfortunately, due to possible reflection or absorption of waves from the fjords, accurate attenuation coefficients could not be calculated from the 1978 Greenland Sea experiments.

The Labrador Ice Margin Experiment (LIMEX)
Another set of experiments took place off the east coast of Newfoundland, Canada, in 1987 and 1989. These experiments provided synthetic aperture radar (SAR) imagery, wave buoy and ice property data. We attempted to obtain the results of this experiment, but unfortunately were not successful.

The Antarctic Peninsula Experiments
Most recently an experiment took place in the MIZ of Antarctica. Autosub, an Autonomous Underwater Vehicle (AUV), was used to complete four missions west of the Antarctic Peninsula in the Bellinghausen Sea during 22 – 25 March 2003. The Autosub is a promising new device. It is a battery-powered vehicle that follows a pre-programmed course and can travel up to a maximum range of 400 km. In water track mode, the Autosub's navigation frame of reference is the water rather than the seabed, hence for some missions, a mean current caused the sub to drift from the mission plan. Consequently, the line of travel of the sub was not necessarily along the direction of the swell nor at right angles to the ice edge. A thorough study of the ice conditions at the time of the experiments was not conducted; estimations from the ship were made for each mission. Hayes et al. (2007) notes that the attenuation coefficients for waves of period longer than 16 s may be compromised by possible surge response of the vehicle. A detailed description of these experiments can be found in Hayes et al. (2007). The results of these experiments were attained from D. Hayes and are used in this study.

2.4 Strain and Floe Break-up

Incoming waves cause ice floes to bend. If the bending induces sufficient strain, fracture will occur (Squire, 1993). The breaking of large continuous floes and land-fast ice, supplies the MIZ with ice floes and determines the floe size distribution of the MIZ (Langhorne et al., 1998). Observations suggest that cracks initially form within a few tens of metres

on the ice edge and that sea-ice thickness is the principal determinant of crack position. Wavelength appears to play only a secondary role (Squire, 1993). During ocean wave experiments, strain gauges were fixed to the upper surface of sea-ice floes in the Arctic which provided some direct measurements of sea-ice fracturing. Results from these experiments have shown an ice island to fracture at $3\text{x}10^{-5}$ (Goodman et al., 1980) and sea-ice to fracture from $4.4\text{x}10^{-5}$ to $8.5\text{x}10^{-5}$ (Squire and Martin, 1980). Based on a series of experiments carried out in the McMurdo Sound, Antarctica, Langhorne et al. (1998) deduce that sea-ice fatigues when it is cyclically stressed. This fatigue can cause the ice to fracture and breakup at stresses well below its flexural strength. Using these experiments, Langhorne et al. (2001) predict the lifetime of the sea-ice as a function of significant wave height and sea-ice brine fraction. We assume that, in general, if the strain is less than $3\text{x}10^{-5}$, the ice will have an infinite resistance to failure (Squire, 1993; Personal correspondence with T. Haskell).

Fox and Squire (1991) were the first to completely and precisely model the strain in ice due to incoming ocean waves. The model is an extension of their Fox and Squire (1990) matched eigenfunction model, which is also summarised in Fox and Squire (1994), for the solution of the velocity potential. Squire (1993) uses a variation on the Fox and Squire (1991) method and considers wave propagation into a viscoelastic ice sheet. This alters the travelling mode so that it attenuates exponentially by an amount which depends on the magnitude of the viscous damping term, which unfortunately is currently unknown.

In Section 8.7, we define the strain as defined in Fox and Squire (1991) and consider the effects it has on floe breakup for a given wave spectrum.

2.5 Very Large Floating Structures (VLFS)

The study of wave propagation through floating elastic plates can also be applied to the construction of Very Large Floating Structures (VLFS). This has motivated much of the recent research in this field. Our world has a growing population and a corresponding expansion of urban development in land-scarce countries. Engineers have proposed the construction of VLFS for industrial space, airports, storage facilities and habitation (Watanabe et al., 2004). There are many examples of such structures already in place. Japan have constructed a Mega-Float (a VLFS test model for floating airport terminals and airstrips), a floating amusement facility, floating emergency rescue bases and floating oil storage systems. There have been floating bridges built in Japan, Canada, Norway

and the United States. Canada also has a floating heliport and Vietnam a floating Hotel (Watanabe et al., 2004).

VLFS may be classified under two broad categories; the pontoon type and the semi-submersible type. The pontoon type is suited to calm sea conditions and is usually associated with naturally sheltered coastal formations. In open seas where wave heights are relatively large, the semi-submersible type of structure is required, to minimise the effects of waves (Watanabe et al., 2004). It is common for the semi-submersible type to be modelled as a column supported structure consisting of a thin upper deck and a great number of buoyancy elements. In Japan, most VLFS research has focused on the pontoon type structure (Kashiwagi, 2000). Formulations for the pontoon type are closely related to ice plate formulations. For the pontoon type, the wavelengths are very small compared to the horizontal dimensions of the structure, hydroelastic responses are more important than the rigid-body motions due to the relatively small flexural rigidity of the structure, and they have a small draft (Kashiwagi, 2000). Consequently, much of the floating ice and VLFS modelling methods are similar e.g. Matched Eigenfunction Expansion Methods, Mesh Methods, and Green function Methods. Recently, VLFS research has focused on topics such as mooring systems, breakwaters, profiles of seabed and anti-motion devices.

In this thesis, we consider a VLFS which is constructed via connecting a series of plates, and solve using both the MEEM and GFM for various articulated edge conditions, including springed and hinged plates (Chapter 6).

3

Formulation and Preliminaries

3.1 Introduction

We begin this chapter by outlining the two-dimensional elastic plate problem. We then outline the familiar assumptions and boundary conditions. This is an important aspect of this research as it forms the basis of our solution. We conclude the chapter with the final non-dimensionalised equations.

3.2 The Problem

In this thesis, we consider the problem of small amplitude waves, incident on a set of floating elastic plates occupying the entire water surface. Open water surfaces are approximated by very thin plates. The submergence of the plates is considered negligible. The extension of the method to submerged plates may be possible by modifying the present formulation, but this remains a subject for future research. We assume the problem is invariant in one horizontal direction, although we allow the waves to be incident from an angle. The set of plates consists of two semi-infinite plates separated by a region consisting of a finite number of plates, each with unique properties. A schematic diagram of the problem is shown in Figure 3.1.

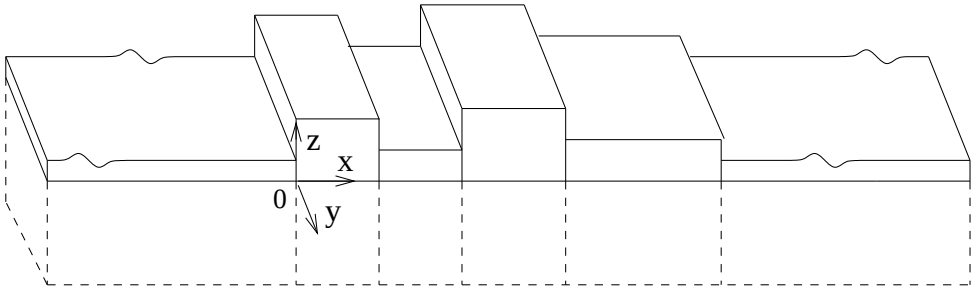

Figure 3.1: A schematic diagram of small amplitude waves incident on a set of floating plates occupying the entire water surface. x and y represent the horizontal co-ordinates and z represents the vertical co-ordinate.

3.3 Assumptions and Conditions

We assume that in the fluid region $-\infty < x, y < \infty$ and $-h < z \leq 0$, the flow is irrotational and inviscid, so that the fluid velocity can be written as the gradient of a velocity potential, Φ, which satisfies Laplace's equation in the fluid region, i.e.

$$\nabla^2 \Phi = 0, \qquad \text{for } -h < z \leq 0. \tag{3.1}$$

We consider only incident waves of a single frequency ω, and we assume that these waves also have a simple harmonic variation with respect to y. The velocity potential of the wave can therefore be expressed as

$$\Phi(x, y, z, t) = \Re\{\phi(x, z) e^{ik_y y} e^{-i\omega t}\} \tag{3.2}$$

(Stoker, 1957), where ϕ is the complex-valued potential, k_y is the wave number in the y direction, t is time and $\Re$ denotes the real part. The corresponding elevation of the plates is defined by $\Re\{\eta(x) e^{ik_y y} e^{-i\omega t}\}$.

3.3.1 The Seabed

We assume the seabed is impermeable, therefore the velocity component normal to the sea floor vanishes. Hence, the velocity potential at the sea floor satisfies

$$\frac{\partial \Phi}{\partial z} = 0, \qquad \text{at } z = -h. \tag{3.3}$$

3.3.2 The Free Surface

Open water, or the free surface, can also be solved explicitly by considering the following conditions, which are applied in Section 4.4.3. At the free surface, where the (moving) surface is always composed of fluid particles, the kinematic condition holds (Johnson, 1997) and is defined as

$$\frac{\partial \Phi}{\partial z} = \frac{\partial \eta}{\partial t} + \frac{\partial \Phi}{\partial x \partial y}\frac{\partial \eta}{\partial x \partial y}, \quad \text{at } z = 0. \tag{3.4}$$

We assume the amplitude at the free surface is small relative to the wavelength, and that the curvature is small. Hence, the non-linear term can be assumed negligible and the kinematic condition (3.4) becomes

$$\frac{\partial \eta}{\partial t} = \frac{\partial \Phi}{\partial z}, \quad \text{at } z = 0 \tag{3.5}$$

(Billingham and King, 2000). We eliminate time dependence using (3.2) to give

$$-i\omega\eta = \frac{\partial \phi}{\partial z}, \quad \text{at } z = 0. \tag{3.6}$$

As it is assumed the flow is irrotational, the dynamic condition given by Bournoulli's equation applies

$$\frac{\partial \Phi}{\partial t} + \frac{1}{2}\nabla\Phi \cdot \nabla\Phi + \frac{P}{\rho_w} + g\eta = 0 \tag{3.7}$$

(Stoker, 1957), where P is the pressure at the water surface, g is the gravitational constant and ρ_w is the water density.

It is usual to set the pressure at the free surface equal to the constant atmospheric pressure (Johnson, 1997). We also linearise at the surface and eliminate time dependence to give

$$-i\omega\phi + g\eta = 0, \quad \text{at } z = 0. \tag{3.8}$$

3.3.3 The Covered Surface

We assume the μ^{th} elastic plate has mass density ρ_μ and thickness τ_μ. The equation of motion for the plate is therefore given by the elastic plate equation

$$P = D_\mu \left(\frac{\partial^2}{\partial x^2} - k_y^2\right)^2 \eta - \omega^2 \rho_\mu \tau_\mu \eta, \quad \text{at } z = 0, \quad \text{for } l_\mu \leq x \leq r_\mu, \tag{3.9}$$

where P is the pressure at the surface, D_μ is the rigidity constant of the μth plate and is given by $D_\mu = Y\tau_\mu^3/(12\rho_\mu(1-\nu^2))$ where Y is the effective Young's modulus (GPa) and ν is Poisson's constant. l_μ and r_μ $(= l_{\mu+1})$ are the x co-ordinates of the left and right edge of the μth plate. The dynamic condition given by the linearised Bernoulli's equation for a covered surface applies

$$-i\omega\phi + \frac{P}{\rho_w} + g\eta = 0, \qquad \text{at } z = 0 \tag{3.10}$$

(Stoker, 1957), where P is the pressure at the water surface and ρ_w is the water density. Equating (3.9) and (3.10) gives

$$D_\mu \left(\frac{\partial^2}{\partial x^2} - k_y^2\right)^2 \eta - \omega^2\rho_\mu\tau_\mu\eta - i\omega\rho_w\phi + \rho_w g\eta = 0, \qquad \text{at } z = 0, \quad \text{for } l_\mu \le x \le r_\mu. \tag{3.11}$$

3.3.4 The Plate Edges

Additional constraints apply at the edges of the elastic plates. Plates with free edges have a zero bending moment and shearing forces at each edge. The derivation of the free edge boundary conditions are given in Fox and Squire (1994). The free edge boundary conditions can be expressed as

$$\left(\frac{\partial^3}{\partial x^3} - k_y^2(2-\nu)\frac{\partial}{\partial x}\right)\eta = 0, \qquad \text{at } z = 0, \quad \text{for } x = l_\mu, r_\mu, \tag{3.12}$$

$$\left(\frac{\partial^2}{\partial x^2} - k_y^2\nu\right)\eta = 0, \qquad \text{at } z = 0, \quad \text{for } x = l_\mu, r_\mu. \tag{3.13}$$

Alternative conditions considered in this thesis include: clamped, simply supported, sliding, springed and hinged. The clamped edge boundary conditions can be expressed as

$$\frac{\partial\eta}{\partial x} = 0, \qquad \text{at } z = 0, \quad \text{for } x = l_\mu, r_\mu, \tag{3.14}$$

$$\eta = 0, \qquad \text{at } z = 0, \quad \text{for } x = l_\mu, r_\mu. \tag{3.15}$$

The simply supported edge boundary conditions can be expressed as

$$\frac{\partial^2 \eta}{\partial x^2} = 0, \qquad \text{at } z = 0, \qquad \text{for } x = l_\mu, r_\mu, \tag{3.16}$$

$$\eta = 0, \qquad \text{at } z = 0, \qquad \text{for } x = l_\mu, r_\mu. \tag{3.17}$$

The sliding edge boundary conditions can be expressed as

$$\frac{\partial^3 \eta}{\partial x^3} = 0, \qquad \text{at } z = 0, \qquad \text{for } x = l_\mu, r_\mu, \tag{3.18}$$

$$\frac{\partial \eta}{\partial x} = 0, \qquad \text{at } z = 0, \qquad \text{for } x = l_\mu, r_\mu. \tag{3.19}$$

(Chung, 2002). The springed edge boundary conditions can be expressed as

$$\begin{aligned}
\left(\frac{\partial^3}{\partial x^3} - k_y^2(2-\nu)\frac{\partial}{\partial x}\right)\eta(l_{\mu+1}) &= -\frac{s_v}{\beta}\big(\eta(l_{\mu+1}) - \eta(r_\mu)\big), \\
\left(\frac{\partial^3}{\partial x^3} - k_y^2(2-\nu)\frac{\partial}{\partial x}\right)\eta(r_\mu) &= -\frac{s_v}{\beta}\big((\eta(l_{\mu+1}) - \eta(r_\mu)\big), \\
\left(\frac{\partial^2}{\partial x^2} - k_y^2\nu\right)\eta(l_{\mu+1}) &= \frac{s_r}{\beta}\left(\frac{\partial \eta(l_{\mu+1})}{\partial x} - \frac{\partial \eta(r_\mu)}{\partial x}\right), \\
\left(\frac{\partial^2}{\partial x^2} - k_y^2\nu\right)\eta(r_\mu) &= \frac{s_r}{\beta}\left(\frac{\partial \eta(l_{\mu+1})}{\partial x} - \frac{\partial \eta(r_\mu)}{\partial x}\right)
\end{aligned} \tag{3.20}$$

(Xia et al., 2000), where s_v is the vertical spring constant, s_r is the rotational spring constant and β is the stiffness constant. Lastly, the hinged edge boundary conditions can be expressed as

$$\begin{aligned}
\eta(r_\mu) - \eta(l_{\mu+1}) &= 0, \\
\frac{\partial^3 \eta(r_\mu)}{\partial x^3} - \frac{\partial^3 \eta(l_{\mu+1})}{\partial x^3} &= 0, \\
\frac{\partial^2 \eta(l_{\mu+1})}{\partial x^2} &= 0, \\
\frac{\partial^2 \eta(r_\mu)}{\partial x^2} &= 0.
\end{aligned} \tag{3.21}$$

3.4 Non-Dimensionalising the Variables

It is convenient to reduce the number of constants in the equations by non-dimensionalising. We non-dimensionalise by scaling the spatial variables by a length parameter $\mathcal{L}$ and the time variables by a time parameter $\sqrt{\mathcal{L}/g}$. The choice of length parameter, $\mathcal{L}$, we leave open. A typical value for $\mathcal{L}$ is the water depth, h. The non-dimensional variables, denoted by an overbar are

$$\bar{x} = \frac{x}{\mathcal{L}}, \bar{y} = \frac{y}{\mathcal{L}}, \bar{z} = \frac{z}{\mathcal{L}}, \bar{\eta} = \frac{\eta}{\mathcal{L}}, \bar{t} = \frac{t}{\sqrt{g/\mathcal{L}}}, \bar{\omega} = \frac{\omega}{\sqrt{g/\mathcal{L}}}, \text{ and } \bar{\phi} = \frac{\phi}{\mathcal{L}\sqrt{\mathcal{L}g}}.$$

The free surface boundary condition given by (3.8) can now be non-dimensionally expressed as

$$-i\bar{\omega}\bar{\phi} + \bar{\eta} = 0, \quad \text{for } z = 0. \tag{3.22}$$

Also, the boundary condition given by (3.11) can now be non-dimensionally expressed as

$$\beta_\mu \left(\frac{\partial^2}{\partial \bar{x}^2} - k_y^2 \right)^2 \bar{\eta} - \bar{\omega}^2 \gamma_\mu \bar{\eta} - i\bar{\omega}\bar{\phi} + \bar{\eta} = 0, \quad \text{at } z = 0, \quad \text{for } \bar{l}_\mu \leq \bar{x} \leq \bar{r}_\mu, \tag{3.23}$$

where $\beta_\mu = D_\mu/(\rho_\mu g \mathcal{L}^4)$ is the stiffness constant and $\gamma_\mu = \rho_\mu \tau_\mu/(\rho_w \mathcal{L})$ is the mass constant. From here on, all equations are expressed non-dimensionally, and for simplicity the overbar will be omitted from the dimensionless variables in what follows.

3.5 Final Equations

Eliminating η using (3.6), equations (3.1), (3.3), (3.22) and (3.23) become

$$\left(\frac{\partial^2}{\partial x^2} + \frac{\partial^2}{\partial z^2} - k_y^2 \right) \phi = 0, \quad \text{for } -h < z \leq 0, \tag{3.24}$$

$$\frac{\partial \phi}{\partial z} = 0, \quad \text{at } z = -h, \tag{3.25}$$

$$\frac{\partial \phi}{\partial z} = \alpha \phi, \quad \text{at } z = 0, \quad \text{for } l_\mu \leq x \leq r_\mu, \tag{3.26}$$

$$\left(\beta_\mu \left(\frac{\partial^2}{\partial x^2} - k_y^2\right)^2 - \gamma_\mu \alpha + 1\right) \frac{\partial \phi}{\partial z} - \alpha \phi = 0, \qquad \text{at } z = 0, \quad \text{for } l_\mu \leq x \leq r_\mu, \qquad (3.27)$$

where $\alpha = \omega^2$.

4

The Matched Eigenfunction Expansion Method

4.1 Introduction

Within this chapter, we explicitly go through the steps involved in solving the elastic plate problem using the Matched Eigenfunction Expansion Method (MEEM) (Linton and McIver, 2001). We begin the chapter with a general description of the problem and explain how it is solved. This is followed by solving explicitly for two plates, which leads to solving for a set of plates. To finalise, we also solve for the shallow water case and discuss an alternative solution method, which includes the free surface formulations.

4.2 Method of Solution

4.2.1 Eigenfunction Expansion

We will solve (3.24) to (3.27) using an eigenfunction expansion. This method has been applied in many situations for linear water wave problems, and the technique is described in Linton and McIver (2001). The method was developed by Fox and Squire (1994) for the case of the elastic plate boundary condition. We show here how this method can

be extended to the case of an arbitrary number of plates. This extension of the MEEM has been published in Kohout et al. (2007). One of the key features in the eigenfunction expansion method for elastic plates, is that extra modes are required in order to solve the higher order boundary conditions at the plate edges. The first and last plates are semi-infinite and the middle plates are finite. The velocity potential under the first plate can be expressed as the summation of an incident wave and of reflected waves, one of which is propagating but the rest of which are evanescent and decay as x tends to minus infinity. Similarly, the potential under the final plate can be expressed as a sum of transmitted waves, one of which is propagating and the rest of which are evanescent and decay towards positive infinity. The potential under the middle plates can be expressed as the sum of transmitted waves and reflected waves, each of which consists of a propagating wave and evanescent waves, which decay as x increases or decreases respectively (Figure 4.1). We could combine these waves in the formulation, but because of the exponential growth (or decay) in the x direction, in some cases the solution becomes numerically unstable if the transmission and reflection are not expanded at opposite ends of the plate.

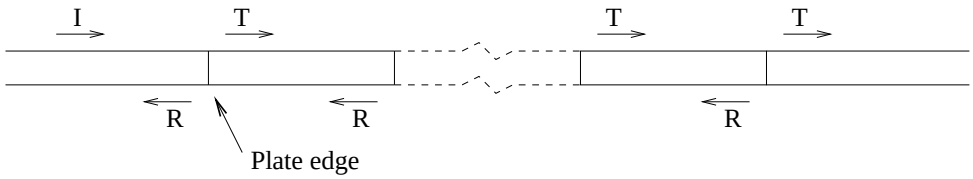

Figure 4.1: A schematic diagram of the incident (I), reflected (R) and transmitted (T) waves.

The velocity potential can be written in terms of an infinite series of separated eigenfunctions of the form

$$e^{\kappa(x)} \cos(k(z+h)) \tag{4.1}$$

(Ursell, 1947), where κ and k are the wave numbers in the x and z direction respectively.

The free surface

As discussed in Section 4.4.3, the free surface can be solved exactly. It is however possible to estimate the solution for the free surface, by solving for a surface covered by a very thin plate. To identify the eigenfunctions at the free surface, we apply the free surface boundary condition (3.26) to (4.1) and obtain

$$k_\mu^f \tan(k_\mu^f h) = \alpha. \tag{4.2}$$

Solving for k_μ^f, the free surface wave number of the μ^{th} plate in the z direction, the dispersion equation (4.2) gives a negative and positive pure imaginary root and an infinite number of real roots which approach $\pm m\pi/h$ as m approaches $\pm$ infinity (Linton and McIver, 2001). We denote the negative purely imaginary root by $k_\mu^f(0)$ and the positive real roots by $k_\mu^f(m)$ for m a positive integer. $k_\mu^f(0)$ corresponds to a reflected travelling mode propagating along the x axis and $k_\mu^f(m)$ correspond to the reflected evanescent modes. In a similar manner, the negative of these correspond to the transmitted travelling and evanescent modes respectively.

The covered surface

To identify the eigenfunctions of a covered surface, we apply the boundary conditions given by (3.25) and (3.27), and obtain

$$k_\mu \tan(k_\mu h) = -\frac{\alpha}{\beta_\mu k_\mu^4 + 1 - \alpha\gamma_\mu}. \tag{4.3}$$

Solving for k_μ, the covered surface wave number of the μ^{th} plate in the z direction, the dispersion equation (4.3) gives a negative and positive pure imaginary root, four complex roots (two complex conjugate paired roots with positive real part and two with negative real part in all physical situations), an infinite number of real roots which approach $\pm m\pi/h$ as m approaches $\pm$ infinity (Fox and Squire, 1994). We denote the two complex roots with positive real part by $k_\mu(-2)$ and $k_\mu(-1)$, the negative purely imaginary root by $k_\mu(0)$ and the positive real roots by $k_\mu(m)$ for m a positive integer. $k_\mu(-2)$ and $k_\mu(-1)$ correspond to damped reflected travelling modes, $k_\mu(0)$ corresponds to a reflected travelling mode propagating along the x axis, and $k_\mu(m)$ correspond to reflected evanescent modes. In a similar manner, the negative of these correspond to the transmitted travelling, damped and evanescent modes respectively. Note that $\beta = \gamma = 0$ recovers (4.2) with $-\alpha$.

The coefficient κ_μ is given by

$$\kappa_\mu(m) = \sqrt{k_\mu(m)^2 + k_y^2},$$

where $k_y = k_1(0)\sin(\theta)$, where θ is the incident wave angle with respect to the x-axis. Note that the solutions of the dispersion equation will differ per plate, and that the expansion is only valid under a single plate.

4.2.2 The Velocity Potential

The incident wave

The incident wave consists of one travelling mode from negative infinity. Its potential is defined by

$$\phi_I = Ie^{-\kappa_1(0)(x-r_1)}\cos\left(k_1(0)(z+h)\right),$$

where I is the non-dimensional incident wave amplitude in potential and r_1 is the right edge of the first plate.

The transmitted and reflected waves

We expand the potential under each plate (or the free surface) using the separation of variables solution. For the potential under each plate (or free surface), we include all of the roots of each dispersion equation (note, there are M+3 roots under each plate and M+1 roots under each free surface, where M is the number of evanescent roots of the dispersion equation). For the reflected waves, we require a solution of ϕ that remains finite as x approaches $-\infty$ and only consider the positive solutions of the dispersion equation (4.3). For the transmitted waves, we require a solution that remains finite as x approaches ∞ and consider the negative solutions of the dispersion equation. The potential, ϕ, under the μ^{th} plate can now be expressed as the eigenfunctions transmitted through the l_μ edge and propagating in the positive x direction, plus the eigenfunctions reflected from the r_μ edge and propagating in the negative x direction (Figure 4.1), i.e.

$$\begin{aligned}\phi_\mu \approx \sum_{m=n}^{M} & T_\mu(m)e^{-\kappa_\mu(m)(x-l_\mu)}\frac{\cos k_\mu(m)(z+h)}{\cos k_\mu(m)h} \\ & +R_\mu(m)e^{\kappa_\mu(m)(x-r_\mu)}\frac{\cos k_\mu(m)(z+h)}{\cos k_\mu(m)h}, \quad \text{for } l_\mu < x < r_\mu,\end{aligned} \tag{4.4}$$

where $n = 0$ for the free surfaces and $n = -2$ for the ice-covered surfaces, μ is the μ^{th} plate, Λ is the last plate, r_μ is the x-co-ordinate of the right edge of the μ^{th} plate, l_μ is the x-co-ordinate of the left edge of the μ^{th} plate, $R_\mu(m)$ is the reflected potential coefficient of the m^{th} mode under the μ^{th} plate, and $T_\mu(m)$ is the transmitted potential coefficient of the m^{th} mode under the μ^{th} plate. Note that 4.4 is a truncation, for $M = \infty$ the solution would be exact. Also, note that we divide by $\cos(kh)$. This is so the coefficients are normalised by the potential at the surface rather than at the seabed. This means that if the water is deep and the potential at the seabed is small, we avoid the problem of having very small numbers for the coefficients in the expansion.

4.2.3 The Displacement

Recall (3.6) which, assuming a small amplitude relative to wave length, implies

$$\eta_\mu = -\frac{1}{i\omega}\partial_z \phi_\mu \big|_{z=0}. \tag{4.5}$$

Using (4.4), (4.5) becomes

$$\begin{aligned} \eta_\mu \approx \; & -\frac{1}{i\omega}\sum_{m=n}^{M} -T_\mu(m)k_\mu(m)e^{-\kappa_\mu(m)(x-l_\mu)}\tan\left(k_\mu(m)h\right) \\ & -R_\mu(m)k_\mu(m)e^{\kappa_\mu(m)(x-r_\mu)}\tan\left(k_\mu(m)h\right), \text{ for } l_\mu < x < r_\mu. \end{aligned} \tag{4.6}$$

4.2.4 Eigenfunction Matching

To solve for the coefficients T_μ and R_μ, we require as many equations as we have unknowns. We derive the equations from the edge conditions, and from imposing conditions of continuity of the potential and its partial derivative with respect to x, at each plate boundary. We impose the latter condition by taking inner products with respect to the orthogonal functions $\cos\frac{n\pi}{h}(z+h)$ where n is a natural number. These functions are chosen for the following reasons. The vertical plate eigenfunctions, $\cos k_\mu(m)(z+h)$, are not orthogonal (they are not even a basis) and could therefore lead to an ill-conditioned system of equations. Furthermore, by choosing $\cos\frac{n\pi}{h}(z+h)$ we can use the same functions to take the inner products under every plate. Finally, and most importantly, the plate and free surface eigenfunctions approach $\cos(n\pi/h)(z+h)$ for large n, so that as we increase the number of modes, the matrices become almost diagonal, leading to a very well-conditioned system of equations.

4.3 Wave Propagation Through Two Semi-Infinite Elastic Plates

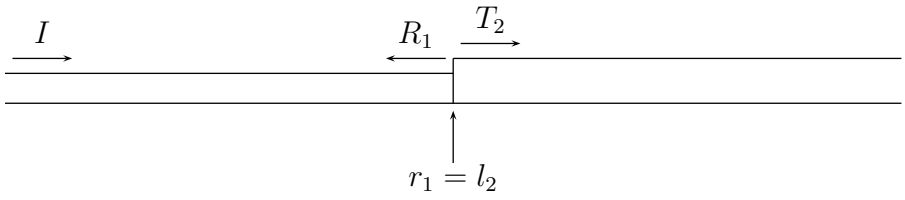

Figure 4.2: A schematic diagram of wave propagation through two semi-infinite plates with an incident wave (I) and reflected waves (R) under the left plate and transmitted waves under the right plate (T). r_1 is the right edge of the first plate and l_2 is the left edge of the second plate.

For simplicity, we first show the solution for wave propagation through two semi-infinite elastic plates with no edge restrictions. Each plate is homogeneous, but the plate properties per plate can vary (i.e. thickness). The wave can be incident from any angle. We have an incident wave and the reflected waves under the first plate. Under the second plate, we have the transmitted waves only (Figure 4.2). Note, the solution in this section is exactly the solution of Barrett and Squire (1996). This particular problem has also been solved by the Wiener–Hopf technique (Chung and Fox, 2002).

From Section 4.2, we can define the velocity potential of the region as

$$\phi \approx \begin{cases} Ie^{-\kappa_1(0)(x-r_1)}\dfrac{\cos(k_1(0)(z+h))}{\cos(k_1(0)h)} \\ \qquad + \displaystyle\sum_{m=-2}^{M} R_1(m)e^{\kappa_1(m)(x-r_1)}\dfrac{\cos(k_1(m)(z+h))}{\cos(k_1(m)h)}, & \text{for } x < r_1, \\ \displaystyle\sum_{m=-2}^{M} T_2(m)e^{-\kappa_2(m)(x-l_2)}\dfrac{\cos(k_2(m)(z+h))}{\cos(k_2(m)h)}, & \text{for } x > r_1, \end{cases} \tag{4.7}$$

and the displacement as

$$\eta(x) \approx -\frac{1}{i\omega}\begin{cases} -Ik_1(0)e^{-\kappa_1(0)(x-r_1)}\tan(k_1(0)h) \\ \qquad - \displaystyle\sum_{m=-2}^{M} R_1(m)k_1(m)e^{\kappa_1(m)(x-r_1)}\tan(k_1(m)h), & \text{for } x < r_1, \\ - \displaystyle\sum_{m=-2}^{M} T_2(m)k_2(m)e^{-\kappa_2(m)(x-l_2)}\tan(k_2(m)h), & \text{for } x > r_1. \end{cases} \tag{4.8}$$

As described in Section 4.2, we solve via eigenfunction matching between the plates

$$\begin{aligned}\int_{-h}^{0}\phi_1(r_1,z)\cos\frac{n\pi}{h}(z+h)\,dz &= \int_{-h}^{0}\phi_2(l_2,z)\cos\frac{n\pi}{h}(z+h)\,dz,\\ \int_{-h}^{0}\frac{\partial\phi_1(r_1,z)}{\partial x}\cos\frac{n\pi}{h}(z+h)\,dz &= \int_{-h}^{0}\frac{\partial\phi_2(l_2,z)}{\partial x}\cos\frac{n\pi}{h}(z+h)\,dz,\end{aligned} \tag{4.9}$$

where $n\in[0,M]$. Expanding the first matching in (4.9) gives

$$\begin{aligned}&\int_{-h}^{0}\sum_{m=-2}^{M} I\frac{\cos\left(k_1(0)(z+h)\right)}{\cos(k_1(0)h)}\cos\Big(\frac{n\pi}{h}(z+h)\Big)\,dz\\ &\quad+\int_{-h}^{0}\sum_{m=-2}^{M} R_1(m)\frac{\cos\left(k_1(m)(z+h)\right)}{\cos(k_1(m)h)}\cos\Big(\frac{n\pi}{h}(z+h)\Big)\,dz\\ &=\int_{-h}^{0}\sum_{m=-2}^{M} T_2(m)\frac{\cos\left(k_2(m)(z+h)\right)}{\cos(k_2(m)h)}\cos\Big(\frac{n\pi}{h}(z+h)\Big)\,dz,\end{aligned} \tag{4.10}$$

and expanding the second matching gives

$$\begin{aligned}&\int_{-h}^{0}\sum_{m=-2}^{M} -\kappa_1(0)I\frac{\cos\left(k_1(0)(z+h)\right)}{\cos(k_1(0)h)}\cos\Big(\frac{n\pi}{h}(z+h)\Big)\,dz\\ &\quad+\int_{-h}^{0}\sum_{m=-2}^{M} R_1(m)\frac{\cos\left(k_1(m)(z+h)\right)}{\cos(k_1(m)h)}\cos\Big(\frac{n\pi}{h}(z+h)\Big)\,dz\\ &=\int_{-h}^{0}\sum_{m=-2}^{M} T_2(m)\frac{\cos\left(k_2(m)(z+h)\right)}{\cos(k_2(m)h)}\cos\Big(\frac{n\pi}{h}(z+h)\Big)\,dz.\end{aligned} \tag{4.11}$$

The remaining equations to be solved are given by the two free edge conditions per edge

$$\begin{aligned}\left(\frac{\partial^3}{\partial x^3}-k_y^2(2-\nu)\frac{\partial}{\partial x}\right)\frac{\partial\phi}{\partial z} &= 0,\quad \text{at } z=0,\quad \text{for } x=r_1,l_2,\\ \left(\frac{\partial^2}{\partial x^2}-k_y^2\nu\right)\frac{\partial\phi}{\partial z} &= 0,\quad \text{at } z=0,\quad \text{for } x=r_1,l_2.\end{aligned} \tag{4.12}$$

Expanding the first edge condition under the first plate in (4.12) gives

$$0=\sum_{m=-2}^{M}\big(I-R_1\big)\big((\kappa_1(m)^3-\kappa_1(m)k_y^2(2-\nu)\big)\tan(k_1(m)h)\big), \tag{4.13}$$

and expanding the first edge condition under the second plate gives

$$0 = -\sum_{m=-2}^{M} T_2\big((\kappa_2(m)^3 - \kappa_2(m)k_y^2(2-\nu))\tan(k_2(m)h)\big). \tag{4.14}$$

Expanding the second edge condition under the first plate in (4.12) gives

$$0 = \sum_{m=-2}^{M} \big(-I - R_1\big)\big((\kappa_1(m)^2 - k_y^2\nu)\tan(k_1(m)h)\big), \tag{4.15}$$

and expanding the second edge condition under the second plate gives

$$0 = \sum_{m=-2}^{M} -T_2\big((\kappa_2(m)^2 - k_y^2\nu)\tan(k_2(m)h)\big). \tag{4.16}$$

We will show the explicit form of the linear system of equations which arise when we solve (4.9) and (4.12). Let $\mathbf{T}_2$ be the vector representing $[\mathbf{T}_2(-2), ..., \mathbf{T}_2(M)]$ and $\mathbf{R}_1$ be the vector representing $[\mathbf{R}_1(-2), ..., \mathbf{R}_1(M)]$.

The equations which arise from matching between the plates are

$$\begin{aligned} I\mathbf{C} + \mathbf{M}_R\mathbf{R}_1 &= \mathbf{M}_T\mathbf{T}_2, \\ -\kappa_1(0)I\mathbf{C} + \mathbf{N}_R\mathbf{R}_1 &= \mathbf{N}_T\mathbf{T}_2, \end{aligned} \tag{4.17}$$

where $\mathbf{M}_R$ and $\mathbf{M}_T$ represent matrices of size $(M+1)$ by $(M+3)$ such that

$$\begin{aligned} \mathbf{M}_R(n,m) &= \int_{-h}^{0} \frac{\cos k_1(m)(z+h)}{\cos k_1(m)h} \cos\frac{n\pi}{h}(z+h)\,dz, \\ \mathbf{M}_T(n,m) &= \int_{-h}^{0} \frac{\cos k_2(m)(z+h)}{\cos k_2(m)h} \cos\frac{n\pi}{h}(z+h)\,dz. \end{aligned} \tag{4.18}$$

$\mathbf{N}_R$ and $\mathbf{N}_T$ are $(M+1)$ by $(M+3)$ matrices such that

$$\begin{aligned} \mathbf{N}_R(n,m) &= \kappa_1(m)\mathbf{M}_R(n,m), \\ \mathbf{N}_T(n,m) &= -\kappa_2(m)\mathbf{M}_T(n,m). \end{aligned} \tag{4.19}$$

$\mathbf{C}$ is a $(M+1)$ by (1) matrix representing the incident wave and is given by

$$\mathbf{C}(n) = \int_{-h}^{0} \frac{\cos k_1(0)(z+h)}{\cos k_1(0)h} \cos\frac{n\pi}{h}(z+h)\,dz. \tag{4.20}$$

We can express the edge conditions (4.12), as

$$\begin{aligned} I\mathbf{E}^{+}_{T_1} + \mathbf{E}^{+}_{R_1}\mathbf{R}_1 &= 0, \\ \mathbf{E}^{-}_{T_2}\mathbf{T}_2 &= 0, \end{aligned} \tag{4.21}$$

where $\mathbf{E}^{+}_{R_1}$ and $\mathbf{E}^{-}_{T_2}$ are (2) by (M+3) matrices given by

$$\begin{aligned} \mathbf{E}^{+}_{R_1}(1,m) &= (\kappa_1(m)^2 - (2-\nu)k_y^2)(-k_1(m)\kappa_1(m)\tan(k_1(m)h)), \\ \mathbf{E}^{-}_{T_2}(1,m) &= (\kappa_2(m)^2 - (2-\nu)k_y^2)(k_2(m)\kappa_2(m)\tan(k_2(m)h)), \\ \mathbf{E}^{+}_{R_1}(2,m) &= (\kappa_1(m)^2 - \nu k_y^2)(-k_1(m)\tan(k_1(m)h)), \\ \mathbf{E}^{-}_{T_2}(2,m) &= (\kappa_2(m)^2 - \nu k_y^2)(-k_2(m)\tan(k_2(m)h)). \end{aligned} \tag{4.22}$$

$\mathbf{E}^{+}_{T_1}$ represents the incident wave and is a (2) by (1) matrix given by

$$\begin{aligned} \mathbf{E}^{+}_{T_1}(1,0) &= (\kappa_1(0)^3 - k_y^2\kappa_1(0)(2-\nu))(k_1(0)\tan(k_1(0)h)), \\ \mathbf{E}^{+}_{T_1}(2,0) &= -(\kappa_1(0)^2 - \nu k_y^2)(k_1(0)\tan(k_1(0)h)). \end{aligned} \tag{4.23}$$

Combining the set of coefficients, $\mathbf{R}$ and $\mathbf{T}$ can now be solved by

$$\begin{pmatrix} \mathbf{M}_R & -\mathbf{M}_T \\ \mathbf{N}_R & -\mathbf{N}_T \\ \mathbf{E}^{+}_{R_1} & 0 \\ 0 & \mathbf{E}^{-}_{T_2} \end{pmatrix} \times \begin{pmatrix} \mathbf{R}_1 \\ \vdots \\ \mathbf{T}_2 \end{pmatrix} = \begin{pmatrix} -I\mathbf{C} \\ I\kappa_1(0)\mathbf{C} \\ 0 \\ \vdots \\ -I\mathbf{E}^{+}_{T_1} \\ 0 \\ 0 \end{pmatrix}.$$

4.4 Wave Propagation Through a Set of Plates

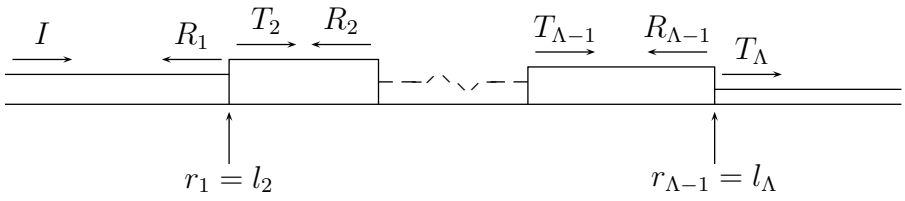

Figure 4.3: A schematic diagram of wave propagation through a set of plates with I representing the incident wave, R_μ representing the reflected waves under the μ^{th} plate and T_μ representing the transmitted waves under the μ^{th} plate. r_μ is the right edge of the μ^{th} plate and l_μ is the left edge of the μ^{th} plate.

4.4.1 Arbitrary Depth

Here we show how we can extend the eigenfunction expansion and matching technique to the case of a set of plates. We let the first and last plates be semi-infinite and the middle plates be finite. Each plate is homogeneous, but the plate properties can very per plate (i.e. thickness and length). The wave can be incident from any angle. The velocity potential of the first plate can be expressed as the summation of an incident wave and of reflected waves, one of which is propagating, the rest of which are evanescent and decay as x tends to minus infinity. Similarly the potential under the final plate can be expressed as a sum of transmitted waves, one of which is propagating and the rest of which are evanescent and decay towards plus infinity. The potential under the middle plates can be expressed as the sum of transmitted waves and reflected waves, each of which consists of a propagating wave plus evanescent waves which decay as x increases or decreases respectively (Figure 4.3).

We note that we can simulate open water by setting the plate thickness to be small or by introducing an additional formulation. For all solutions of the MEEM in this thesis, we simply set the plate thickness to be very thin to simulate open water. In Section 4.4.3, it is explained how to include the additional formulation to explicitly simulate open water.

We now expand the potential under each plate using the separation of variables solution. We always include the two complex and one imaginary root and truncate the expansion at M real roots to the dispersion equation. From Section 4.2, the potential ϕ can be

expressed as the following sum of eigenfunctions

$$\phi(x,z) \approx \begin{cases} Ie^{-\kappa_1(0)(x-r_1)}\dfrac{\cos(k_1(0)(z+h))}{\cos(k_1(0)h)} \\ \qquad + \displaystyle\sum_{m=-2}^{M} R_1(m)e^{\kappa_1(m)(x-r_1)}\frac{\cos(k_1(m)(z+h))}{\cos(k_1(m)h)}, & \text{for } x < r_1, \\ \displaystyle\sum_{m=-2}^{M} T_\mu(m)e^{-\kappa_\mu(m)(x-l_\mu)}\frac{\cos(k_\mu(m)(z+h))}{\cos(k_\mu(m)h)} \\ \qquad + \displaystyle\sum_{m=-2}^{M} R_\mu(m)e^{\kappa_\mu(m)(x-r_\mu)}\frac{\cos(k_\mu(m)(z+h))}{\cos(k_\mu(m)h)}, & \text{for } l_\mu < x < r_\mu, \\ \displaystyle\sum_{m=-2}^{M} T_\Lambda(m)e^{-\kappa_\Lambda(m)(x-l_\Lambda)}\frac{\cos(k_\Lambda(m)(z+h))}{\cos(k_\Lambda(m)h)}, & \text{for } l_\Lambda < x, \end{cases} \tag{4.24}$$

where I is the incident wave amplitude, μ is the μ^{th} plate, Λ is the last plate, r_μ is the x co-ordinate of the right edge of the μ^{th} plate, l_μ is the x co-ordinate of the left edge of the μ^{th} plate, $R_\mu(m)$ is the reflected potential coefficient of the m^{th} mode under the μ^{th} plate, and $T_\mu(m)$ is the transmitted potential coefficient of the m^{th} mode under the μ^{th} plate.

The displacement can be expressed as

$$\eta(x) \approx -\frac{1}{iw}\begin{cases} -Ik_1(0)e^{-\kappa_1(0)(x-r_1)}\tan(k_1(0)h) \\ \qquad - \displaystyle\sum_{m=-2}^{M} R_1(m)k_1(m)e^{\kappa_1(m)(x-r_1)}\tan(k_1(m)h), & \text{for } x < r_1, \\ - \displaystyle\sum_{m=-2}^{M} T_\mu(m)k_\mu(m)e^{-\kappa_\mu(m)(x-l_\mu)}\tan(k_\mu(m)h) \\ \qquad - \displaystyle\sum_{m=-2}^{M} R_\mu(m)k_\mu(m)e^{\kappa_\mu(m)(x-r_\mu)}\tan(k_\mu(m)h), & \text{for } l_\mu < x < r_\mu, \\ - \displaystyle\sum_{m=-2}^{M} T_\Lambda(m)k_\mu(m)e^{-\kappa_\mu(m)(x-l_\Lambda)}\tan(k_\mu(m)h), & \text{for } l_\Lambda < x. \end{cases} \tag{4.25}$$

To solve for the coefficients, we require as many equations as we have unknowns. As described in Section 4.2, we derive the equations from the free edge conditions and from imposing conditions of continuity of the potential and its derivative in the x-direction

at each plate boundary. We impose the latter condition by taking inner products with respect to the orthogonal functions $\cos\frac{n\pi}{h}(z+h)$ where n is a natural number. The matched eigenfunctions are given by

$$\begin{aligned}\int_{-h}^{0}\phi_\mu(r_\mu,z)\cos\left(\frac{n\pi}{h}(z+h)\right)\,dz\\ =\int_{-h}^{0}\phi_{\mu+1}(l_{\mu+1},z)\cos\left(\frac{n\pi}{h}(z+h)\right)\,dz\end{aligned}\tag{4.26}$$

and

$$\begin{aligned}\int_{-h}^{0}\frac{\partial\phi_\mu}{\partial x}(r_\mu,z)\cos\left(\frac{n\pi}{h}(z+h)\right)\,dz\\ =\int_{-h}^{0}\frac{\partial\phi_{\mu+1}}{\partial x}(l_{\mu+1},z)\cos\left(\frac{n\pi}{h}(z+h)\right)\,dz,\end{aligned}\tag{4.27}$$

where $n\in[0,M]$ and ϕ_μ is given by (4.24) and denotes the potential under the μ^{th} plate valid for $l_\mu<x<r_\mu$. Expanding (4.26) gives

$$\begin{aligned}&\int_{-h}^{0}\sum_{m=-2}^{M}T_\mu(m)e^{-\kappa_\mu(m)(r_\mu-l_\mu)}\frac{\cos\left(k_\mu(m)(z+h)\right)}{\cos(k_\mu(m)h)}\cos\left(\frac{n\pi}{h}(z+h)\right)dz\\ &\quad+\int_{-h}^{0}\sum_{m=-2}^{M}R_\mu(m)\frac{\cos\left(k_\mu(m)(z+h)\right)}{\cos(k_\mu(m)h)}\cos\left(\frac{n\pi}{h}(z+h)\right)dz\\ &=\int_{-h}^{0}\sum_{m=-2}^{M}T_{\mu+1}(m)\frac{\cos\left(k_{\mu+1}(m)(z+h)\right)}{\cos(k_{\mu+1}(m)h)}\cos\left(\frac{n\pi}{h}(z+h)\right)dz\\ &\quad+\int_{-h}^{0}\sum_{m=-2}^{M}R_{\mu+1}(m)e^{\kappa_{\mu+1}(m)(l_{\mu+1}-r_{\mu+1})}\frac{\cos\left(k_{\mu+1}(m)(z+h)\right)}{\cos(k_{\mu+1}(m)h)}\\ &\qquad\cos\left(\frac{n\pi}{h}(z+h)\right)dz,\end{aligned}\tag{4.28}$$

and expanding (4.27) gives

$$\begin{aligned}
&\int_{-h}^{0} \sum_{m=-2}^{M} -\kappa_\mu(m) T_\mu(m) e^{-\kappa_\mu(m)(r_\mu - l_\mu)} \frac{\cos\left(k_\mu(m)(z+h)\right)}{\cos(k_\mu(m)h)} \cos\left(\frac{n\pi}{h}(z+h)\right) dz \\
&\quad + \int_{-h}^{0} \sum_{m=-2}^{M} R_\mu(m) \frac{\cos\left(k_\mu(m)(z+h)\right)}{\cos(k_\mu(m)h)} \cos\left(\frac{n\pi}{h}(z+h)\right) dz \\
&= \int_{-h}^{0} \sum_{m=-2}^{M} T_{\mu+1}(m) \frac{\cos\left(k_{\mu+1}(m)(z+h)\right)}{\cos(k_{\mu+1}(m)h)} \cos\left(\frac{m\pi}{h}(z+h)\right) dz \\
&\quad + \int_{-h}^{0} \sum_{m=-2}^{M} -\kappa_{\mu+1}(m) R_{\mu+1}(m) e^{\kappa_{\mu+1}(m)(l_{\mu+1} - r_{\mu+1})} \frac{\cos\left(k_{\mu+1}(m)(z+h)\right)}{\cos(k_{\mu+1}(m)h)} \\
&\qquad\qquad \cos\left(\frac{n\pi}{h}(z+h)\right) dz.
\end{aligned} \tag{4.29}$$

The remaining equations to be solved are given by the two free edge conditions satisfied at both edges of each plate

$$\begin{aligned}
\left(\frac{\partial^3}{\partial x^3} - k_y^2(2-\nu)\frac{\partial}{\partial x}\right)\frac{\partial \phi_\mu}{\partial z} &= 0, \quad \text{at } z = 0, \text{ for } x = l_\mu, r_\mu, \\
\left(\frac{\partial^2}{\partial x^2} - k_y^2 \nu\right)\frac{\partial \phi_\mu}{\partial z} &= 0, \quad \text{at } z = 0, \text{ for } x = l_\mu, r_\mu.
\end{aligned} \tag{4.30}$$

We expand for the μ^{th} and $(\mu+1)^{th}$ plates for each edge condition in (4.30). The first edge condition at the left edge of the plate gives

$$\begin{aligned}
0 = \sum_{m=-2}^{M} &\left(T_\mu - R_\mu e^{\kappa_\mu(m)(l_\mu - r_\mu)}\right) \\
&\left((\kappa_\mu(m)^3 - \kappa_\mu(m) k_y^2(2-\nu))\tan(k_\mu(m)h)\right),
\end{aligned} \tag{4.31}$$

and the first edge condition at the right edge of the plate gives

$$\begin{aligned}
0 = \sum_{m=-2}^{M} &\left(T_\mu e^{-\kappa_\mu(m)(r_\mu - l_\mu)} - R_\mu\right) \\
&\left((\kappa_\mu(m)^3 - \kappa_\mu(m) k_y^2(2-\nu))\tan(k_\mu(m)h)\right).
\end{aligned} \tag{4.32}$$

The second edge condition at the left edge of the plate gives

$$0 = \sum_{m=-2}^{M} \left(-T_\mu - R_\mu e^{\kappa_\mu(m)(l_\mu - r_\mu)}\right) \left((\kappa_\mu(m)^2 - k_y^2\nu)\tan(k_\mu(m)h)\right), \tag{4.33}$$

and the second edge condition at the right edge of the plate gives

$$0 = \sum_{m=-2}^{M} \left(-T_\mu e^{-\kappa_\mu(m)(r_\mu - l_\mu)} - R_\mu\right) \left((\kappa_\mu(m)^2 - k_y^2\nu)\tan(k_\mu(m)h)\right). \tag{4.34}$$

We will show the explicit form of the linear system of equations which arise when we solve (4.28), (4.29) and (4.31) to (4.34).

Let $\mathbf{T}_\mu$ be a column vector given by $[T_\mu(-2), ..., T_\mu(M)]^{\mathbf{T}}$ and $\mathbf{R}_\mu$ be a column vector given by $[R_\mu(-2)...R_\mu(M)]^{\mathbf{T}}$. The equations which arise from matching at the boundary between the first and second plates are

$$\begin{aligned} &I\mathbf{C} + \mathbf{M}^+_{R_1}\mathbf{R}_1 = \mathbf{M}^-_{T_2}\mathbf{T}_2 + \mathbf{M}^-_{R_2}\mathbf{R}_2, \\ &-\kappa_1(0)I\mathbf{C} + \mathbf{N}^+_{\mathbf{R_1}}\mathbf{R_1} = \mathbf{N}^-_{\mathbf{T_2}}\mathbf{T_2} + \mathbf{N}^-_{\mathbf{R_2}}\mathbf{R_2}. \end{aligned} \tag{4.35}$$

The equations which arise from matching at the boundary between the μ^{th} and $(\mu+1)^{th}$ plates ($\mu > 1$) are

$$\begin{aligned} &\mathbf{M}^+_{T_\mu}\mathbf{T}_\mu + \mathbf{M}^+_{R_\mu}\mathbf{R}_\mu = \mathbf{M}^-_{T_{\mu+1}}\mathbf{T}_{\mu+1} + \mathbf{M}^-_{R_{\mu+1}}\mathbf{R}_{\mu+1}, \\ &\mathbf{N}^+_{T_\mu}\mathbf{T}_\mu + \mathbf{N}^+_{R_\mu}\mathbf{R}_\mu = \mathbf{N}^-_{T_{\mu+1}}\mathbf{T}_{\mu+1} + \mathbf{N}^-_{R_{\mu+1}}\mathbf{R}_{\mu+1}. \end{aligned} \tag{4.36}$$

The equations which arise from matching at the $\Lambda^{th} - 1$ and Λ^{th} boundary are

$$\begin{aligned} &\mathbf{M}^+_{T_{\Lambda-1}}\mathbf{T}_{\Lambda-1} + \mathbf{M}^+_{R_{\Lambda-1}}\mathbf{R}_{\Lambda-1} = \mathbf{M}^-_{T_\Lambda}\mathbf{T}_\Lambda, \\ &\mathbf{N}^+_{T_{\Lambda-1}}\mathbf{T}_{\Lambda-1} + \mathbf{N}^+_{R_{\Lambda-1}}\mathbf{R}_{\Lambda-1} = \mathbf{N}^-_{T_\Lambda}\mathbf{T}_\Lambda, \end{aligned} \tag{4.37}$$

where $\mathbf{M}^+_{T_\mu}$ and $\mathbf{M}^+_{R_\mu}$ are $(M+1)$ by $(M+3)$ matrices given by

$$\begin{aligned} \mathbf{M}^+_{T_\mu}(n,m) &= \int_{-h}^{0} e^{-\kappa_\mu(m)(r_\mu - l_\mu)} \frac{\cos\left(k_\mu(m)(z+h)\right)}{\cos\left(k_\mu(m)h\right)} \cos\left(\frac{n\pi}{h}(z+h)\right)\, dz, \\ \mathbf{M}^+_{R_\mu}(n,m) &= \int_{-h}^{0} \frac{\cos\left(k_\mu(m)(z+h)\right)}{\cos\left(k_\mu(m)h\right)} \cos\left(\frac{n\pi}{h}(z+h)\right)\, dz, \end{aligned} \tag{4.38}$$

and

$$\begin{aligned}\mathbf{M}^{-}_{T_\mu}(n,m) &= \mathbf{M}^{+}_{R_\mu}(n,m),\\ \mathbf{M}^{-}_{R_\mu}(n,m) &= \mathbf{M}^{+}_{T_\mu}(n,m).\end{aligned} \tag{4.39}$$

$\mathbf{N}^{+}_{T_\mu}$, $\mathbf{N}^{+}_{R_\mu}$, $\mathbf{N}^{-}_{T_\mu}$, and $\mathbf{N}^{-}_{R_\mu}$ are given by

$$\begin{aligned}\mathbf{N}^{\pm}_{T_\mu}(n,m) &= -\kappa_\mu(m)\mathbf{M}^{\pm}_{T_\mu}(n,m),\\ \mathbf{N}^{\pm}_{R_\mu}(n,m) &= \kappa_\mu(m)\mathbf{M}^{\pm}_{R_\mu}(n,m).\end{aligned} \tag{4.40}$$

$\mathbf{C}$ is a $(M+1)$ vector which is given by

$$\mathbf{C}(n) = \int_{-h}^{0} \frac{\cos(k_1(0)(z+h))}{\cos(k_1(0)h)} \cos\left(\frac{n\pi}{h}(z+h)\right)\, dz. \tag{4.41}$$

Now, for all but the first and Λ^{th} plate, (4.30) becomes

$$\begin{aligned}\mathbf{E}^{+}_{T_\mu}\mathbf{T}_\mu + \mathbf{E}^{+}_{R_\mu}\mathbf{R}_\mu &= 0,\\ \mathbf{E}^{-}_{T_\mu}\mathbf{T}_\mu + \mathbf{E}^{-}_{R_\mu}\mathbf{R}_\mu &= 0.\end{aligned} \tag{4.42}$$

The first and last plates only require two equations because there is only one plate edge. The equation for the first plate must be modified to include the effect of the incident wave. This gives

$$I\begin{pmatrix}\mathbf{E}^{+}_{T_1}(1,0)\\ \mathbf{E}^{+}_{T_1}(2,0)\end{pmatrix} + \mathbf{E}^{+}_{R_1}\mathbf{R}_1 = 0, \tag{4.43}$$

and for the Λ^{th} plate we have no reflection so

$$\mathbf{E}^{-}_{T_\Lambda}\mathbf{T}_\Lambda = 0 \tag{4.44}$$

$\mathbf{E}^{+}_{T_\mu}$, $\mathbf{E}^{+}_{R_\mu}$, $\mathbf{E}^{-}_{T_\mu}$ and $\mathbf{E}^{-}_{R_\mu}$ are (2) by (M+3) matrices given by

$$\begin{aligned}
\mathbf{E}^{-}(1,m)_{T_\mu} &= (\kappa_\mu(m)^2 - (2-\nu)k_y^2)(k_\mu(m)\kappa_\mu(m)\tan(k_\mu(m)h)),\\
\mathbf{E}^{+}(1,m)_{T_\mu} &= (\kappa_\mu(m)^2 - (2-\nu)k_y^2)(k_\mu(m)\kappa_\mu(m)e^{-\kappa_\mu(m)(r_\mu-l_\mu)}\tan(k_\mu(m)h)),\\
\mathbf{E}^{-}(1,m)_{R_\mu} &= (\kappa_\mu(m)^2 - (2-\nu)k_y^2)(-k_\mu(m)\kappa_\mu(m)e^{\kappa_\mu(m)(l_\mu-r_\mu)}\tan(k_\mu(m)h)),\\
\mathbf{E}^{+}(1,m)_{R_\mu} &= (\kappa_\mu(m)^2 - (2-\nu)k_y^2)(-k_\mu(m)\kappa_\mu(m)\tan(k_\mu(m)h)),\\
\mathbf{E}^{-}(2,m)_{T_\mu} &= (\kappa_\mu(m)^2 - \nu k_y^2)(-k_\mu(m)\tan(k_\mu(m)h)),\\
\mathbf{E}^{+}(2,m)_{T_\mu} &= (\kappa_\mu(m)^2 - \nu k_y^2)(-k_\mu(m)e^{-\kappa_\mu(m)(r_\mu-l_\mu)}\tan(k_\mu(m)h)),\\
\mathbf{E}^{-}(2,m)_{R_\mu} &= (\kappa_\mu(m)^2 - \nu k_y^2)(-k_\mu(m)e^{\kappa_\mu(m)(l_\mu-r_\mu)}\tan(k_\mu(m)h)),\\
\mathbf{E}^{+}(2,m)_{R_\mu} &= (\kappa_\mu(m)^2 - \nu k_y^2)(-k_\mu(m)\tan(k_\mu(m)h)).
\end{aligned} \tag{4.45}$$

Now, the matching matrix is a $(2M+6)\times(\Lambda-1)$ by $(2M+1)\times(\Lambda-1)$ matrix given by

$$\mathbf{M}=\begin{pmatrix}
\mathbf{M}^+_{R_1} & -\mathbf{M}^-_{T_2} & -\mathbf{M}^-_{R_2} & 0 & 0 & & 0 & 0 & 0\\
\mathbf{N}^+_{R_1} & -\mathbf{N}^-_{T_2} & -\mathbf{N}^-_{R_2} & 0 & 0 & & 0 & 0 & 0\\
0 & \mathbf{M}^+_{T_2} & \mathbf{M}^+_{R_2} & -\mathbf{M}^-_{T_3} & -\mathbf{M}^-_{R_3} & \dots & 0 & 0 & 0\\
0 & \mathbf{N}^+_{T_2} & \mathbf{N}^+_{R_2} & -\mathbf{N}^-_{T_3} & -\mathbf{N}^-_{R_3} & & 0 & 0 & 0\\
 & & \vdots & & & \ddots & & & \\
0 & 0 & 0 & 0 & 0 & & \mathbf{M}^+_{T_{\Lambda-1}} & \mathbf{M}^+_{R_{\Lambda-1}} & -\mathbf{M}^-_{T_\Lambda}\\
0 & 0 & 0 & 0 & 0 & & \mathbf{N}^+_{T_{\Lambda-1}} & \mathbf{N}^+_{R_{\Lambda-1}} & -\mathbf{N}^-_{T_\Lambda}
\end{pmatrix}, \tag{4.46}$$

the edge matrix is a $(2M+6)\times(\Lambda-1)$ by $4(\Lambda-1)$ matrix given by

$$\mathbf{E}=\begin{pmatrix}
\mathbf{E}^+_{R_1} & 0 & 0 & 0 & 0 & & 0 & 0 & 0\\
0 & \mathbf{E}^+_{T_2} & \mathbf{E}^+_{R_2} & 0 & 0 & & 0 & 0 & 0\\
0 & \mathbf{E}^-_{T_2} & \mathbf{E}^-_{R_2} & 0 & 0 & & 0 & 0 & 0\\
0 & 0 & 0 & \mathbf{E}^+_{T_3} & \mathbf{E}^+_{R_3} & \dots & 0 & 0 & 0\\
0 & 0 & 0 & \mathbf{E}^-_{T_3} & \mathbf{E}^-_{R_3} & & 0 & 0 & 0\\
 & & \vdots & & & \ddots & & & \\
0 & 0 & 0 & 0 & 0 & & \mathbf{E}^+_{T_{\Lambda-1}} & \mathbf{E}^+_{R_{\Lambda-1}} & 0\\
0 & 0 & 0 & 0 & 0 & & \mathbf{E}^-_{T_{\Lambda-1}} & \mathbf{E}^-_{R_{\Lambda-1}} & 0\\
0 & 0 & 0 & 0 & 0 & & 0 & 0 & \mathbf{E}^-_{T_\Lambda}
\end{pmatrix}, \tag{4.47}$$

and finally, the complete system to be solved is given by

$$\begin{pmatrix}\mathbf{M}\\ \mathbf{E}\end{pmatrix}\times\begin{pmatrix}
\mathbf{R}_1\\ \mathbf{T}_2\\ \mathbf{R}_2\\ \mathbf{T}_3\\ \mathbf{R}_3\\ \vdots\\ \mathbf{T}_{\Lambda-1}\\ \mathbf{R}_{\Lambda-1}\\ \mathbf{T}_\Lambda
\end{pmatrix}=\begin{pmatrix}
-I\mathbf{C}\\ \kappa_1(0)I\mathbf{C}\\ 0\\ \vdots\\ -I\mathbf{E}^+_{T_\mu}(1,0)\\ -I\mathbf{E}^+_{T_\mu}(2,0)\\ 0\\ \vdots
\end{pmatrix}. \tag{4.48}$$

The final system of equations has size $(2M+6)\times(\Lambda-1)$ by $(2M+6)\times(\Lambda-1)$. The method of solution we have derived is relatively simple and leads to large systems of equations when we simulate multiple plates. Our aim is to produce code which is simple to develop and which we have a strong degree of confidence is numerically accurate and error free. We do not want to make any kind of wide-spacing approximations since real

ice fields always have some small floes which we want to be able to account for. We have used our method to solve for up to a hundred plates in simulations of wave propagation in the Marginal Ice Zone.

The system of equations has a large number of zero entries, due to the fact that each plate couples only with its nearest neighbour. It seems likely that a more sophisticated method of solution could be developed, which exploits this structure. We have been unable to find such a method due to the difficulty of including the free edge conditions.

4.4.2 Shallow Water

Consider the special case of a wave in shallow water propagating obliquely through a set of ice plates. Recall the dispersion equation (4.3). For small h, $\tan(kh) \approx kh$ and the dispersion equation becomes

$$\beta_\mu k_\mu^6 + (1 - \alpha\gamma_\mu)k_\mu^2 - \frac{\alpha}{h} = 0. \tag{4.49}$$

Solving for k_μ gives two purely imaginary travelling modes and four complex damped travelling modes, i.e. there no longer exists an infinite number of real modes. Three modes for each of the reflected and transmitted potentials remain. The shallow water potential, ϕ^s, can now be expressed as

$$\phi^s = \begin{cases} Ie^{-\kappa_1(0)(x-r_1)}\dfrac{\cos(k_1(0)(z+h))}{\cos(k_1(0)h)} \\ \qquad + \displaystyle\sum_{m=-2}^{0} R_1(m)e^{\kappa_1(m)(x-r_1)}\frac{\cos(k_1(m)(z+h))}{\cos(k_1(m)h)}, & \text{for } x < r_1, \\ \displaystyle\sum_{m=-2}^{0} T_\mu(m)e^{-\kappa_\mu(m)(x-l_\mu)}\frac{\cos(k_\mu(m)(z+h)}{\cos(k_\mu(m)h)} \\ \qquad + R_\mu(m)e^{\kappa_\mu(m)(x-r_\mu)}\dfrac{\cos(k_\mu(m)(z+h))}{\cos(k_\mu(m)h)}, & \text{for } l_\mu < x < r_\mu, \\ \displaystyle\sum_{m=-2}^{0} T_\Lambda(m)e^{-\kappa_\mu(m)(x-l_\Lambda)}\frac{\cos(k_\mu(m)(z+h)}{\cos(k_\mu(m)h)}, & \text{for } l_\Lambda < x, \end{cases} \tag{4.50}$$

where μ stands for the μ^{th} plate and Λ is the last plate.

For the shallow water displacement, η^s, $\tan(kh) \approx kh$ implies

$$\eta^s = -\frac{i}{\omega}\begin{cases} Ik_1(0)^2 h e^{-\kappa_1(0)(x-r_1)} \\ \quad -\sum_{m=-2}^{0} R_1(m)k_1(m)^2 h e^{\kappa_1(m)(x-r_1)}, & \text{for } x < r_1, \\ -\sum_{m=-2}^{0} T_\mu(m)k_\mu(m)^2 h e^{-\kappa_\mu(m)(x-l_\mu)} \\ \quad -R_\mu(m)k_\mu(m)^2 h e^{\kappa_\mu(m)(x-r_\mu)}, & \text{for } l_\mu < x < r_\mu, \\ \eta_\Lambda = -\sum_{m=1}^{M+3} T_\Lambda(m)k_\Lambda(m)^2 e^{-\kappa_\Lambda(m)(x-l_\Lambda)}, & \text{for } l_\Lambda < x. \end{cases} \tag{4.51}$$

We again solve for the coefficients by matching the potential and its derivative at each plate boundary, but in this case do not need to generate extra equations as the evanescent modes are non-existent. We simply state that at each plate boundary at $z = 0$,

$$\begin{aligned} \phi_\mu &= \phi_{\mu+1}, \\ \frac{\partial \phi_\mu}{\partial x} &= \frac{\partial \phi_{\mu+1}}{\partial x}. \end{aligned} \tag{4.52}$$

The edge conditions remain the same as in (4.30). We show the explicit form of the linear system of equations which arise when solving for shallow water and again let $\mathbf{T}_\mu$ be a column vector given by $[T_\mu(-2), ..., T_\mu(M)]^{\mathbf{T}}$ and $\mathbf{R}_\mu$ be a column vector given by $[R_\mu(-2)...R_\mu(M)]^{\mathbf{T}}$. The equations which arise from matching at the boundary between the first and second plate are

$$\begin{aligned} I + \mathbf{M}^+_{R_1}\mathbf{R}_1 &= \mathbf{M}^-_{T_2}\mathbf{T}_2 + \mathbf{M}^-_{R_2}\mathbf{R}_2, \\ -\kappa_1(0)I + \mathbf{N}^+_{R_1}\mathbf{R}_1 &= \mathbf{N}^-_{T_2}\mathbf{T}_2 + \mathbf{N}^-_{R_2}\mathbf{R}_2. \end{aligned} \tag{4.53}$$

The equations which arise from matching at the boundary between the μ^{th} and $(\mu+1)^{th}$ plate are

$$\begin{aligned} \mathbf{M}^+_{T_\mu}\mathbf{T}_\mu + \mathbf{M}^+_{R_\mu}\mathbf{R}_\mu &= \mathbf{M}^-_{T_{\mu+1}}\mathbf{T}_{\mu+1} + \mathbf{M}^-_{R_{\mu+1}}\mathbf{R}_{\mu+1}, \\ \mathbf{N}^+_{T_\mu}\mathbf{T}_\mu + \mathbf{N}^+_{R_\mu}\mathbf{R}_\mu &= \mathbf{N}^-_{T_{\mu+1}}\mathbf{T}_{\mu+1} + \mathbf{N}^-_{R_{\mu+1}}\mathbf{R}_{\mu+1}. \end{aligned} \tag{4.54}$$

The equations which arise from matching at the $\Lambda^{th} - 1$ and Λ^{th} boundary are

$$\begin{aligned} \mathbf{M}^+_{T_{\Lambda-1}}\mathbf{T}_{\Lambda-1} + \mathbf{M}^+_{R_{\Lambda-1}}\mathbf{R}_{\Lambda-1} &= \mathbf{M}^-_{T_\Lambda}\mathbf{T}_\Lambda, \\ \mathbf{N}^+_{T_{\Lambda-1}}\mathbf{T}_{\Lambda-1} + \mathbf{N}^+_{R_{\Lambda-1}}\mathbf{R}_{\Lambda-1} &= \mathbf{N}^-_{T_\Lambda}\mathbf{T}_\Lambda, \end{aligned} \tag{4.55}$$

where for this case, $\mathbf{M}^+_{T_\mu}$, $\mathbf{M}^+_{R_\mu}$, $\mathbf{M}^-_{T_\mu}$, and $\mathbf{M}^-_{R_\mu}$are $(M+1)$ by $(M+3)$ matrices given by

$$\begin{aligned}
\mathbf{M}^+_{T_\mu}(n,m) &= e^{-\kappa_\mu(m)(r_\mu - l_\mu)}, \\
\mathbf{M}^+_{R_\mu}(n,m) &= 1, \\
\mathbf{M}^-_{T_\mu}(n,m) &= 1, \\
\mathbf{M}^-_{R_\mu}(n,m) &= e^{\kappa_\mu(m)(l_\mu - r_\mu)}.
\end{aligned} \tag{4.56}$$

$\mathbf{N}^+_{T_\mu}$, $\mathbf{N}^+_{R_\mu}$, $\mathbf{N}^-_{T_\mu}$, and $\mathbf{N}^-_{R_\mu}$ are given by

$$\begin{aligned}
\mathbf{N}^\pm(n,m)_{T_\mu} &= -\kappa_\mu(m)\mathbf{M}^\pm_{T_\mu}(n,m), \\
\mathbf{N}^\pm(n,m)_{R_\mu} &= \kappa_\mu(m)\mathbf{M}^\pm_{R_\mu}(n,m).
\end{aligned} \tag{4.57}$$

For all but the first and Λth plate, (4.30) can be expressed as

$$\begin{aligned}
\mathbf{E}^+_{T_\mu}\mathbf{T}_\mu + \mathbf{E}^+_{R_\mu}\mathbf{R}_\mu = 0, \\
\mathbf{E}^-_{T_\mu}\mathbf{T}_\mu + \mathbf{E}^-_{R_\mu}\mathbf{R}_\mu = 0.
\end{aligned} \tag{4.58}$$

For the first plate, we obtain

$$I\begin{pmatrix} \mathbf{E}^+_{T_1}(1,0) \\ \mathbf{E}^+_{T_1}(2,0) \end{pmatrix} + \mathbf{E}^+_{R_1}\mathbf{R}_1 = 0, \tag{4.59}$$

and, for the Λ^{th} plate,

$$\mathbf{E}^-_{T_\Lambda}\mathbf{T}_\Lambda = 0. \tag{4.60}$$

$\mathbf{E}^+_{T_\mu}$, $\mathbf{E}^+_{R_\mu}$, $\mathbf{E}^-_{T_\mu}$ and $\mathbf{E}^-_{R_\mu}$ are 2 by M+3 matrices given by

$$\begin{aligned}
\mathbf{E}^-(1,m)_{T_\mu} &= (\kappa_\mu(m)^2 - (2-\nu)k_y^2)(k_\mu^2(m)\kappa_\mu(m)), \\
\mathbf{E}^+(1,m)_{T_\mu} &= (\kappa_\mu(m)^2 - (2-\nu)k_y^2)(k_\mu^2(m)\kappa_\mu(m)e^{-\kappa_\mu(m)(r_\mu - l_\mu)}), \\
\mathbf{E}^-(1,m)_{R_\mu} &= (\kappa_\mu(m)^2 - (2-\nu)k_y^2)(-k_\mu^2(m)\kappa_\mu(m)e^{\kappa_\mu(m)(l_\mu - r_\mu)}), \\
\mathbf{E}^+(1,m)_{R_\mu} &= (\kappa_\mu(m)^2 - (2-\nu)k_y^2)(-k_\mu^2(m)\kappa_\mu(m)), \\
\mathbf{E}^-(2,m)_{T_\mu} &= (\kappa_\mu(m)^2 - \nu k_y^2)(-k_\mu^2(m)), \\
\mathbf{E}^+(2,m)_{T_\mu} &= (\kappa_\mu(m)^2 - \nu k_y^2)(-k_\mu^2(m)e^{-\kappa_\mu(m)(r_\mu - l_\mu)}), \\
\mathbf{E}^-(2,m)_{R_\mu} &= (\kappa_\mu(m)^2 - \nu k_y^2)(-k_\mu^2(m)e^{\kappa_\mu(m)(l_\mu - r_\mu)}), \\
\mathbf{E}^+(2,m)_{R_\mu} &= (\kappa_\mu(m)^2 - \nu k_y^2)(-k_\mu^2(m)).
\end{aligned} \tag{4.61}$$

We again express the large matching matrix as

$$\mathbf{M} = \begin{pmatrix} \mathbf{M}^+_{R_1} & -\mathbf{M}^-_{T_2} & -\mathbf{M}^-_{R_2} & 0 & 0 & & 0 & 0 & 0 \\ \mathbf{N}^+_{R_1} & -\mathbf{N}^-_{T_2} & -\mathbf{N}^-_{R_2} & 0 & 0 & & 0 & 0 & 0 \\ 0 & \mathbf{M}^+_{T_2} & \mathbf{M}^+_{R_2} & -\mathbf{M}^-_{T_3} & -\mathbf{M}^-_{R_3} & \dots & 0 & 0 & 0 \\ 0 & \mathbf{N}^+_{T_2} & \mathbf{N}^+_{R_2} & -\mathbf{N}^-_{T_3} & -\mathbf{N}^-_{R_3} & & 0 & 0 & 0 \\ & & \vdots & & & \ddots & & & \\ 0 & 0 & 0 & 0 & 0 & & \mathbf{M}^+_{T_{\Lambda-1}} & \mathbf{M}^+_{R_{\Lambda-1}} & -\mathbf{M}^-_{T_\Lambda} \\ 0 & 0 & 0 & 0 & 0 & & \mathbf{N}^+_{T_{\Lambda-1}} & \mathbf{N}^+_{R_{\Lambda-1}} & -\mathbf{N}^-_{T_\Lambda} \end{pmatrix}, \tag{4.62}$$

and the edge matrix as

$$\mathbf{E} = \begin{pmatrix} \mathbf{E}^+_{R_1} & 0 & 0 & 0 & 0 & & 0 & 0 & 0 \\ 0 & \mathbf{E}^+_{T_2} & \mathbf{E}^+_{R_2} & 0 & 0 & & 0 & 0 & 0 \\ 0 & \mathbf{E}^-_{T_2} & \mathbf{E}^-_{R_2} & 0 & 0 & & 0 & 0 & 0 \\ 0 & 0 & 0 & \mathbf{E}^+_{T_3} & \mathbf{E}^+_{R_3} & \dots & 0 & 0 & 0 \\ 0 & 0 & 0 & \mathbf{E}^-_{T_3} & \mathbf{E}^-_{R_3} & & 0 & 0 & 0 \\ & & \vdots & & & \ddots & & & \\ 0 & 0 & 0 & 0 & 0 & & \mathbf{E}^+_{T_{\Lambda-1}} & \mathbf{E}^+_{R_{\Lambda-1}} & 0 \\ 0 & 0 & 0 & 0 & 0 & & \mathbf{E}^-_{T_{\Lambda-1}} & \mathbf{E}^-_{R_{\Lambda-1}} & 0 \\ 0 & 0 & 0 & 0 & 0 & & 0 & 0 & \mathbf{E}^-_{T_\Lambda} \end{pmatrix}, \tag{4.63}$$

so that the complete system to be solved is given by

$$\begin{pmatrix} \mathbf{M} \\ \mathbf{E} \end{pmatrix} \times \begin{pmatrix} \mathbf{R}_1 \\ \mathbf{T}_2 \\ \mathbf{R}_2 \\ \mathbf{T}_3 \\ \mathbf{R}_3 \\ \vdots \\ \mathbf{T}_{\Lambda-1} \\ \mathbf{R}_{\Lambda-1} \\ \mathbf{T}_\Lambda \end{pmatrix} = \begin{pmatrix} -I \\ \kappa_1(0)I \\ 0 \\ \vdots \\ -IE^+_{T_1}(1,0) \\ -IE^+_{T_1}(1,0) \\ 0 \\ \vdots \end{pmatrix}. \tag{4.64}$$

4.4.3 The Free Surface Formulation

Throughout this thesis, open water is simulated by setting the plate thickness to be sufficiently small. The additional free surface formulation can be used as an alternative representation of open water. This technique is slightly more complicated, but is also slightly more accurate and more practical under certain circumstances, since it has two fewer unknowns.

For each free surface region, the matching and edge matrices (**M**, **N**, **C**) are redefined using the set of free surface eigenfunctions defined in Section 4.2.1. No edge conditions exist for free surface regions. For the free surface, each matrix in (4.61) is therefore zero. Due to the lack of damped modes at the free surface, the free surface **M** and **N** matrices are now square matrices of size (M+1). The structure of the large matrices **M** and **E** remain the same and have the same number of rows, but have two less columns per free surface region.

5

The Green Function Method

The Green function was first derived for infinite depth by Squire and Dixon (2001) and for finite depth by Evans and Porter (2003). We include this solution method as it is a useful tool to verify the results of the MEEM (Section 7). In this chapter, we re-express the derivation of Evans and Porter (2003) and Porter and Evans (2006) to be consistent with our notation. Note that our derivation of the GFM equations is new, as is the application of the GFM to various edge conditions (Section 6).

The Green Function Method (GFM) considers the entire free surface to be occupied by a floating elastic plate, with identical properties throughout and a set of discontinuities, i.e. cracks, at x'_n where $n = 1, ..., \Lambda - 1$. Note that this is problem can be solved using MEEM with Λ identical plates. The Free-Surface Green Function for a floating elastic plate is given by

$$\begin{aligned} G(x, x', z) &= \sum_{m=-2}^{\infty} \frac{k(m) \sin\left(k(m)h\right) \cos\left(k(m)(z+h)\right)}{2\alpha\kappa(m)\mathcal{C}(k(m))} e^{-\kappa(m)|x-x'|}, \\ \mathcal{C}(k(m)) &= \frac{1}{2}\left(h - \frac{(5\beta k(m)^4 + 1 - \alpha\gamma)\sin^2\left(k(m)h\right)}{\alpha}\right), \end{aligned} \tag{5.1}$$

and satisfies the following equations

$$\begin{aligned} \nabla^2 G &= 0, & -h < z < 0, \\ G_z &= 0, & z = -h, \\ \left(\beta(\partial_x^2 - k_y^2)^2 - \gamma\alpha + 1\right) G_z - \alpha G &= \delta(x - x'), & z = 0, \end{aligned} \tag{5.2}$$

where $k(m)$ are the solutions given by (4.3). Green's second identity can be applied as ϕ and G are both twice continuously differentiable on $\mathcal{U}$, where $\mathcal{U}$ is the area bounded by the contour $\mathcal{S}$, which is defined by the boundaries of the sea floor, sea surface and the extent of the floating plate (Figure 5.1).

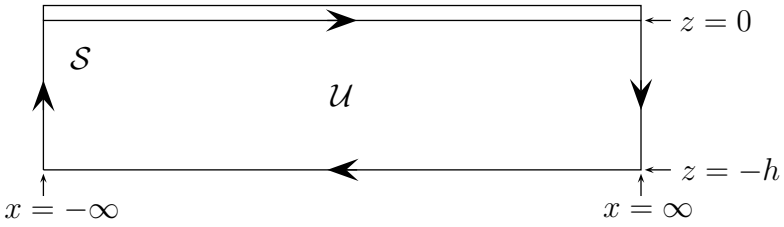

Figure 5.1: A schematic diagram showing the area, $\mathcal{U}$ bounded by the contour $\mathcal{S}$, which is defined by the boundaries of the sea floor ($-h \leq z \leq 0$) and the extent of the floating plate ($-\infty \leq x \leq \infty$).

Hence by Green's second identity,

$$\int_{\mathcal{U}} \left(G\nabla^2\phi - \phi\nabla^2 G\right)\, dV = \oint_{\partial\mathcal{U}} \left(G\phi_n - \phi G_n\right) d\mathcal{S}, \tag{5.3}$$

where n is the outward plane normal to the boundary, $\mathcal{S}$.

Our governing equations for G and ϕ imply that the L.H.S of Green's second identity is zero so that

$$0 = \oint_{\partial\mathcal{U}} \left(G\phi_n - \phi G_n\right)\, d\mathcal{S}. \tag{5.4}$$

Expanding (5.4) gives

$$\begin{aligned} 0 = \lim_{N\to\infty}\Bigg[& \int_{-N}^{N} (G\phi_z|_{z=0} - \phi G_z|_{z=0})\, dx \\ + & \int_{-h}^{0} (G\phi_x|_{x=N} - \phi G_x|_{x=N})\, dz \\ - & \int_{-N}^{N} (G\phi_{-z}|_{z=-h} - \phi G_{-z}|_{z=-h})\, dx \\ - & \int_{-h}^{0} (G\phi_{-x}|_{x=-N} - \phi G_{-x}|_{x=-N})\, dz \Bigg], \end{aligned} \tag{5.5}$$

where we take the limit as N goes to infinity. We evaluate the four integrals in (5.5) separately.

The first integral in (5.5) is given by

$$\int_{-\infty}^{\infty} (G(x,x')\phi_z(x') - \phi(x')G_z(x,x'))\, dx. \tag{5.6}$$

We integrate by parts remembering that ϕ_z is continuous everywhere except at $x = x'_n$ so that

$$\int_{-\infty}^{\infty} (\partial_x^4\phi_z)G_z dx = \sum_{n=1}^{\Lambda-1} \int_{-\infty}^{x'_n} (\partial_x^4\phi_z)G_z dx + \int_{x'_n}^{\infty} (\partial_x^4\phi_z)G_z dx, \tag{5.7}$$

where

$$\begin{aligned} \textstyle\int_a^b (\partial_x^4\phi_z)G_z dx = & \textstyle\int_a^b \phi_z(\partial_x G)dx \\ & -\phi_z(b)(\partial_x^3 G(b)) + \phi_z(a)(\partial_x^3 G(a)) \\ & +(\partial_x\phi_z(b))(\partial_x^2 G(b)) - (\partial_x\phi_z(a))(\partial_x^2 G(a)) \\ & -(\partial_x^2\phi_z(b))(\partial_x G(b)) + (\partial_x^2\phi_z(a))(\partial_x G(a)) \\ & +(\partial_x^3\phi_z(b))G(b) - (\partial_x^3\phi_z(a))G(a). \end{aligned} \tag{5.8}$$

and obtain

$$\int_{-\infty}^{\infty} \left\{ \frac{1}{\alpha}\left(\beta(\partial_x^2 - k_y^2)^2) - \gamma\alpha + 1\right) G_z(x'_n, x') - G(x'_n, x') \right\} \phi_z(x) dx$$

$$\begin{aligned} +\frac{\beta}{\alpha}\sum_{n=1}^{\Lambda-1}\Bigg(& -(\partial_x^3 - 2k_y^2\partial_x)G_z(x'_n,x')[\phi_z]_n + (\partial_x^2 - 2k_y^2)G_z(x'_n,x')\partial_x[\phi_z]_n \\ & -\partial_x G_z(x'_n,x')\partial_x^2[\phi_z]_n + G_z(x'_n,x')\partial_x^3[\phi_z]_n \Bigg) \end{aligned} \tag{5.9}$$

$$\begin{aligned} & +\phi_z(-N)\partial_x^3 G_z(-N) - \partial_x\phi_z(-N)\partial_x^2 G_z(-N) \\ & \quad +\partial_x^2\phi_z(-N)\partial_x G_z(-N) - \partial_x^3\phi_z(-N)G_z(-N), \end{aligned}$$

where $[\phi_z]_n$ denotes the jump in ϕ_z at $x = x'_n$. The integral in (5.9) can be simplified using the delta function property of the Green Function, and the last four terms of (5.9) can be simplified, so that (5.9) reduces to

$$\begin{aligned}\frac{1}{\alpha}\phi_z + \frac{\beta}{\alpha}4k(0)^2\kappa(0)^3 I\mathcal{G}(0)e^{-\kappa(0)x'}\sin^2(k(0)h) \\ +\frac{\beta}{\alpha}\sum_{n=1}^{\Lambda-1}\Big(-(\partial_x^3 - 2k_y^2\partial_x)G_z(x'_n,x')[\phi_z]_n + (\partial_x^2 - 2k_y^2)G_z(x'_n,x')\partial_x[\phi_z]_n \\ -\partial_x G_z(x'_n,x')\partial_x^2[\phi_z]_n + G_z(x'_n,x')\partial_x^3[\phi_z]_n\Big).\end{aligned} \tag{5.10}$$

The second and third term in (5.5) give zero. The final term is given by

$$\int_{-h}^{0}(G(-N,x',z)\phi_{-x}(-N,x',z) - \phi(-N,x',z)G_{-x}(-N,x',z))\,dz. \tag{5.11}$$

From Section 4, ϕ under the first plate is

$$\phi_1(x,z) = Ie^{-\kappa(0)(x)}\cos(k(0)(z+h)) + \sum_{m=-2}^{M} Re^{\kappa(m)(x)}\cos(k(m)(z+h), \tag{5.12}$$

where $I = 1/k(0)$ so that

$$\phi_z^I = e^{-\kappa(0)x}\sin(k(0)(z+h)).$$

We simplify G as

$$G(x,x',z) = \sum_{m=-2}^{M}\mathcal{G}(m)e^{-\kappa(m)|x-x'|}\cos(k(m)(z+h)), \tag{5.13}$$

where

$$\mathcal{G} = \frac{k(n)\sin(k(n)h)}{2\alpha\kappa(n)\mathcal{C}(k(n))}, \tag{5.14}$$

so that (5.11), under the first plate, can be expressed as

$$\begin{aligned}-\int_{-h}^{0}\mathcal{G}(0)e^{-\kappa(0)|-N-x'|}\cos(k(0)(z+h))(-\kappa(0)Ie^{\kappa(0)N}\cos(k(0)(z+h)) \\ +\kappa(0)Re^{-\kappa(0)N}\cos(k(0)(z+h))) \\ -\kappa(0)\mathcal{G}(0)e^{-\kappa(0)|-N-x'|}\cos(k(0)(z+h))(Ie^{\kappa(0)N}\cos(k(0)(z+h)) \\ +Re^{-\kappa(0)N}\cos(k(0)(z+h)))dz.\end{aligned} \tag{5.15}$$

Note that the reflected terms in (5.15) vanish. The reflected and transmitted terms under

the middle and final plates also vanish so that (5.11) simplifies to

$$\int_{-h}^{0} 2I\kappa(0)\mathcal{G}(0)e^{-\kappa(0)x'}\cos^2(k(0)(z+h))dz. \tag{5.16}$$

From Evans and Porter (2003), (5.16) gives

$$2I\kappa(0)\mathcal{G}(0)e^{-\kappa(0)x'}\left(C(k(0)) + \frac{\beta}{\alpha}2k(0)^2\kappa(0)^2\sin^2(k(0)(h))\right). \tag{5.17}$$

Expanding gives

$$\frac{1}{\alpha}Ik(0)e^{-k(0)x}\sin(k(0)h) + \frac{\beta}{\alpha}4Ik(0)^2\kappa(0)^3\mathcal{G}\sin^2(k(0)h)e^{-k(0)x}, \tag{5.18}$$

or simply

$$\frac{1}{\alpha}\phi_z^I + \frac{\beta}{\alpha}4Ik(0)^2\kappa(0)^3\mathcal{G}\sin^2(k(0)h)e^{-k(0)x}. \tag{5.19}$$

Combining (5.10) and (5.19), we can now express (5.5) as

$$\begin{aligned}\frac{1}{\alpha}\phi_z + \frac{\beta}{\alpha}\sum_{n=1}^{\Lambda-1}\big(&-(\partial_x^3 - 2k_y^2\partial_x)G_z(x'_n,x')[\phi_z]_n + (\partial_x^2 - 2k_y^2)G_z(x'_n,x')\partial_x[\phi_z]_n \\ &-\partial_x G_z(x'_n,x')\partial_x^2[\phi_z]_n + G_z(x'_n,x')\partial_x^3[\phi_z]_n\big) - \frac{1}{\alpha}\phi_z^{\mathrm{I}}.\end{aligned} \tag{5.20}$$

The boundary conditions are given in terms of η, so we multiply (5.20) by $i\omega$ and rearrange to give

$$\begin{aligned}\eta(x) = \eta^I + \beta\sum_{n=1}^{\Lambda-1}\big(&(\partial_x^3 - 2k_y^2\partial_x)G_z[\eta]_n - (\partial_x^2 - 2k_y^2)G_z[\partial_x\eta]_n \\ &+\partial_x G_z[\partial_x^2\eta]_n - G_z[\partial_x^3\eta]_n\big).\end{aligned} \tag{5.21}$$

We can solve (5.21) by applying the free edge conditions (3.12) and (3.13). These edge conditions imply $[\partial_x^2\eta]_n = k_y^2\nu[\eta]_n$ and $[\partial_x^3\eta]_n = k_y^2(2-\nu)[\partial_x\eta]_n$ so that

$$\eta = \eta^{\mathrm{I}} + \beta\sum_{n=1}^{\Lambda-1}\big((\partial_x^3 G_z - k_y^2(2-\nu)\partial_x G_z)[\eta]_n - (\partial_x^2 G_z - k_y^2\nu G_z)[\partial_x\eta]_n\big), \tag{5.22}$$

where

$$\begin{aligned}
G_z|_{z=0} &= -\sum_{m=-2}^{\infty} \frac{k(m)^2 \sin^2(k(m)h)}{2\alpha\kappa(m)\mathcal{C}(k(m))} e^{-\kappa(m)|x-x'|}, \\
\partial_x G_z|_{z=0} &= -\mathrm{sgn}(x-x') \sum_{m=-2}^{\infty} \frac{k(m)^2 \sin^2(k(m)h)}{2\alpha\mathcal{C}(k(m))} e^{-\kappa(m)|x-x'|}, \\
\partial_x^2 G_z|_{z=0} &= -\sum_{m=-2}^{\infty} \frac{k(m)^2\kappa(m) \sin^2(k(m)h)}{2\alpha\mathcal{C}(k(m))} e^{-\kappa(m)|x-x'|}, \\
\partial_x^3 G_z|_{z=0} &= -\mathrm{sgn}(x-x') \sum_{m=-2}^{\infty} \frac{k(m)^2\kappa(m)^2 \sin^2(k(m)h)}{2\alpha\mathcal{C}(k(m))} e^{-\kappa(m)|x-x'|}.
\end{aligned}$$

To solve for the free edge, we apply edge condition (3.12),

$$0 = \left(\partial_x^3 - k_y^2(2-\nu)\partial_x\right)\eta. \tag{5.23}$$

Expanding gives

$$\begin{aligned}
0 = &\left(\partial_x^3 - k_y^2(2-\nu)\partial_x\right)\eta^I \\
&+ \left(\partial_x^3 - k_y^2(2-\nu)\partial_x\right) \sum_{n=1}^{\Lambda-1} \left(\partial_x^3 G_z - k_y^2(2-\nu)\partial_x G_z\right)[\eta]_n \\
&- \left(\partial_x^3 - k_y^2(2-\nu)\partial_x\right) \sum_{n=1}^{\Lambda-1} \left(\partial_x^2 G_z - k_y^2\nu G_z\right)[\partial_x\eta]_n,
\end{aligned} \tag{5.24}$$

which gives

$$\begin{aligned}
0 = &-(\kappa(0)^3 - k_y^2\kappa(0)(2-\nu))e^{-\kappa(0)x} \\
&+ \left(\kappa(m)^3 - \kappa(m)k_y^2(2-\nu)\right)^2 \\
&\quad \left(\sum_{n=1}^{\Lambda-1}\sum_{m=-2}^{\infty} \mathcal{C}(k(m))^{-1} k(m) \sin^2(k(m)h) e^{-\kappa(m)|x-x'|}[\eta]_n\right) \\
&-\mathrm{sgn}(x-x')(\kappa(m)^3 - \kappa(m)k_y^2(2-\nu))(\kappa(m)^2 - k_y^2\nu) \\
&\quad \left(\sum_{n=1}^{\Lambda-1}\sum_{m=-2}^{\infty} \mathcal{C}(k(m))^{-1} k(m) \sin^2(k(m)h) e^{-\kappa(m)|x-x'|}[\partial_{x'}\eta]_n\right).
\end{aligned} \tag{5.25}$$

Edge condition (3.13) gives

$$0 = \left(\partial_x^2 - k_y^2\nu\right)\eta. \tag{5.26}$$

Expanding gives

$$\begin{aligned} 0 = &\left(\partial_x^2 - k_y^2\nu\right)\eta^I \\ &+ \left(\partial_x^2 - k_y^2\nu\right)\sum_{n=1}^{\Lambda-1}\left(\partial_x^3 G_z - k_y^2(2-\nu)\partial_x G_z\right)[\eta]_n \\ &- \left(\partial_x^2 - k_y^2\nu\right)\sum_{n=1}^{\Lambda-1}\left(\partial_x^2 G_z - k_y^2\nu G_z\right)[\partial_x\eta]_n, \end{aligned} \tag{5.27}$$

which gives

$$\begin{aligned} 0 = &(\kappa(0)^2 - k_y^2\nu)e^{-\kappa(0)x} \\ &-\mathrm{sgn}(x-x')\left(\kappa(m)^2 - k_y^2\nu\right)\left(\kappa(m)^3 - \kappa(m)k_y^2(2-\nu)\right) \\ &\left(\sum_{n=1}^{\Lambda-1}\sum_{m=-2}^{\infty}\mathcal{C}(k(m))^{-1}k(m)\sin^2(k(m)h)e^{-\kappa(m)|x-x'|}[\eta]_n\right) \\ &+(\kappa(m)^2 - k_y^2\nu)^2 \\ &\left(\sum_{n=1}^{\Lambda-1}\sum_{m=-2}^{\infty}\mathcal{C}(k(m))^{-1}k(m)\sin^2(k(m)h)e^{-\kappa(m)|x-x'|}[\partial_x\eta]_n\right). \end{aligned} \tag{5.28}$$

The jump conditions $[\eta]_n$ and $[\partial_x\eta]_n$ can be solved by solving the edge conditions simultaneously. The reflection and transmission coefficients, R_1 and T_Λ can now be found by taking the limit of η as $x \to \pm\infty$ so that

$$\begin{aligned} R_1 &= \lim_{x\to-\infty}\big(\eta^I + \beta\sum_{n=1}^{\Lambda-1}\big((\partial_x^3 G_z - k_y^2(2-\nu)\partial_x G_z)[\eta]_n \\ &\qquad -\beta(\partial_x^2 G_z - k_y^2\nu G_z)[\partial_x\eta]_n\big), \\ &= e^{\kappa(0)r_1}\Bigg(\frac{\beta k(0)\sin^2(k(0)h)}{2\alpha\mathcal{C}(k(0))} \\ &\qquad \sum_{n=1}^{\Lambda-1}\big((\kappa(0)^3 - \kappa(0)k_y^2(2-\nu)[\eta]_n + (\kappa(0)^2 - k_y^2\nu)[\partial_x\eta]_n\big)\Bigg), \end{aligned} \tag{5.29}$$

and

$$
\begin{aligned}
T_\Lambda &= \lim_{x\to\infty}\big(\eta^I + \beta\sum_{n=1}^{\Lambda-1}\big((\partial_x^3 G_z - k_y^2(2-\nu)\partial_x G_z)[\eta]_n \\
&\qquad -\beta(\partial_x^2 G_z - k_y^2\nu G_z)[\partial_x\eta]_n\big), \\
&= e^{-\kappa(0)r_{\Lambda-1}}\Bigg(1 - \frac{\beta k_1(0)\sin^2(k_1(0)h)}{2\alpha\mathcal{C}(k_1(0))} \\
&\qquad \sum_{n=1}^{\Lambda-1}\big((\kappa_1(0)^3 - \kappa_1(0)k_y^2(2-\nu)[\eta]_n - (\kappa_1(0)^2 - k_y^2\nu)[\partial_x\eta]_n\big)\Bigg).
\end{aligned}
\tag{5.30}
$$

6

Articulated Plates

6.1 Introduction

Within this chapter, we consider plates with non free edges i.e. plates with a non zero bending moment and/or non zero shear force at each edge. Solving for clamped, simply supported or sliding plates is relatively straightforward and we solve for each case using both the MEEM and the GFM.

A slightly more complicated case is when the plates are connected by springs. Such a problem can be applied to Very Large Floating Structures (VLFS)'s, which are often constructed by welding together a series of plates. During the process of welding, the joints behave as vertical and rotational springs connecting the neighbouring plates with a stiffness varying from zero (disconnected) to infinity (connected). It is important to determine the relative motions between two adjacent plates, and the bending moment and shear force on the joint due to waves, so that the assembly can progress smoothly and efficiently (Xia et al., 2000). The problem of multiple plates connected by springs, where each plate is assumed to have the same flexural rigidity, has been solved by (Xia et al., 2000). By considering the symmetry and asymmetry of the problem, Xia et al. (2000) defines the potential as the sum of the incoming wave potential, the singular moment

loading potential and the singular slope disturbance potential. The potential is solved by applying the connector conditions which are given by (3.20). Karmakar and Sahoo (2005) solve a similar problem where they consider the geometrical symmetry and solve by the direct application of a mixed-type Fourier transform and eigenfunction matching at the plate boundaries. Both Xia et al. (2000) and Karmakar and Sahoo (2005) conclude that the hydroelastic properties of the articulated plates are strongly dependent on the stiffness of the connectors and the incoming wave frequency.

A special case of springed connections is hinged connections. Pontoon type structures consisting of several plates connected by hinged joints, have been proposed for mobile offshore bases. The hinges are desirable as they reduce the magnitude of the bending loads compared to a single rigid structure of the same overall length (Newman, 2005). Also, assembling a series of plates connected by hinges is logistically easier than trying to construct one large structure. The hydrodynamic behaviour of hinged structures is analysed in Xia et al. (2000), Lee and Newman (2000), and Newman (2005). We can solve for the hinge case by redefining the springed edge conditions (3.20) by taking the limit as s_r approaches ∞ and taking $s_v = 0$ to give (3.21) (Xia et al., 2000).

In this section, we solve for each articulated edge condition using both the MEEM and the GFM. A summary of this theory has been submitted for publication (Kohout and Meylan, 2008a). The results are compared in Section 7.

6.2 Matched Eigenfunction Expansion Method

6.2.1 Simple Connections

Solving for clamped, simply supported or sliding plates using the MEEM only requires editing the edge matrices, $\mathbf{E}^{+}_{T_\mu}$, $\mathbf{E}^{+}_{R_\mu}$, $\mathbf{E}^{-}_{T_\mu}$ and $\mathbf{E}^{-}_{R_\mu}$ as defined in (4.45). The problem is then solved using the same method as for a set of plates with free edges (Section 4.4.1). Firstly, we consider plates which are clamped at each edge so that (3.14) and (3.15) apply

giving

$$\begin{aligned}
\mathbf{E}^-(1,m)_{T_\mu} &= k_\mu(m)\kappa_\mu(m)\tan\left(k_\mu(m)h\right),\\
\mathbf{E}^+(1,m)_{T_\mu} &= k_\mu(m)\kappa_\mu(m)e^{-\kappa_\mu(m)(r_\mu-l_\mu)}\tan\left(k_\mu(m)h\right),\\
\mathbf{E}^-(1,m)_{R_\mu} &= -k_\mu(m)\kappa_\mu(m)e^{\kappa_\mu(m)(l_\mu-r_\mu)}\tan\left(k_\mu(m)h\right),\\
\mathbf{E}^+(1,m)_{R_\mu} &= -k_\mu(m)\kappa_\mu\tan\left(k_\mu(m)h\right),\\
\\
\mathbf{E}^-(2,m)_{T_\mu} &= -k_\mu(m)\tan\left(k_\mu(m)h\right),\\
\mathbf{E}^+(2,m)_{T_\mu} &= -k_\mu(m)e^{-\kappa_\mu(m)(r_\mu-l_\mu)}\tan\left(k_\mu(m)h\right),\\
\mathbf{E}^-(2,m)_{R_\mu} &= -k_\mu(m)e^{\kappa_\mu(m)(l_\mu-r_\mu)}\tan\left(k_\mu(m)h\right),\\
\mathbf{E}^+(2,m)_{R_\mu} &= -k_\mu(m)\tan\left(k_\mu(m)h\right).
\end{aligned} \tag{6.1}$$

Similarly, simply supported edge conditions defined by (3.16) and (3.17) give

$$\begin{aligned}
\mathbf{E}^-(1,m)_{T_\mu} &= (\kappa_\mu(m)^2-\nu k_y^2)(-k_\mu(m)\tan\left(k_\mu(m)h\right)),\\
\mathbf{E}^+(1,m)_{T_\mu} &= (\kappa_\mu(m)^2-\nu k_y^2)(-k_\mu(m)e^{-\kappa_\mu(m)(r_\mu-l_\mu)}\tan\left(k_\mu(m)h\right)),\\
\mathbf{E}^-(1,m)_{R_\mu} &= (\kappa_\mu(m)^2-\nu k_y^2)(-k_\mu(m)e^{\kappa_\mu(m)(l_\mu-r_\mu)}\tan\left(k_\mu(m)h\right)),\\
\mathbf{E}^+(1,m)_{R_\mu} &= (\kappa_\mu(m)^2-\nu k_y^2)(-k_\mu(m)\tan\left(k_\mu(m)h\right)).\\
\\
\mathbf{E}^-(2,m)_{T_\mu} &= -k_\mu(m)\tan\left(k_\mu(m)h\right),\\
\mathbf{E}^+(2,m)_{T_\mu} &= -k_\mu(m)e^{-\kappa_\mu(m)(r_\mu-l_\mu)}\tan\left(k_\mu(m)h\right),\\
\mathbf{E}^-(2,m)_{R_\mu} &= -k_\mu(m)e^{\kappa_\mu(m)(l_\mu-r_\mu)}\tan\left(k_\mu(m)h\right),\\
\mathbf{E}^+(2,m)_{R_\mu} &= -k_\mu(m)\tan\left(k_\mu(m)h\right).
\end{aligned} \tag{6.2}$$

Finally, the non-physical case of sliding edge conditions defined by (3.18) and (3.19) give

$$\begin{aligned}
\mathbf{E}^-(1,m)_{T_\mu} &= \left(\kappa_\mu(m)^3-k_y^2\kappa_\mu(2-\nu)\right)\left(k_\mu(m)\tan\left(k_\mu(m)h\right)\right),\\
\mathbf{E}^+(1,m)_{T_\mu} &= \left(\kappa_\mu(m)^3-k_y^2\kappa_\mu(2-\nu)\right)\left(k_\mu(m)e^{-\kappa_\mu(m)(r_\mu-l_\mu)}\tan\left(k_\mu(m)h\right)\right),\\
\mathbf{E}^-(1,m)_{R_\mu} &= \left(\kappa_\mu(m)^3-k_y^2\kappa_\mu(2-\nu)\right)\left(-k_\mu(m)e^{\kappa_\mu(m)(l_\mu-r_\mu)}\tan\left(k_\mu(m)h\right)\right),\\
\mathbf{E}^+(1,m)_{R_\mu} &= \left(\kappa_\mu(m)^3-k_y^2\kappa_\mu(2-\nu)\right)\left(-k_\mu(m)\tan\left(k_\mu(m)h\right)\right),\\
\\
\mathbf{E}^-(2,m)_{T_\mu} &= k_\mu(m)\kappa_\mu(m)\tan\left(k_\mu(m)h\right),\\
\mathbf{E}^+(2,m)_{T_\mu} &= k_\mu(m)\kappa_\mu(m)e^{-\kappa_\mu(m)(r_\mu-l_\mu)}\tan\left(k_\mu(m)h\right),\\
\mathbf{E}^-(2,m)_{R_\mu} &= -k_\mu(m)\kappa_\mu(m)e^{\kappa_\mu(m)(l_\mu-r_\mu)}\tan\left(k_\mu(m)h\right),\\
\mathbf{E}^+(2,m)_{R_\mu} &= -k_\mu(m)\kappa_\mu\tan\left(k_\mu(m)h\right).
\end{aligned} \tag{6.3}$$

6.2.2 Springed Connections

In this section we solve for plates connected by springs using a slightly different version of the MEEM presented in Section 4.4.1. Here, each plate is connected by a series of flexural rotational and vertical linear springs so that the edge conditions are redefined by (3.20). We first re-arrange (3.20) to give

$$\begin{aligned}
\eta(r_\mu) &= \left(\frac{\beta}{s_v}\left(\frac{\partial^3}{\partial x^3} - k_y^2(2-\nu)\frac{\partial}{\partial x}\right) + 1\right)\eta(l_{\mu+1}),\\
-\eta(l_{\mu+1}) &= \left(\frac{\beta}{s_v}\left(\frac{\partial^3}{\partial x^3} - k_y^2(2-\nu)\frac{\partial}{\partial x}\right) - 1\right)\eta(r_\mu),\\
\frac{\partial\eta(r_\mu)}{\partial x} &= \left(-\frac{\beta}{s_r}\left(\frac{\partial^2}{\partial x^2} - k_y^2\nu\right) + \frac{\partial}{\partial x}\right)\eta(l_{\mu+1}),\\
\frac{\partial\eta(l_{\mu+1})}{\partial x} &= \left(\frac{\beta}{s_r}\left(\frac{\partial^2}{\partial x^2} - k_y^2\nu\right) + \frac{\partial}{\partial x}\right)\eta(r_\mu).
\end{aligned} \tag{6.4}$$

Using the definition of η given by (4.25), we expand each edge condition in (6.4). Expanding the first edge condition for the boundary between the μ^{th} and $(\mu+1)^{th}$ plate, gives

$$\begin{aligned}
&\sum_{m=-2}^{M}\Big[-T_\mu(m)k_\mu(m)e^{-\kappa_\mu(m)(r_\mu-l_\mu)}\tan\left(k_\mu(m)h\right) - R_\mu(m)k_\mu(m)\tan\left(k_\mu(m)h\right)\Big]\\
&= \sum_{m=-2}^{M}\Big[T_{\mu+1}(m)k_{\mu+1}(m)\tan\left(k_{\mu+1}(m)h\right)\\
&\qquad\left(\frac{\beta}{s_v}\left(\kappa_{\mu+1}^3(m) - k_y^2\kappa_{\mu+1}(2-\nu)\right) - 1\right)\\
&\qquad -R_{\mu+1}(m)k_{\mu+1}(m)e^{\kappa_{\mu+1}(m)(l_{\mu+1}-r_{\mu+1})}\tan\left(k_{\mu+1}(m)h\right)\\
&\qquad\left(\frac{\beta}{s_v}\left(\kappa_{\mu+1}^3(m) - k_y^2\kappa_{\mu+1}(2-\nu)\right) + 1\right)\Big].
\end{aligned} \tag{6.5}$$

Expanding the second edge condition for the boundary between the μ^{th} and $(\mu+1)^{th}$ plate, gives

$$\begin{aligned}
&\sum_{m=-2}^{M}\Bigg[T_\mu(m)k_\mu(m)e^{-\kappa_\mu(m)(r_\mu-l_\mu)}\tan\left(k_\mu(m)h\right)\\
&\qquad\left(\frac{\beta}{s_v}\left(\kappa_{\mu+1}^3(m)-k_y^2\kappa_{\mu+1}(2-\nu)\right)+1\right)\\
&\quad+R_\mu(m)k_\mu(m)\tan\left(k_\mu(m)h\right)\left(-\frac{\beta}{s_v}\left(\kappa_{\mu+1}^3(m)-k_y^2\kappa_{\mu+1}(2-\nu)\right)+1\right)\Bigg]\\
&=\sum_{m=-2}^{M}\Bigg[T_{\mu+1}(m)k_{\mu+1}(m)\tan\left(k_{\mu+1}(m)h\right)\\
&\qquad+R_{\mu+1}(m)k_{\mu+1}(m)e^{\kappa_{\mu+1}(m)(l_{\mu+1}-r_{\mu+1})}\tan\left(k_{\mu+1}(m)h\right)\Bigg].
\end{aligned}\tag{6.6}$$

Expanding the third edge condition for the boundary between the μ^{th} and $(\mu+1)^{th}$ plate, gives

$$\begin{aligned}
&\sum_{m=-2}^{M}\Bigg[T_\mu(m)k_\mu(m)\kappa_\mu(m)e^{-\kappa_\mu(m)(r_\mu-l_\mu)}\tan\left(k_\mu(m)h\right)\\
&\qquad-R_\mu(m)k_\mu(m)\kappa_\mu(m)\tan\left(k_\mu(m)h\right)\Bigg]\\
&=\sum_{m=-2}^{M}\Bigg[T_{\mu+1}(m)k_{\mu+1}(m)\tan\left(k_{\mu+1}(m)h\right)\left(\frac{\beta}{s_r}\left(\kappa_{\mu+1}^2(m)-k_y^2\nu\right)+\kappa_{\mu+1}\right)\\
&\qquad+R_{\mu+1}(m)k_{\mu+1}(m)e^{\kappa_{\mu+1}(m)(l_{\mu+1}-r_{\mu+1})}\tan\left(k_{\mu+1}(m)h\right)\\
&\qquad\left(\frac{\beta}{s_r}\left(\kappa_{\mu+1}^2(m)-k_y^2\nu\right)-\kappa_\mu\right)\Bigg].
\end{aligned}\tag{6.7}$$

Expanding the fourth edge condition for the boundary between the μ^{th} and $(\mu+1)^{th}$ plate, gives

$$\begin{aligned}
&\sum_{m=-2}^{M}\Bigg[T_\mu(m)k_\mu(m)e^{-\kappa_\mu(m)(r_\mu-l_\mu)}\tan\left(k_\mu(m)h\right)\left(-\frac{\beta}{s_r}\left(\kappa_\mu^2(m)-k_y^2\nu\right)+\kappa_\mu\right)\\
&\qquad -R_\mu(m)k_\mu(m)\tan\left(k_\mu(m)h\right)\left(\frac{\beta}{s_r}\left(\kappa_\mu^2(m)-k_y^2\nu\right)+\kappa_\mu\right)\Bigg]\\
&=\sum_{m=-2}^{M}\Bigg[T_{\mu+1}(m)k_{\mu+1}(m)\kappa_{\mu+1}(m)\tan\left(k_{\mu+1}(m)h\right)\\
&\qquad -R_{\mu+1}(m)k_{\mu+1}(m)\kappa_{\mu+1}e^{\kappa_{\mu+1}(m)(l_{\mu+1}-r_{\mu+1})}\tan\left(k_{\mu+1}(m)h\right)\Bigg].
\end{aligned} \tag{6.8}$$

The edge conditions of the first and second plate can be expressed as

$$I\begin{pmatrix}\mathbf{E}_{R_1}^{+}(1,0)\\ \mathbf{E}_{R_1}^{+}(2,0)\end{pmatrix}+\mathbf{E}_{R_1}^{+}\mathbf{R}_1=\mathbf{E}_{T_2}^{-}\mathbf{T}_2+\mathbf{E}_{R_2}^{-}\mathbf{R}_2. \tag{6.9}$$

The μ^{th} and $(\mu+1)^{th}$ edge conditions can be expressed as

$$\mathbf{E}_{T_\mu}^{+}\mathbf{T}_\mu+\mathbf{E}_{R_\mu}^{+}\mathbf{R}_\mu \;=\; \mathbf{E}_{T_{\mu+1}}^{-}\mathbf{T}_{\mu+1}+\mathbf{E}_{R_{\mu+1}}^{-}\mathbf{R}_{\mu+1}. \tag{6.10}$$

The final $\Lambda^{th}-1$ and Λ^{th} edge conditions can be expressed as

$$\mathbf{E}_{T_{\Lambda-1}}^{+}\mathbf{T}_{\Lambda-1}+\mathbf{E}_{R_{\Lambda-1}}^{+}\mathbf{R}_{\Lambda-1}=\mathbf{E}_{T_\mu}^{-}\mathbf{T}_\mu, \tag{6.11}$$

where $\mathbf{E}^+_{T_\mu}$, $\mathbf{E}^+_{R_\mu}$, $\mathbf{E}^-_{T_\mu}$, $\mathbf{E}^-_{T_\mu}$ are 4 by M+3 matrices given by

$$
\begin{aligned}
\mathbf{E}^-_{T_\mu}(1,m) &= k_\mu(m)\tan(k_\mu(m)h)\left(\tfrac{\beta}{s_v}\left(\kappa^3_\mu(m)-k_y^2\kappa_\mu(m)(2-\nu)\right)-1\right),\\
\mathbf{E}^-_{R_\mu}(1,m) &= -k_\mu(m)\tan(k_\mu(m)h)e^{\kappa_\mu(m)(l_\mu-r_\mu)}\\
&\quad\left(\tfrac{\beta}{s_v}\left(\kappa^3_\mu(m)-k_y^2\kappa_\mu(m)(2-\nu)\right)+1\right),\\
\mathbf{E}^+_{T_\mu}(1,m) &= -k_\mu(m)\tan(k_\mu(m)h)e^{-\kappa_\mu(m)(r_\mu-l_\mu)},\\
\mathbf{E}^+_{R_\mu}(1,m) &= -k_\mu(m)\tan(k_\mu(m)h),\\
\\
\mathbf{E}^-_{T_\mu}(2,m) &= k_\mu(m)\tan(k_\mu(m)h),\\
\mathbf{E}^-_{R_\mu}(2,m) &= k_\mu(m)\tan(k_\mu(m)h)e^{\kappa_\mu(m)(l_\mu-r_\mu)},\\
\mathbf{E}^+_{T_\mu}(2,m) &= k_\mu(m)\tan(k_\mu(m)h)e^{-\kappa_\mu(m)(r_\mu-l_\mu)}\\
&\quad\left(\tfrac{\beta}{s_v}\left(\kappa^3_\mu(m)-k_y^2\kappa_\mu(m)(2-\nu)\right)+1\right),\\
\mathbf{E}^+_{R_\mu}(2,m) &= -k_\mu(m)\tan(k_\mu(m)h)\left(\tfrac{\beta}{s_v}\left(\kappa^3_\mu(m)-k_y^2\kappa_\mu(m)(2-\nu)\right)-1\right),\\
\\
\mathbf{E}^-_{T_\mu}(3,m) &= k_\mu(m)\tan(k_\mu(m)h)\left(\tfrac{\beta}{s_r}\left(\kappa^2_\mu(m)-k_y^2\nu\right)+\kappa_\mu(m)\right),\\
\mathbf{E}^-_{R_\mu}(3,m) &= k_\mu(m)\tan(k_\mu(m)h)e^{\kappa_\mu(m)(l_\mu-r_\mu)}\left(\tfrac{\beta}{s_r}\left(\kappa^2_\mu(m)-k_y^2\nu\right)-\kappa_\mu(m)\right),\\
\mathbf{E}^+_{T_\mu}(3,m) &= k_\mu(m)\kappa_\mu\tan(k_\mu(m)h)e^{-\kappa_\mu(m)(r_\mu-l_\mu)},\\
\mathbf{E}^+_{R_\mu}(3,m) &= -k_\mu(m)\kappa_\mu\tan(k_\mu(m)h),\\
\\
\mathbf{E}^-_{T_\mu}(4,m) &= k_\mu(m)\kappa_\mu\tan(k_\mu(m)h),\\
\mathbf{E}^-_{R_\mu}(4,m) &= -k_\mu(m)\kappa_\mu\tan(k_\mu(m)h)e^{\kappa_\mu(m)(l_\mu-r_\mu)},\\
\mathbf{E}^+_{T_\mu}(4,m) &= -k_\mu(m)\tan(k_\mu(m)h)e^{-\kappa_\mu(m)(r_\mu-l_\mu)}\\
&\quad\left(\tfrac{\beta}{s_r}\left(\kappa^2_\mu(m)-k_y^2\nu\right)-\kappa_\mu(m)\right),\\
\mathbf{E}^+_{R_\mu}(4,m) &= -k_\mu(m)\tan(k_\mu(m)h)\left(\tfrac{\beta}{s_r}\left(\kappa^2_\mu(m)-k_y^2\nu\right)+\kappa_\mu(m)\right).
\end{aligned}
\tag{6.12}
$$

From (4.63), we can combine the edge conditions into one large $(2\mathrm{M}+6)\times(\Lambda-1)$ by $4(\Lambda-1)$ matrix:

$$
\mathbf{E}=\begin{pmatrix}
\mathbf{E}^+_{R_1} & -\mathbf{E}^-_{T_2} & -\mathbf{E}^-_{R_2} & 0 & 0 & & 0 & 0 & 0\\
0 & \mathbf{E}^+_{T_2} & \mathbf{E}^+_{R_2} & -\mathbf{E}^-_{T_3} & -\mathbf{E}^-_{R_3} & & 0 & 0 & 0\\
 & & \vdots & & & \ddots & & & \\
0 & 0 & 0 & 0 & 0 & & \mathbf{E}^+_{T_{\Lambda-1}} & \mathbf{E}^+_{R_{\Lambda-1}} & -\mathbf{E}^-_{T_\Lambda}
\end{pmatrix},
\tag{6.13}
$$

and can solve the springed edge condition problem using the complete matrix (4.64).

6.2.3 Hinged Connections

A special case of springed connections is hinged connections. We can solve for the hinge case by redefining the springed edge conditions (3.20) by taking the limit as s_r approaches ∞ and taking $s_v = 0$ to give (3.21) (Xia et al., 2000). The MEEM for hinged plates is very similar to the method presented in 6.2.2. The edge conditions are again expressed by (6.9), (6.10), (6.9), where $\mathbf{E}^+_{T_\mu}$, $\mathbf{E}^+_{R_\mu}$, $\mathbf{E}^-_{T_\mu}$, $\mathbf{E}^-_{T_\mu}$ are in this case given by

$$
\begin{aligned}
\mathbf{E}^-_{T_\mu}(1,m) &= -k_\mu(m)\tan(k_\mu(m)h),\\
\mathbf{E}^-_{R_\mu}(1,m) &= -k_\mu(m)\tan(k_\mu(m)h)e^{\kappa_\mu(m)(l_\mu-r_\mu)},\\
\mathbf{E}^+_{T_\mu}(1,m) &= -k_\mu(m)\tan(k_\mu(m)h)e^{-\kappa_\mu(m)(r_\mu-l_\mu)},\\
\mathbf{E}^+_{R_\mu}(1,m) &= -k_\mu(m)\tan(k_\mu(m)h),\\
\\
\mathbf{E}^-_{T_\mu}(2,m) &= k_\mu(m)(\kappa^3_\mu(m)-\kappa_\mu(m)k^2_y(2-\nu))\tan(k_\mu(m)h),\\
\mathbf{E}^-_{R_\mu}(2,m) &= -k_\mu(m)(\kappa^3_\mu(m)-\kappa_\mu(m)k^2_y(2-\nu))\tan(k_\mu(m)h)e^{\kappa_\mu(m)(l_\mu-r_\mu)},\\
\mathbf{E}^+_{T_\mu}(2,m) &= k_\mu(m)(\kappa^3_\mu(m)-\kappa_\mu(m)k^2_y(2-\nu))\tan(k_\mu(m)h)e^{-\kappa_\mu(m)(r_\mu-l_\mu)},\\
\mathbf{E}^+_{R_\mu}(2,m) &= -k_\mu(m)(\kappa^3_\mu(m)-\kappa_\mu(m)k^2_y(2-\nu))\tan(k_\mu(m)h),\\
\\
\mathbf{E}^-_{T_\mu}(3,m) &= -k_\mu(m)(\kappa^2_\mu(m)-k^2_y\nu)\tan(k_\mu(m)h),\\
\mathbf{E}^-_{R_\mu}(3,m) &= -k_\mu(m)(\kappa^2_\mu(m)-k^2_y\nu)\tan(k_\mu(m)h)e^{\kappa_\mu(m)(l_\mu-r_\mu)},\\
\mathbf{E}^+_{T_\mu}(3,m) &= 0,\\
\mathbf{E}^+_{R_\mu}(3,m) &= 0,\\
\\
\mathbf{E}^-_{T_\mu}(4,m) &= 0,\\
\mathbf{E}^-_{R_\mu}(4,m) &= 0,\\
\mathbf{E}^+_{T_\mu}(4,m) &= -k_\mu(m)(\kappa^2_\mu(m)-k^2_y\nu)\tan(k_\mu(m)h)e^{-\kappa_\mu(m)(r_\mu-l_\mu)},\\
\mathbf{E}^+_{R_\mu}(4,m) &= -k_\mu(m)(\kappa^2_\mu(m)-k^2_y\nu)\tan(k_\mu(m)h).
\end{aligned}
\tag{6.14}
$$

The hinged problem is solved using the large edge matrix (6.13) and solving the complete matrix (4.64).

6.3 The Green Function Method

6.3.1 Simple Connections

We first consider clamped plates so that (3.14) and (3.15) apply, which imply $[\partial_x \eta]_m = 0$ and $[\eta]_m = 0$. η, defined by (5.21), therefore becomes

$$\eta = \eta^I + \beta \sum_{n=1}^{\Lambda-1} (\partial_x G_z [\partial_x^2 \eta]_n - G_z [\partial_x^3 \eta]_n), \tag{6.15}$$

so that edge condition (3.14) becomes

$$\begin{aligned} 0 = -\kappa(0) e^{-\kappa(0)x} + \beta \sum_{n=1}^{\Lambda-1} \sum_{m=-2}^{\infty} & (\kappa(m)[\partial_x^2 \eta]_n - \operatorname{sgn}(x - x')[\partial_x^3 \eta]_n) \\ & \frac{k(m)\kappa(m)\sin^2(k(m)h)}{2\alpha \mathcal{C}(k(m))} e^{-\kappa(m)|x-x'|}, \end{aligned} \tag{6.16}$$

and edge condition (3.15) becomes

$$\begin{aligned} 0 = e^{-\kappa(0)x} + \beta \sum_{n=1}^{\Lambda-1} \sum_{m=-2}^{\infty} & (-\operatorname{sgn}(x - x')\kappa(m)[\partial_x^2 \eta]_n + [\partial_x^3 \eta]_n) \\ & \frac{k(m)\sin^2(k(m)h)}{2\alpha \mathcal{C}(k(m))} e^{-\kappa(m)|x-x'|}. \end{aligned} \tag{6.17}$$

The reflection and transmission coefficients, R_1 and T_Λ can now be found by taking the limit of η as $x \to \pm\infty$ so that

$$R_1 = e^{\kappa(0) r_1} \left(\frac{\beta k(0) \sin^2(k(0)h)}{2\alpha \mathcal{C}(k(0))} \sum_{n=1}^{\Lambda-1} \big(\kappa(0)[\partial_x^2 \eta]_n + [\partial_x \eta]_n\big) \right), \tag{6.18}$$

and

$$T_\Lambda = e^{-\kappa(0) r_{\Lambda-1}} \left(1 - \frac{\beta k(0) \sin^2(k(0)h)}{2\alpha \mathcal{C}(k(0))} \sum_{n=1}^{\Lambda-1} \big(\kappa(0)[\partial_x^2 \eta]_n - [\partial_x \eta]_n\big) \right). \tag{6.19}$$

We also consider simply supported plates so that (3.16) and (3.17) apply, which imply $[\partial_x^2 \eta]_n = 0$ and $[\eta]_n = 0$. η, defined by (5.21), therefore becomes

$$\eta(x) = \eta^I - \beta \sum_{n=1}^{\Lambda-1} \left((\partial_x^2 - 2k_y^2) G_z [\partial_x \eta]_n + G_z [\partial_x^3 \eta]_m \right), \tag{6.20}$$

so that edge condition (3.16) becomes

$$0 = \kappa(0)^2 e^{-\kappa(0)x} + \beta \sum_{n=1}^{\Lambda-1} \sum_{m=-2}^{\infty} \big(\kappa(m)^2(\kappa(m)^2 - 2k_y^2)[\partial_x \eta]_n + \kappa(m)^2[\partial_x^3 \eta]_n\big) \frac{k(m)\sin^2(k(m)h)}{2\alpha \mathcal{C}(k(m))} e^{-\kappa(m)|x-x'|}, \tag{6.21}$$

and edge condition (3.17) becomes

$$0 = e^{-\kappa(0)x} + \beta \sum_{n=1}^{\Lambda-1} \sum_{m=-2}^{\infty} \big((\kappa(m)^2 - 2k_y^2)[\partial_x \eta]_n + [\partial_x^3 \eta]_n\big) \frac{k(m)\sin^2(k(m)h)}{2\alpha \mathcal{C}(k(m))} e^{-\kappa(m)|x-x'|}. \tag{6.22}$$

The reflection and transmission coefficients, R_1 and T_Λ can now be found by taking the limit of η as $x \to \pm\infty$ so that

$$R_1 \;= e^{\kappa(0)r_1} \left(\frac{\beta k(0)\sin^2(k(0)h)}{2\alpha \mathcal{C}(k(0))} \sum_{n=1}^{\Lambda-1} \big((\kappa(0)^2 - 2k_y^2)[\partial_x \eta]_n + [\partial_{x'}^3 \eta]_n\big) \right), \tag{6.23}$$

and

$$T_\Lambda \;= e^{-\kappa(0)r_{\Lambda-1}} \left(1 + \frac{\beta k(0)\sin^2(k(0)h)}{2\alpha \mathcal{C}(k(0))} \sum_{n=1}^{\Lambda-1} \big((\kappa(0)^2 - 2k_y^2)[\partial_x \eta]_n + [\partial_x^3 \eta]_n\big) \right). \tag{6.24}$$

Finally, we consider sliding plates so that (3.18) and (3.19) apply, which imply $[\partial_x^3 \eta]_n = 0$ and $[\partial_x \eta]_n = 0$. η, defined by (5.21), therefore becomes

$$\eta = \eta^I + \beta \sum_{n=1}^{\Lambda-1} \big((\partial_x^3 - 2k_y^2 \partial_x) G_z[\eta]_n + \partial_x G_z[\partial_x^2 \eta]_n\big), \tag{6.25}$$

so that edge condition (3.18) becomes

$$0 = -\kappa(0)^3 e^{-\kappa(0)x} + \beta \sum_{n=1}^{\Lambda-1} \sum_{m=-2}^{\infty} \big((\kappa(m)^3(\kappa(m)^3 - 2k_y^2\kappa(m))[\eta]_n + \kappa(m)^4[\partial_x^2 \eta]_n\big) \frac{k(m)\sin^2(k(m)h)}{2\alpha \mathcal{C}(k(m))} e^{-\kappa(m)|x-x'|}, \tag{6.26}$$

and edge condition (3.19) becomes

$$\begin{aligned} 0 = -\kappa(0)e^{-\kappa(0)x} + \beta\sum_{n}^{\Lambda-1}\sum_{m=-2}^{\infty}\big(\kappa(m)(\kappa(m)^3 - 2k_y^2\kappa(m))[\eta]_n \\ +\kappa(m)^2[\partial_x^2\eta]_n\big)\frac{k(m)\sin^2(k(m)h)}{2\alpha\mathcal{C}(k(m))}e^{-\kappa(m)|x-x'|}. \end{aligned} \tag{6.27}$$

The reflection and transmission coefficients, R_1 and T_Λ can now be found by taking the limit of η as $x \to \pm\infty$ so that

$$\begin{aligned} R_1 \;= e^{\kappa(0)r_1}\Bigg(&\frac{\beta k(0)\sin^2(k(0)h)}{2\alpha\mathcal{C}(k(0))} \\ &\sum_{n=1}^{\Lambda-1}\big((\kappa(0)^3 - 2k_y^2\kappa(0))[\eta]_n + \kappa(0)[\partial_x^2\eta]_n\big)\Bigg), \end{aligned} \tag{6.28}$$

and

$$\begin{aligned} T_\Lambda \;= e^{-\kappa(0)r_{\Lambda-1}}\Bigg(&1 - \frac{\beta k(0)\sin^2(k(0)h)}{2\alpha\mathcal{C}(k(0))} \\ &\sum_{n=1}^{\Lambda-1}\big((\kappa(0)^3 - 2k_y^2\kappa(0))[\eta]_n + \kappa(0)[\partial_x^2\eta]_n\big)\Bigg). \end{aligned} \tag{6.29}$$

6.3.2 Springed Connections

We begin by re-expressing (3.20) as

$$\begin{aligned} \beta(\partial_x^3 - k_y^2(2-\nu)\partial_x)\eta^+(x'_n) &= -s_v[\eta]_n, \\ \beta(\partial_x^3 - k_y^2(2-\nu)\partial_x)\eta^-(x'_n) &= -s_v[\eta]_n, \\ \beta(\partial_x^2 - k_y^2\nu)\eta^+(x'_n) &= s_r[\partial_{r_\mu}\eta]_n, \\ \beta(\partial_x^2 - k_y^2\nu)\eta^-(x'_n) &= s_r[\partial_{r_\mu}\eta]_n, \end{aligned} \tag{6.30}$$

where $\eta^+(x'_n)$ is the displacement at the right edge of the n^{th} crack and $\eta^-(x'_n)$ is the displacement at the left edge of the μ^{th} crack. (6.30) implies

$$(\partial_x^2 - k_y^2\nu)\eta^+(x'_n) = (\partial_x^2 - k_y^2\nu)\eta^-(x'_n), \tag{6.31}$$

which implies

$$[\partial_x^2\eta]_n = k_y^2\nu[\eta]_n. \tag{6.32}$$

(6.30) also implies

$$(\partial_x^3 - k_y^2(2-\nu)\partial_x)\eta^+(x'_n) = (\partial_x^3 - k_y^2(2-\nu)\partial_x)\eta^-(x'_n), \tag{6.33}$$

which implies

$$[\partial_x^3\eta]_n = k_y^2(2-\nu)[\partial_x\eta]_n. \tag{6.34}$$

η, as defined by (5.21), can now be re-expressed as

$$\eta = \eta^I + \beta\sum_{n=1}^{\Lambda-1}\big((\partial_x^3 - k_y^2(2-\nu)\partial_x)G_z[\eta]_n - (\partial_x^2 - k_y^2\nu)G_z[\partial_x\eta]_n\big). \tag{6.35}$$

We now have two unknowns which can be solved simultaneously using the following two edge conditions

$$\begin{aligned} -\frac{s_v}{\beta}[\eta]_n &= (\partial_x^3 - k_y^2(2-\nu)\partial_x)\eta(x'_n), \\ \frac{s_r}{\beta}[\partial_x\eta]_n &= (\partial_x^2 - k_y^2\nu)\eta(x'_n). \end{aligned} \tag{6.36}$$

Expanding the first edge condition in (6.36) gives

$$\begin{aligned} -\frac{s_v}{\beta}[\eta]_a = &\left(\partial_x^3 - k_y^2(2-\nu)\partial_x\right)\eta^I \\ &+ \left(\partial_x^3 - k_y^2(2-\nu)\partial_x\right)\sum_{n=1}^{\Lambda-1}\left(\partial_x^3 G_z - k_y^2(2-\nu)\partial_x G_z\right)[\eta]_n \\ &- \left(\partial_x^3 - k_y^2(2-\nu)\partial_x\right)\sum_{n=1}^{\Lambda-1}\left(\partial_x^2 G_z - k_y^2\nu G_z\right)[\partial_x\eta]_n, \end{aligned} \tag{6.37}$$

which gives

$$\begin{aligned} -\frac{s_v}{\beta}[\eta]_a = &-(\kappa(0)^3 - k_y^2\kappa(0)(2-\nu))e^{-\kappa(0)x} \\ &+ \left(\kappa(m)^3 - \kappa(m)k_y^2(2-\nu)\right)^2 \\ &\left(\sum_{n=1}^{\Lambda-1}\sum_{m=-2}^{\infty}\mathcal{C}(k(m))^{-1}k(m)\sin^2(k(m)h)e^{-\kappa(m)|x-x'|}\right)[\eta]_n \\ &-\mathrm{sgn}(x-x')(\kappa(m)^3 - \kappa(m)k_y^2(2-\nu))(\kappa(m)^2 - k_y^2\nu) \\ &\left(\sum_{n=1}^{\Lambda-1}\sum_{m=-2}^{\infty}\mathcal{C}(k(m))^{-1}k(m)\sin^2(k(m)h)e^{-\kappa(m)|x-x'|}\right)[\partial_x\eta]_n. \end{aligned} \tag{6.38}$$

Rearranging gives

$$
\begin{aligned}
&(\kappa(0)^3 - k_y^2\kappa(0)(2-\nu))e^{-\kappa(0)x} = \\
&\frac{s_v}{\beta}[\eta]_a + \left(\kappa(m)^3 - \kappa(m)k_y^2(2-\nu)\right)^2 \\
&\qquad \left(\sum_{n=1}^{\Lambda-1}\sum_{m=-2}^{\infty} \mathcal{C}(k(m))^{-1}k(m)\sin^2(k(m)h)e^{-\kappa(m)|x-x'|}\right)[\eta]_n \\
&-\mathrm{sgn}(x-x')(\kappa(m)^3 - \kappa(m)k_y^2(2-\nu))(\kappa(m)^2 - k_y^2\nu) \\
&\qquad \left(\sum_{n=1}^{\Lambda-1}\sum_{m=-2}^{\infty} \mathcal{C}(k(m))^{-1}k(m)\sin^2(k(m)h)e^{-\kappa(m)|x-x'|}\right)[\partial_x\eta]_n,
\end{aligned}
\tag{6.39}
$$

for $a = 1, 2, ..., \Lambda - 1$. Expanding the second edge condition in (6.36) gives

$$
\begin{aligned}
\frac{s_r}{\beta}[\partial_x\eta]_a = &\left(\partial_x^2 - k_y^2\nu\right)\eta^I \\
&+ \left(\partial_x^2 - k_y^2\nu\right)\sum_{n=1}^{\Lambda-1}\left(\partial_x^3 G_z - k_y^2(2-\nu)\partial_x G_z\right)[\eta]_n \\
&- \left(\partial_x^2 - k_y^2\nu\right)\sum_{n=1}^{\Lambda-1}\left(\partial_x^2 G_z - k_y^2\nu G_z\right)[\partial_x\eta]_n,
\end{aligned}
\tag{6.40}
$$

which gives

$$
\begin{aligned}
&\frac{s_r}{\beta}[\partial_x\eta]_a = (\kappa(0)^2 - k_y^2\nu)e^{-\kappa(0)x} \\
&-\mathrm{sgn}(x-x')\left(\kappa(m)^2 - k_y^2\nu\right)\left(\kappa(m)^3 - \kappa(m)k_u^2(2-\nu)\right)) \\
&\qquad \left(\sum_{n=1}^{\Lambda-1}\sum_{m=-2}^{\infty} \mathcal{C}(k(m))^{-1}k(m)\sin^2(k(m)h)e^{-\kappa(m)|x-x'|}\right)[\eta]_n \\
&+(\kappa(m)^2 - k_y^2\nu)^2 \\
&\qquad \left(\sum_{n=1}^{\Lambda-1}\sum_{m=-2}^{\infty} \mathcal{C}(k(m))^{-1}k(m)\sin^2(k(m)h)e^{-\kappa(m)|x-x'|}\right)[\partial_x\eta]_n.
\end{aligned}
\tag{6.41}
$$

Rearranging gives

$$
\begin{aligned}
&-(\kappa(0)^2 - k_y^2\nu)e^{-\kappa(0)x} = \\
&\quad -\mathrm{sgn}(x-x')\left(\kappa(m)^2 - k_y^2\nu\right)\left(\kappa(m)^3 - \kappa(m)k_y^2(2-\nu)\right) \\
&\qquad \left(\sum_{n=1}^{\Lambda-1}\sum_{m=-2}^{\infty}\mathcal{C}(k(m))^{-1}k(m)\sin^2(k(m)h)e^{-\kappa(m)|x-x'|}\right)[\eta]_n \\
&\quad -\frac{s_r}{\beta}[\partial_x\eta]_a + (\kappa(m)^2 - k_y^2\nu)^2 \\
&\qquad \left(\sum_{n=1}^{\Lambda-1}\sum_{m=-2}^{\infty}\mathcal{C}(k(m))^{-1}k(m)\sin^2(k(m)h)e^{-\kappa(m)|x-x'|}\right)[\partial_x\eta]_n,
\end{aligned}
\tag{6.42}
$$

for $a = 1, 2, ..., \Lambda - 1$.

The reflection and transmission coefficients, R_1 and T_Λ, can now be found by taking the limit of η as $x \to \pm\infty$. R_1 becomes

$$
\begin{aligned}
R_1 \quad &= e^{\kappa(0)r_1}\Bigg(\frac{\beta k(0)\sin^2(k(0)h)}{2\alpha\mathcal{C}(k(0))} \\
&\qquad \sum_{n=1}^{\Lambda-1}\Big((\kappa(0)^3 - \kappa(m)k_y^2(2-\nu))[\eta]_n + (\kappa(0)^2 - k_y^2\nu)[\partial_x\eta]_n\Big)\Bigg),
\end{aligned}
\tag{6.43}
$$

and T_Λ becomes

$$
\begin{aligned}
T_\Lambda \quad &= e^{\kappa(0)r_{\Lambda-1}}\Bigg(1 - \frac{\beta k(0)\sin^2(k(0)h)}{2\alpha\mathcal{C}(k(0))} \\
&\qquad \sum_{n=1}^{\Lambda-1}\Big((\kappa(0)^3 - \kappa(m)k_y^2(2-\nu))[\eta]_n - (\kappa(0)^2 - k_y^2\nu)[\partial_x\eta]_n\Big)\Bigg).
\end{aligned}
\tag{6.44}
$$

6.3.3 Hinged Connections

The hinged edge conditions (3.21) imply $[\eta]_n = 0$, $[\partial_x^2\eta]_n = 0$ and $[\partial_x^3\eta]_n = 0$ so that

$$\eta(x) = \eta^I + \beta \sum_{n=1}^{\Lambda-1} -(\partial_x^2 - 2k_y^2) G_z [\partial_x \eta]_n, \tag{6.45}$$

with only one unknown to solve. The hinged edge condition $\partial_x \eta(x'_n) = 0$ implies

$$\begin{aligned} [\partial_x \eta]_n &= \frac{\partial_x^2 \eta^{\mathrm{I}}}{\beta \partial_x^2 (\partial_x^2 - 2k_y^2) G_z(x)} \\ &= \kappa(0)^2 e^{-\kappa(0)x} \big(-\beta(\kappa(m)^2(\kappa(m)^2 - 2k_y^2) \\ &\qquad \mathcal{C}(k(m))^{-1} k(m) \sin^2(k(m)h) e^{-\kappa(m)|x-x'|} \big)^{-1}. \end{aligned} \tag{6.46}$$

The reflection and transmission coefficients, R_1 and T_Λ can now be found by taking the limit of η as $x \to \pm\infty$ so that

$$R_1 = e^{k(0)r_1} \left(\frac{\beta k(0) \sin^2(k(0)h)}{2\alpha \mathcal{C}(k(0))} \sum_{n=1}^{\Lambda-1} (k(0)^2 - 2k_y^2) e^{-k(0)x'_m} [\partial_x \eta]_n \right), \tag{6.47}$$

and

$$T_\Lambda = e^{-k(0)r_{\Lambda-1}} \left(1 - \frac{\beta k(0) \sin^2(k(0)h)}{2\alpha \mathcal{C}(k(0))} \sum_{n=1}^{\Lambda-1} (k(0)^2 - 2k_y^2) e^{-k(0)x'_n} [\partial_x \eta]_n \right). \tag{6.48}$$

7

Accuracy and Efficiency of Solutions

7.1 Introduction

We test our results by ensuring the system is in energy balance. We can also verify the MEEM by comparing it against the GFM and Meylan and Squire (1994)'s finite-floe model. We verify that each method is producing the same reflected energy at the first plate and the same transmitted energy at the final plate. We also compare the convergence of the methods.

7.2 Energy Balance

Based on the method used in Evans and Davies (1968), a check can be made to ensure the system is in energy balance. This is simply a condition that the incident energy is equal to the sum of the radiated energy. If the properties of the first and last semi-infinite plates were identical, this would give the familiar requirement that

$$|T_\Lambda(0)|^2 + |R_1(0)|^2 = |I|^2.$$

However, when the first and last plates have different properties, the energy balance equation becomes

$$\mathcal{D}|T_\Lambda(0)|^2 + |R_1(0)|^2 = 1, \tag{7.1}$$

where D is given by

$$\mathcal{D} = \left(\frac{\kappa_\Lambda^I k_1^I \cosh^2(k_1^I h)}{\kappa_1^I k_\Lambda^I \cosh^2(k_\Lambda^I h)}\right) \left(\frac{\frac{\beta_\Lambda}{\alpha} 4(k_\Lambda^I)^3((\kappa_\Lambda^I)^2 + k_y^2)\sinh^2(k_\Lambda^I h) + \frac{1}{2}\sinh(2k_\Lambda^I h) + k_\Lambda^I h}{\frac{\beta_1}{\alpha} 4(k_1^I)^3((\kappa_1^I)^2 + k_y^2)\sinh^2(k_1^I h) + \frac{1}{2}\sinh(2k_1^I h) + k_1^I h}\right) \tag{7.2}$$

where $k_\mu^I = -\Im k_\mu(0)$ and $\kappa_\mu^I = -\Im\kappa_\mu(0)$. D is found by applying Green's theorem to ϕ and its conjugate (Evans and Davies, 1968). The derivation of $\mathcal{D}$ is provided in Appendix A. The energy balance condition is useful to help check that the solution is not incorrect (it does not of course guarantee the solution is correct). The energy balance condition is surprisingly well satisfied by our solutions. With $M = 20$, $\beta = 0.1$, $h = 1$, $\gamma = 0$ and $\alpha = 5$, we can easily get (7.1) correct to ten decimal places.

7.3 Verifying the Matched Eigenfunction Expansion Methods Reflection and Transmission Coefficients

We compare results from the MEEM (Section 4) with results from the GFM (Section 5). The problem which can be solved by the GFM is equivalent to the MEEM problem if the rigidity properties are identical for each elastic plate. We have selected the GFM to compare with because it solves the problem in a very different way. Also, the GFM can be applied to multiple plates which is the most challenging aspect of our problem. To further verify the MEEM, we also compare its solutions with solutions from Meylan and Squire (1994)'s finite-floe model.

Figure 7.1 shows a comparison between the MEEM and the GFM for the free edge case, Figure 7.2 compares the two methods for the various basic edge conditions and Figure 7.3 compares the two methods for plates connected by springs. Figure 7.4 compares the MEEM and Meylan and Squire (1994)'s finite-floe model. The crosses and circles are the results using the MEEM and the solid lines are due to the GFM and finite-floe model. As can be seen from the figures, there is perfect agreement between each of the methods.

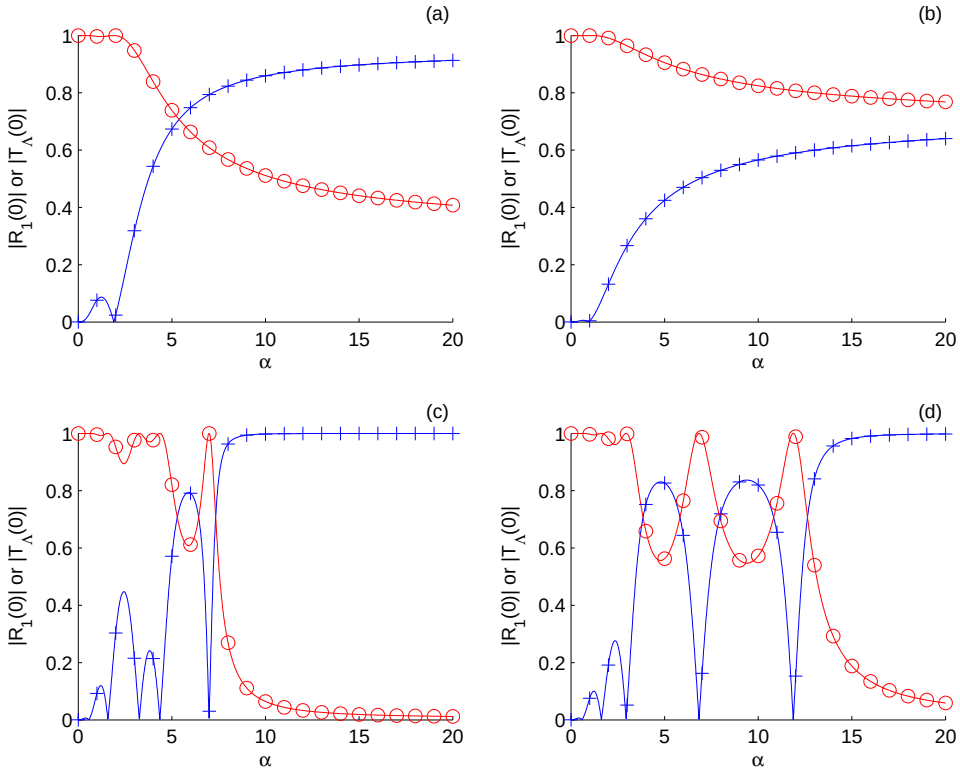

Figure 7.1: The MEEM (-) and the GFM ('+' and 'o') solutions for the reflected (crosses) and transmitted (circles) coefficients against α for plates with free edges. $\beta = 0.1$, $\gamma = 0$ and $h = 1$. Figure (a) presents solutions for two plates with the crack at $x = 0$ and with $\theta = 0$. Figure (b) presents solutions for two plates with the crack at $x = 0$ and with $\theta = \frac{\pi}{3}$. Figure (c) presents solutions for four plates with the cracks at $x = 0, 1, 2$ and with $\theta = 0$. Figure (d) presents solutions for four plates with the cracks at $x = 0, 1, 2$ and with $\theta = \frac{\pi}{12}$.

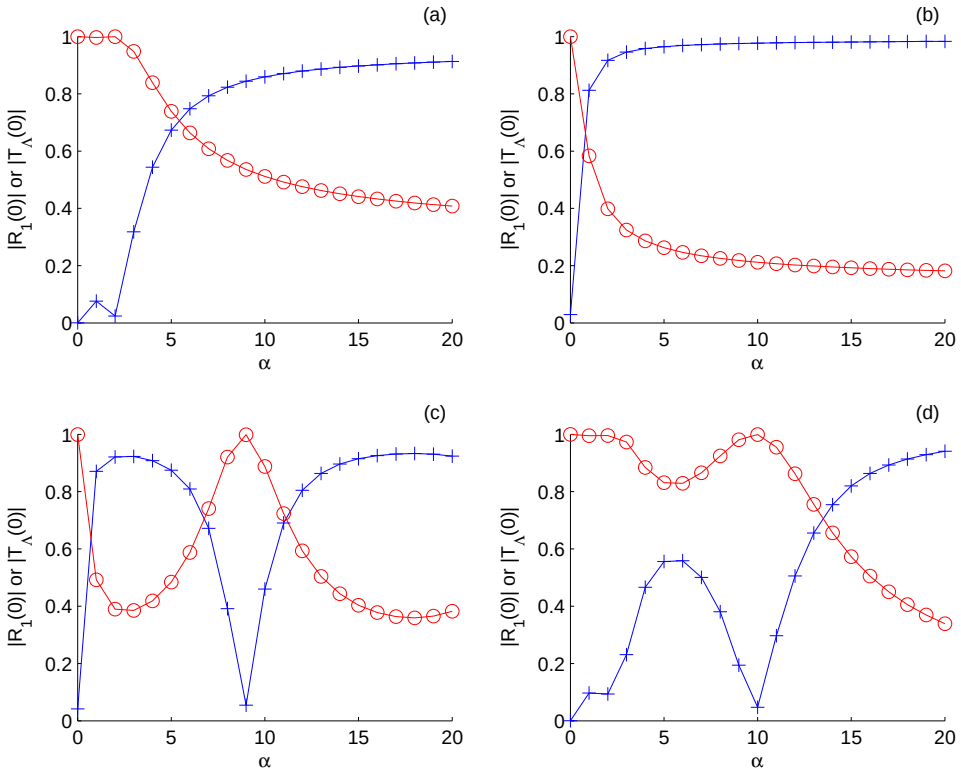

Figure 7.2: The MEEM (-) and the GFM ('+' and 'o') solutions for the reflected (crosses) and transmitted (circles) coefficients against α for a set of plates with various basic edge conditions with $\beta = 0.1$, $\gamma = 0$ and $h = 1$. Figure (a) gives solutions for free plates for 2 plates with $\theta = 0$. Figure (b) gives solutions for clamped plates for 4 plates with $\theta = \frac{\pi}{6}$. Figure (c) gives solutions for simply supported plates for 2 plates with $\theta = 0$. Figure (d) gives solutions for sliding plates for 4 plates with $\theta = \frac{\pi}{3}$.

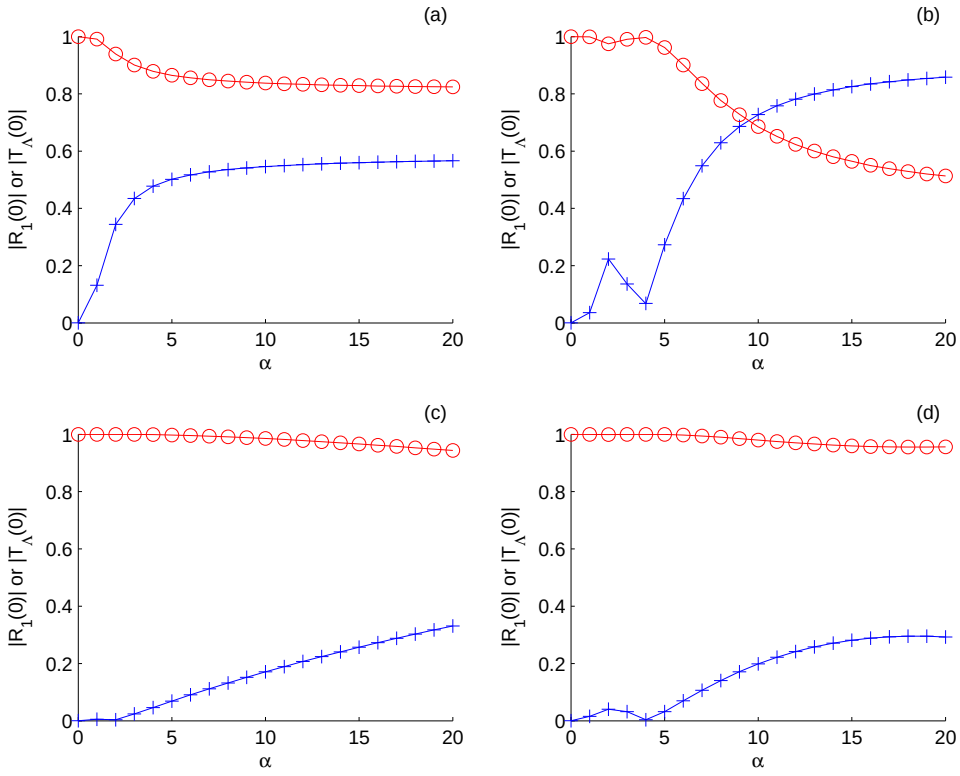

Figure 7.3: The MEEM (-) and the GFM ('+' and 'o') solutions for the reflected (crosses) and transmitted (circles) coefficients against α for a set of plates connected by springs with $\beta = 0.1$, $\gamma = 0$ and $h = 1$. Figure (a) gives solutions for the hinged plates i.e. with $s_v \to \infty$ and $s_r = 0$ for 2 plates with $\theta = 0$. Figure (b) gives solutions for the hinged plates i.e. with $s_v \to \infty$ and $s_r = 0$ for 4 plates with $\theta = \frac{\pi}{6}$. Figure (c) gives solutions for $s_v = 1$ and $s_r = 0.5$ for 2 plates with $\theta = 0$. Figure (d) gives solutions for $s_v = 1$ and $s_r = 1000$ for 4 plates with $\theta = \frac{\pi}{3}$.

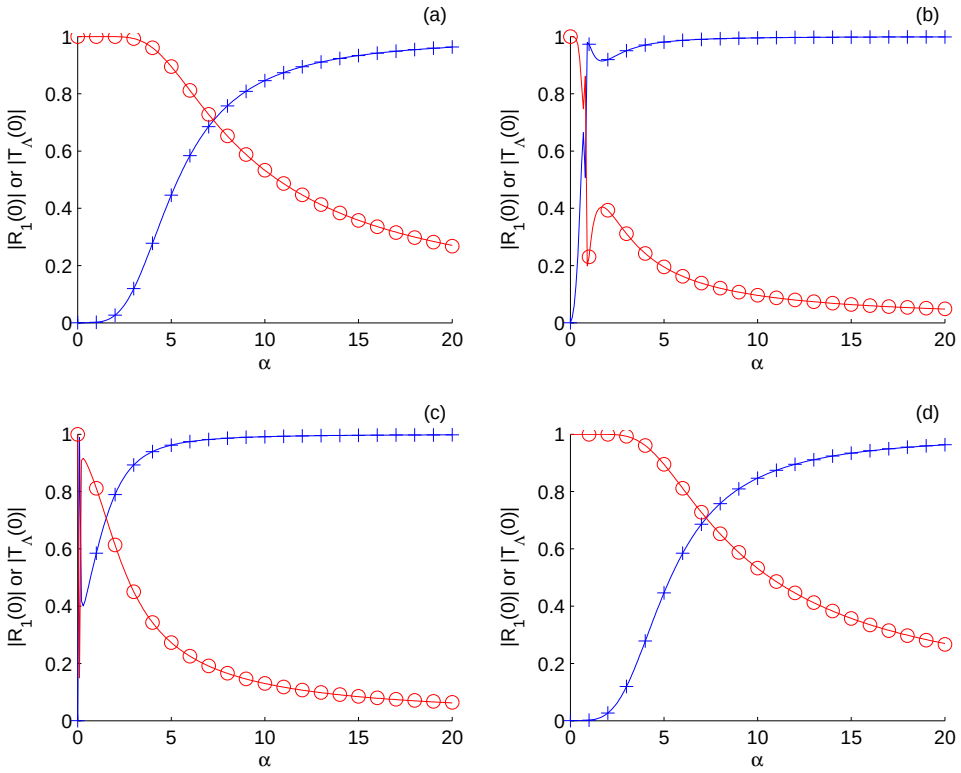

Figure 7.4: The MEEM (-) and Meylan and Squire (1994)'s finite-floe's ('+' and 'o') reflected (crosses) and transmitted (circles) coefficients against α for free edges with $\theta = 0$ and $h = 1$. Figure (a) gives solutions for $\beta = 1$ and $\gamma = 0$. Figure (b) gives solutions for $\beta = 1$ and $\gamma = 1$. Figure (a) gives solutions for $\beta = 50$ and $\gamma = 10$. Figure (a) gives solutions for $\beta = 1,000,000$ and $\gamma = 0$.

7.4 Solution Convergence

In this section, we compare the convergence of the MEEM and the GFM (Table 7.1). We also compare the convergence of the MEEM with the convergence of Meylan and Squire (1994) (Table 7.2). The rate of convergence of each of the solutions is almost identical. The accuracy of two decimal places for $M = 20$ is sufficient for most practical calculations.

Table 7.1: Solutions of $|T|$ from the MEEM (mT_m) and the GFM (T_g) for $\alpha = 5$, $\beta = 0.1$, $\gamma = 0$, $h = 1$.

Λ	M	$\lvert T_m\rvert$	$\lvert T_g\rvert$
2	5	0.72897005265395	0.68013661602795
	10	0.73710075717437	0.73382189306476
	20	0.73943613533854	0.73910099180859
	50	0.74014223492682	0.74012279625910
	100	0.74024743508561	0.74024507931561
	150	0.74026720286310	0.74026651629366
4	5	0.78572228609681	0.64049634405062
	10	0.81444198211422	0.80423931535963
	20	0.82228249776276	0.82126508433661
	50	0.82458694969417	0.82452862088603
	100	0.82492540871298	0.82491836384358
	150	0.82498871994750	0.82498666973497

Table 7.2: Solutions of $|T|$ from the MEEM (T_m) and Meylan and Squire (1994)'s finite-floe model (T_f) for $\alpha = 5$, $\beta = 0.1$, $\gamma = 0$, $h = 1$ and $L = 1$.

Λ	M	$\lvert T_m\rvert$	$\lvert T_f\rvert$
3	5	0.89505673189974	0.89853323035868
	10	0.89667581012319	0.89696873933913
	20	0.89673974324719	0.89675495407642
	50	0.89668355648691	0.89671200121147
	100	0.89666885086657	0.89670637318048
	150	0.89666569737692	0.89670531782835

8

Modelling an Idealised Marginal Ice Zone

8.1 Introduction

The sea-ice which forms in the polar oceans plays an important role in the world's climatic system, and it is important to understand the factors influencing its extent (see Section 2.1 for details). One of these factors is ocean wave energy, which plays a major role in the fracturing of sea-ice (Squire et al., 1995; Wadhams, 2000). To fully understand this fracturing process, it is critical to understand the attenuation of wave energy as it passes through the Marginal Ice Zone (MIZ). The MIZ forms at the boundary of open and frozen oceans and consists of vast fields of ice floes, which dampen wave energy and protect the continuous ice from wave action and consequent breakup. If the wind is blowing towards the ice edge from the open sea, the MIZ is compressed and produces a compact ice field (Wadhams, 2000). This type of ice field is thought to be most accurately modelled by a viscous model (Section 2.2.3). If the wind is blowing away from the ice edge, most of MIZ becomes diffuse. The outermost edge can sometimes organise itself into a series of compact ice-edge bands, which are separated by completely open water and lie with their long axes roughly perpendicular to the wind (Wadhams, 2000). It is expected that this

type of ice field is most accurately modelled by a scatter model (Section 2.2.3).

In this chapter, we use the solutions from the MEEM to simulate a diffuse MIZ. The development of this research and the results have been published in Kohout and Meylan (2006, 2008b). We begin by setting each of the variables so that they approximate a MIZ. An important quantity introduced here is E, the energy transmitted through the floes. Section 8.3 removes the resonance effects caused by linear wave theory, by averaging over many simulations. This enables us to estimate E for a given length, period, thickness and number of plates. It is then discovered that E attenuates exponentially so that an attenuation coefficient can be estimated for a given period and thickness. We finalise this chapter by considering the floe strain induced by wave action. The intention here is to predict the number of floes which will be broken due to wave action for a given wave period and floe thickness.

8.2 Setting the Variables

The number of evanescent modes required depends on the water depth. We set the water depth sufficiently large so that it can be considered infinite (in practice this depth is one wavelength i.e. $h = g\mathcal{T}^2/(2\pi)$) where $\mathcal{T}$ is the wave period. We set $M = 20$ as we find this gives a good compromise between accuracy and computational time. It is worth noting that the long period waves, for which it is more difficult to determine the attenuation coefficients, require less modes to get good convergence. We choose the following values for the constants: $Y = 6$ GPa, $\nu = 0.3$, $g = 9.8\ \mathrm{m\,s^{-2}}$, $\rho_w = 1025.0\ \mathrm{kg\,m^{-3}}$ and $\rho_\mu = 922.5\ \mathrm{kg\,m^{-3}}$ (Meylan, 2002). It is important to recognise that, because we have assumed the ice floes as thin, the non-dimensional stiffness β_μ is much more significant than the non-dimensional mass γ_μ. This means that the effect of changing the Young's modulus is equivalent to changing the cube root of the thickness. For this reason we will not consider any other values for Y. In all results, the semi-infinite plate on the left is open water. The semi-infinite plate on the right is a semi-infinite ice floe which is chosen to have the same thickness as the other floes (if the floe thicknesses are chosen randomly, then the thickness of the semi-infinite floe is also random). A wave is incident from the left-hand (open water side) with unit amplitude. The transmitted energy in the right-hand semi-infinite plate can be calculated as $E = 1 - |R_1|^2$ (this expression being a result of the condition that the incident energy is equal to the sum of the radiated energy). To simulate a MIZ with discrete floes, we have included gaps of water between each floe, and the thickness τ of each floe is chosen normally about a mean with a standard deviation of 0.05. In our

simulation, we have a number of variables; the incident period, $\mathcal{T}$; the length of each floe, L (which can differ per floe); the thickness of each floe, τ (which can differ per floe); and the number of floes, Λ. Note that the number of finite floes is $\Lambda - 2$ and every second floe represents a free surface.

8.3 Floe Length

One of the critical features of the model, and all models which use linear wave theory, is that it is fully coherent. This means that we will always observe effects of cancellation and addition of waves, no matter how large the ice floe size or number of ice floes. This can be seen in Figure 8.1, where the transmitted energy in the right-hand semi-infinite region, E, is shown as a function of floe length for $\Lambda = 7$. Note that in this case, each of the five finite floes are of identical length.

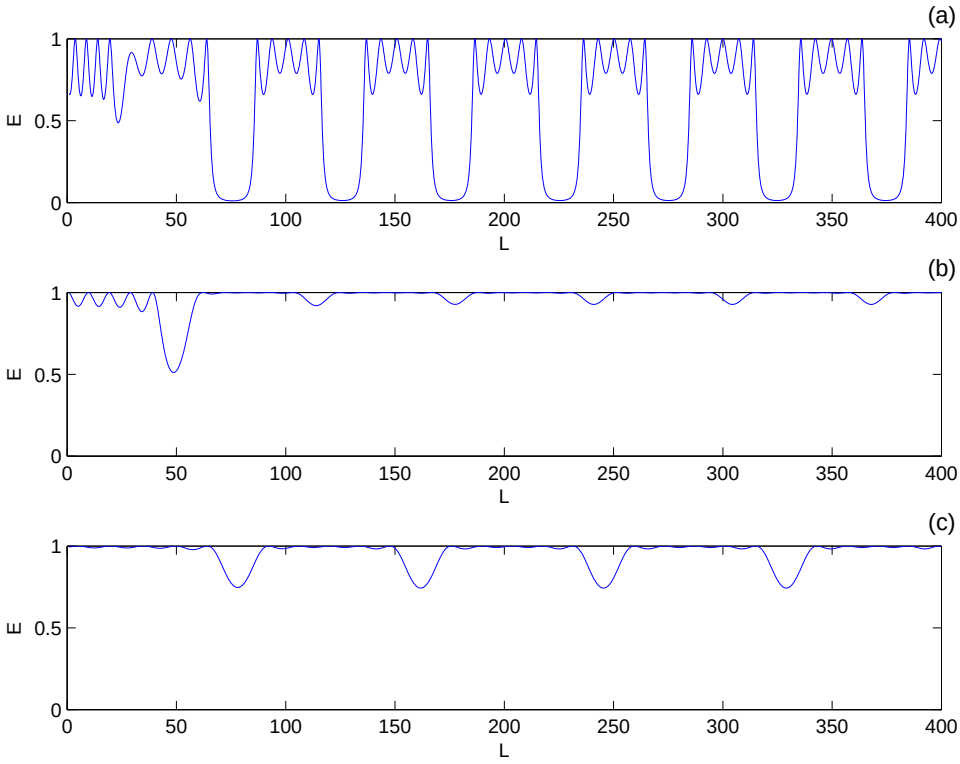

Figure 8.1: The transmitted energy (E) as a function of floe length L where τ is chosen normally about 1m with a standard deviation of 0.05 and $\Lambda = 7$ where the five finite floes are of identical length. Figure (a) is for $\mathcal{T} = 6$ s, Figure (b) is for $\mathcal{T} = 8$ s and Figure (c) is for $\mathcal{T} = 10$ s.

To remove this resonance, we allow the floe length to vary for each floe about a fixed mean and average over many trials. Similar methods have been considered in Wadhams

(1986) and Williams and Squire (2004, 2006). We assume that the spread of floe lengths in the MIZ fits a Rayleigh distribution. The Rayleigh distribution is given by

$$f(l) = \frac{l}{\zeta^2} e^{\frac{-l^2}{2\zeta^2}},$$

where $f(l)$ is the probability of selecting a floe length, l and $\zeta = \bar{\mu}\sqrt{\frac{\pi}{2}}$ where $\bar{\mu}$ is the mean floe length (Papoulis, 1984). The probability that the selected floe length is less than or equal to the actual floe length, l', is given by

$$p = \Pr(l \leq l') = \int_0^l f(l')dl'. \tag{8.1}$$

Finding the inverse and rearranging (8.1) gives,

$$l = \sqrt{-2\zeta^2 \ln(1-p)}. \tag{8.2}$$

Using (8.2), we randomly select p between 0 and 1 to find the Rayleigh distributed set of floe lengths about a given mean. We include gaps between each floe, where each gap length is also determined via the Rayleigh distribution. We calculate the mean E from 100 simulations (Figures 8.2, 8.3 and 8.4). The standard deviation of these simulations is tested for various periods and floe thickness and found to average 0.13. We test our results against other distributions (Figure 8.5) and we find virtually identical results.

The first result from our simulations is that the mean E is independent of length, provided the floe length is above a critical value. This is shown in Figures 8.2, 8.3 and 8.4 where we consider the effect of the parameters $\mathcal{T}$, τ and Λ. The physical explanation for this effect is as follows. If the floe is sufficiently long, it must bend in response to the waves. This bending induces reflections at the edges, but allows the waves to propagate under the floes without attenuation (since our ice floe is modelled as perfectly elastic). This means that the attenuation can be expected to depend only on the number of interfaces, with obvious analogy to other wave scattering processes. However, once the floe length becomes sufficiently short, so that the floe is no longer required to bend, there is no longer any notion of a wave propagating *under* the floe. Furthermore, as the floe shortens it will reflect less energy. In such situations, the floe no longer responds elastically, and a different physical model is appropriate. For this reason we will restrict our model so that in all the results we present, E is considered independent of floe length (and we always choose values of floe length to make this true for our simulations). It can be expected that this critical length will occur roughly when the wavelength is more than two or three times

the floe length.

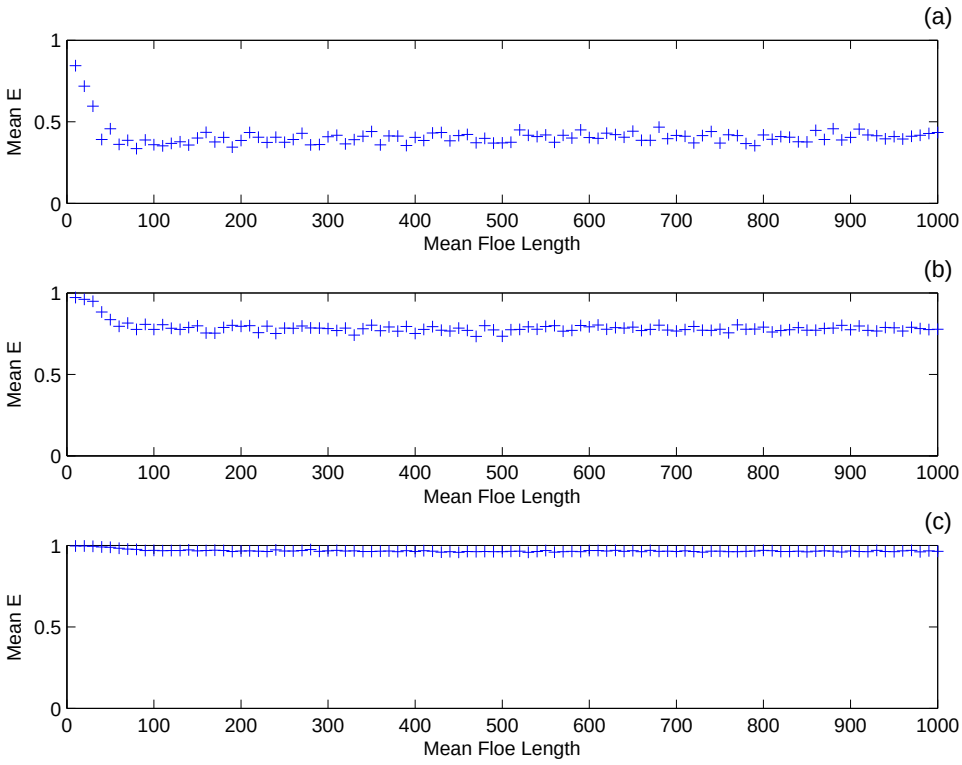

Figure 8.2: The mean transmitted energy (E) as a function of mean floe length, where the floe lengths are chosen via a Rayleigh distribution about the mean. For each mean floe length, E is averaged over 100 simulations. For each subplot τ is normally distributed, with a standard deviation of 0.05, about a mean of 1 m, $\Lambda = 10$. $\mathcal{T} = 6$ s in Figure (a), $\mathcal{T} = 8$ s in Figure (b) and $\mathcal{T} = 10$ s in Figure (c).

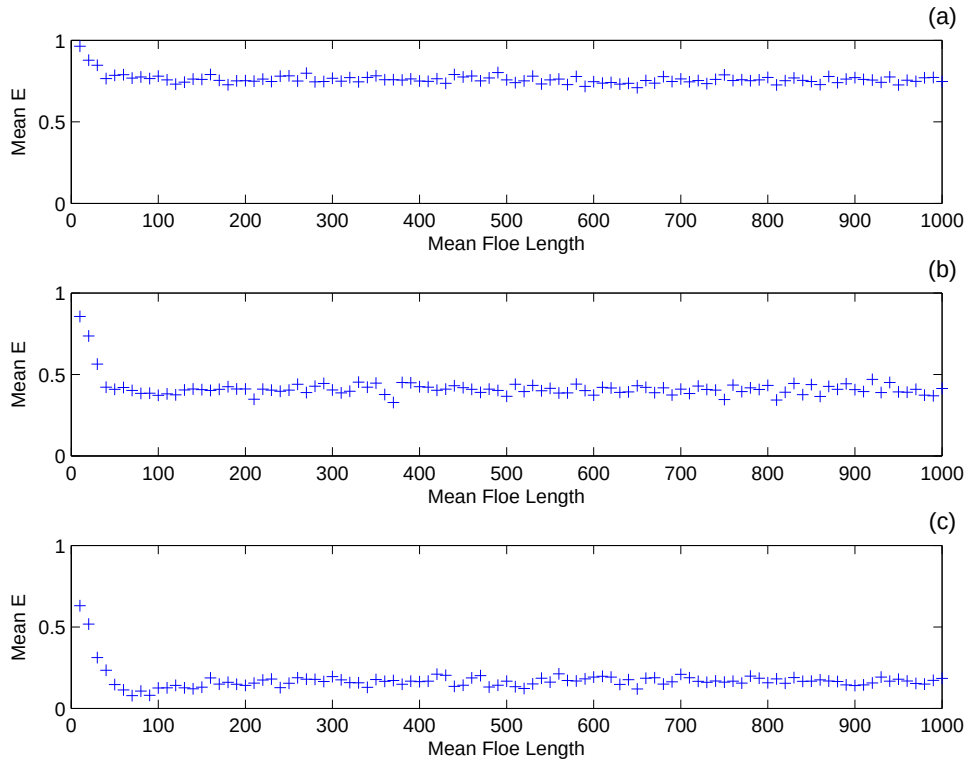

Figure 8.3: The mean transmitted energy (E) as a function of mean floe length, where the floe lengths are chosen via a Rayleigh distribution about the mean. For each mean floe length, E is averaged over 100 simulations. For each subplot $\Lambda = 10$, $\mathcal{T} = 6$ and τ is normally distributed, with a standard deviation of 0.05, about a mean. The mean $\tau = 0.5$ m in Figure (a), 1 m in Figure (b) and 2 m in Figure (c).

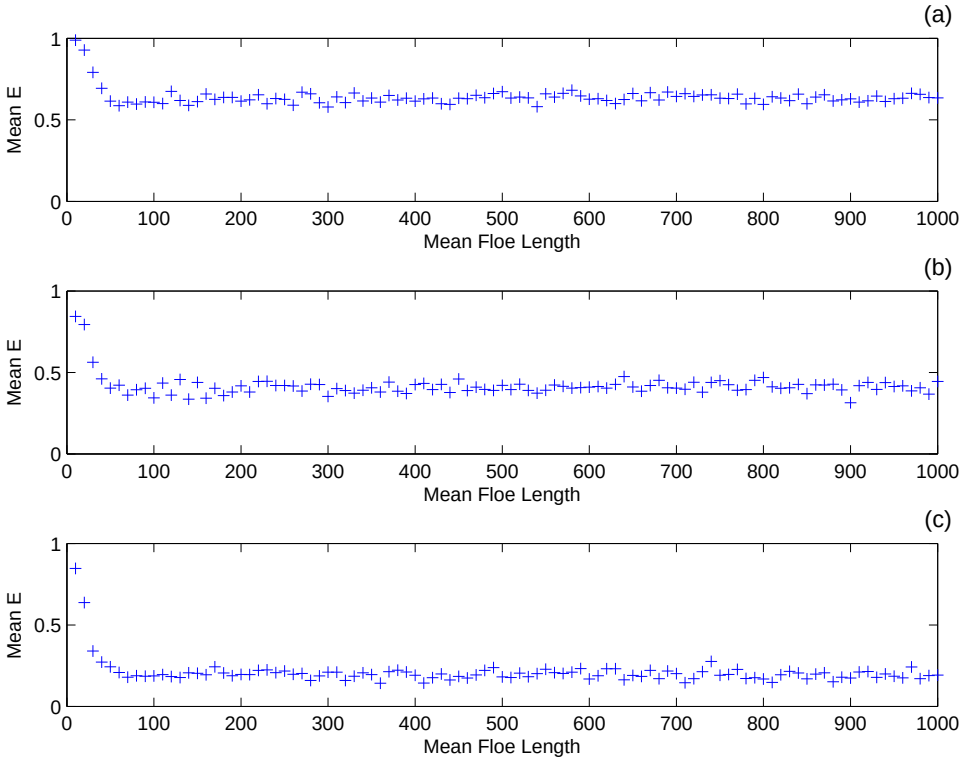

Figure 8.4: The mean transmitted energy (E) as a function of mean floe length, where the floe lengths are chosen via a Rayleigh distribution about the mean. For each mean floe length, E is averaged over 100 simulations. For each subplot τ is normally distributed, with a standard deviation of 0.05, about a mean of 1m, $\mathcal{T} = 6$. $\Lambda = 5$ in Figure (a), $\Lambda = 10$ in Figure (b) and $\Lambda = 20$ in Figure (c).

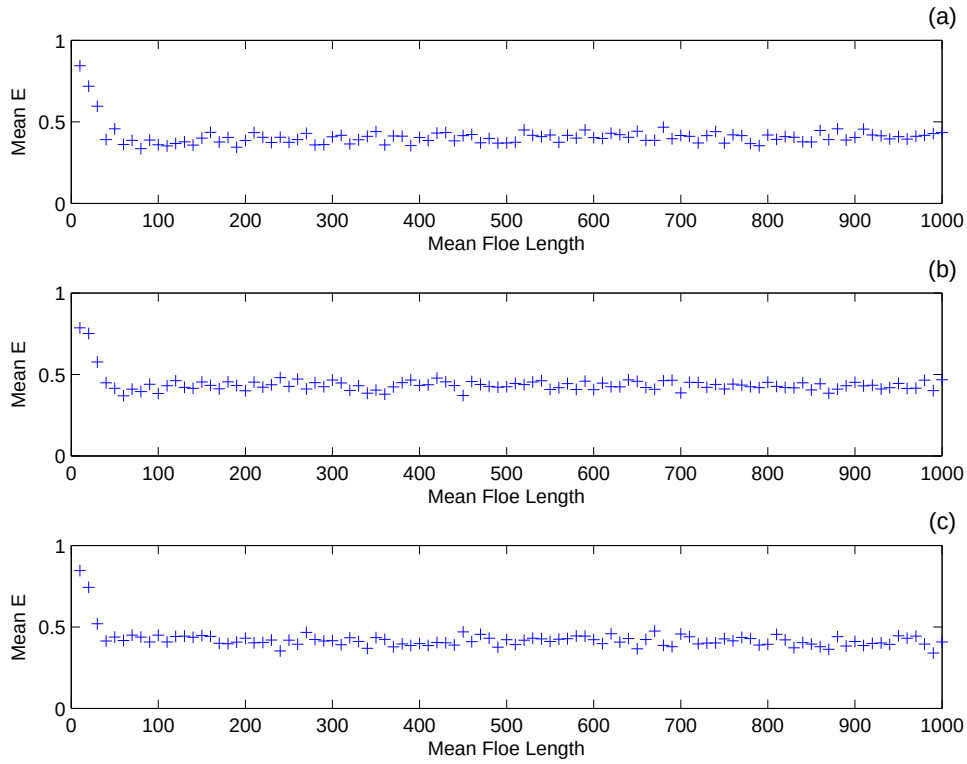

Figure 8.5: Mean transmitted energy (E) as a function of mean floe length, where the floe lengths are chosen via a Rayleigh distribution (Figure (a)), a Normal distribution (Figure (b)) and a Uniform distribution (Figure (c)). For each mean floe length, E is averaged over 100 simulations. τ is normally distributed, with a standard deviation of 0.05, about a mean of 1m, $\Lambda = 10$ and $\mathcal{T} = 6$.

Figure 8.6 shows the displacement for one of the simulations from each subplot of Figure 8.2. It is interesting to have some visualisation of the solution which is provided by the model for each simulation. It can be seen that the model provides much more information than just E since it provides the displacement of each ice floe. This suggests that the model could be used to predict other effects such as floe breakup.

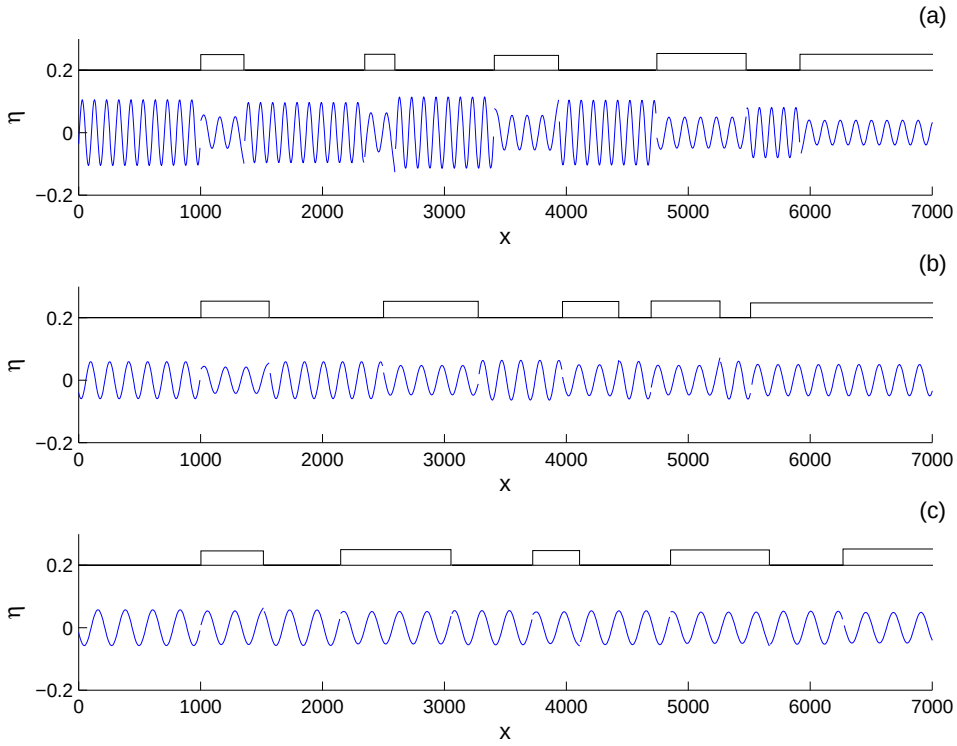

Figure 8.6: The displacement (η) as a function of distance (x) showing the displacement and floe geometry for three of the realisations used in Figure 8.2. $\mathcal{T} = 6$ s in Figure (a), $\mathcal{T} = 8$ s in Figure (b) and $\mathcal{T} = 10$ s in Figure (c). The boxed rectangles represent each plate.

8.4 Period and Floe Thickness

Figure 8.7 clearly shows that as period ($\mathcal{T}$) increases, energy (E) increases. This is as we would expect as increasing $\mathcal{T}$ reduces the bend in the floes, reducing reflection and energy loss. Figure 8.8 shows that as the mean τ increases, E decreases. We would also expect this result as more energy is required to bend thicker floes.

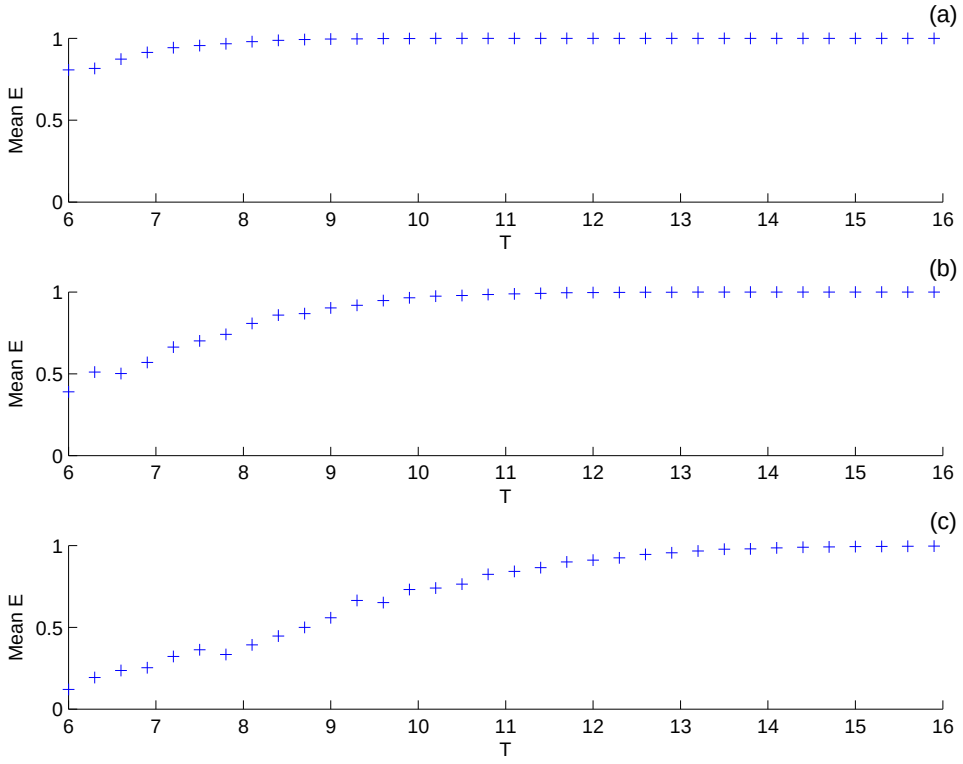

Figure 8.7: The mean transmitted energy (E) as a function of period ($\mathcal{T}$). For each $\mathcal{T}$, E is averaged over 100 simulations. For each subplot $\Lambda = 10$ and τ is normally distributed, with a standard deviation of 0.05, about a mean. The mean $\tau = 0.5$ m in Figure (a), 1 m in Figure (b) and 2 m in Figure (c).

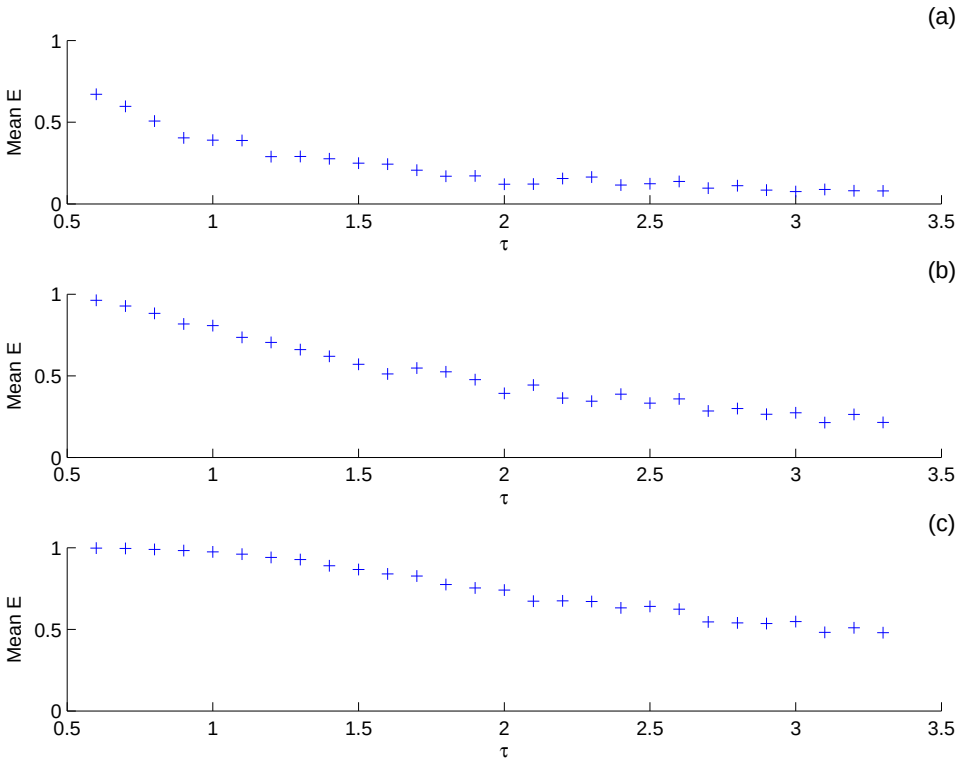

Figure 8.8: The mean transmitted energy (E) as a function of mean floe thickness (τ), where τ is normally distributed about the mean with a standard deviation of 0.05. For each τ, E is averaged over 100 simulations and $\Lambda = 10$. $\mathcal{T} = 6$ s in Figure (a), $\mathcal{T} = 8$ s in Figure (b) and $\mathcal{T} = 10$ s in Figure (c).

8.5 Number of Floes

Here we investigate the effects of increasing Λ. Figures 8.9 and 8.10 show the least square fit of $\ln(E)$ to a straight line, indicating that E is decreasing exponentially with increasing Λ. The linear correlation coefficients of the fit are consistently high and above 90%. The strong correlation indicates that our model is successfully predicting the measured exponential decay of energy (note that we have not made this assumption in our formulation and this is a prediction of the model). The fit to an exponential tends to reduce as Λ increases. This may be a consequence of increased reflection which can increase coherent effects and lead to increased scatter. We conclude that we can fit the data to an exponential curve of the form $e^{-a\Lambda}$, where a is the attenuation coefficient (note that as Λ approaches 0, E approaches 1). We express the exponential curve as a linear function by taking the natural logarithm of both sides i.e. $\ln E = -a\Lambda$. We solve for a by minimising the sum of squares of errors between the data and the approximated curve. We will now concentrate on a, the (exponential) attenuation coefficient.

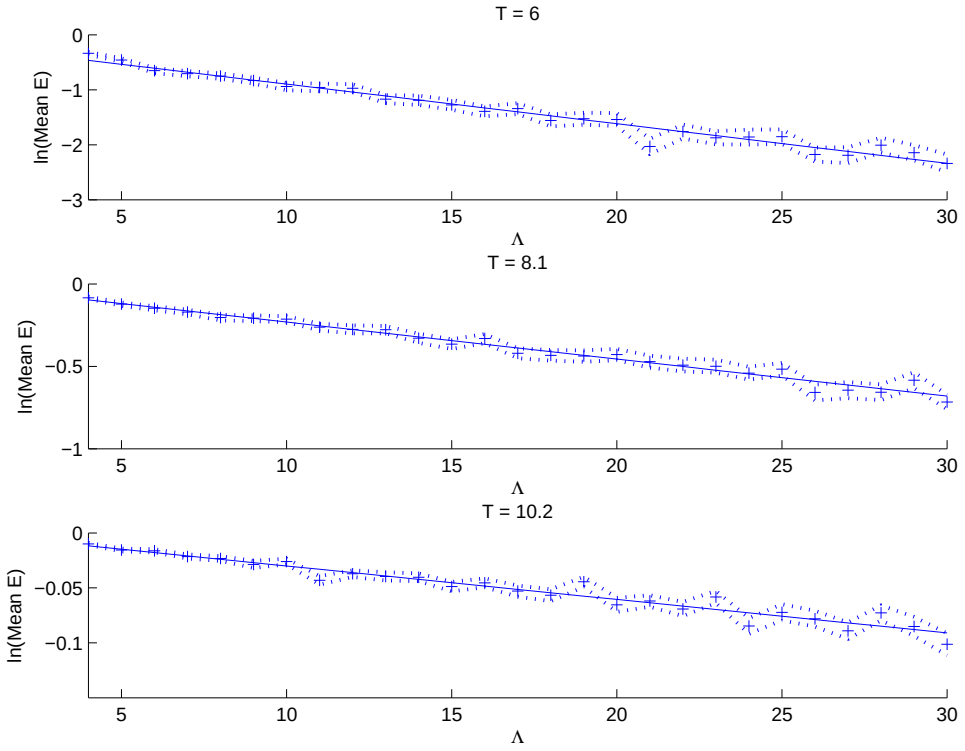

Figure 8.9: $\ln(E)$ as a function of Λ. For each Λ, E is averaged over 100 trials. The dotted line gives the 67% confidence interval for E. τ is normally distributed, with a standard deviation of 0.05, about a mean of 1m. $\mathcal{T} = 6$ s in Figure (a), $\mathcal{T} = 8$ s in Figure (b), and $\mathcal{T} = 10$ s in Figure (c). The solid line shows a straight line fit to the data points ('+').

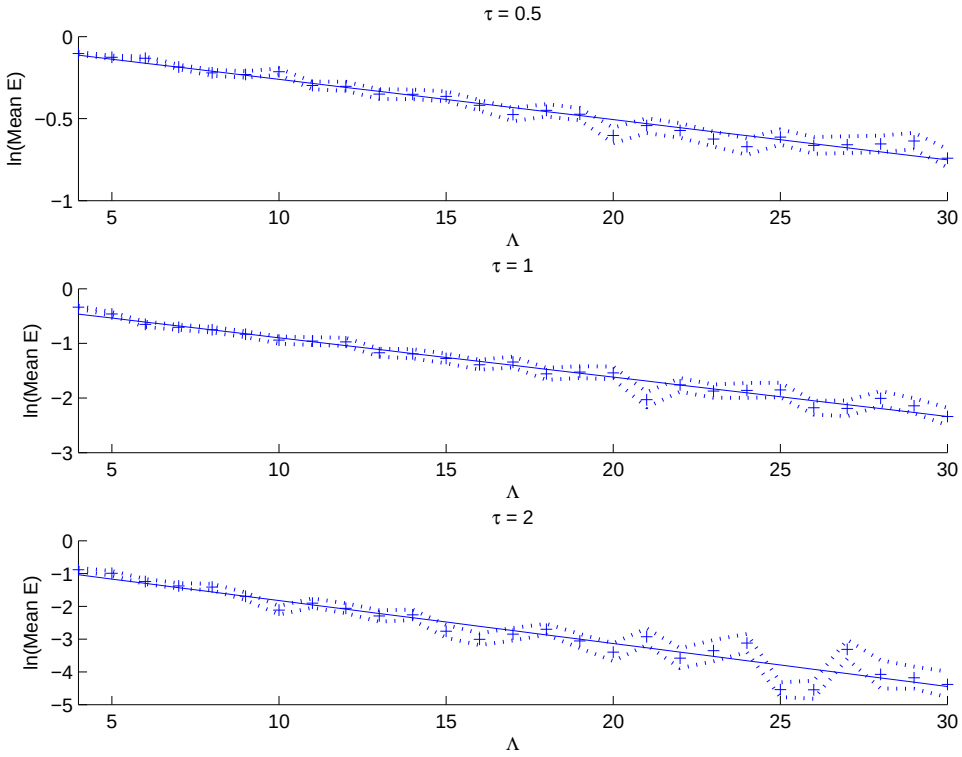

Figure 8.10: The logarithm of the mean transmitted energy ($\ln(E)$) as a function of the number of floes (Λ). For each Λ, E is averaged over 100 trials and the dotted line gives the 67% confidence interval for E (one standard deviation). $\mathcal{T} = 6$ and τ is normally distributed, with a standard deviation of 0.05, about a mean. In Figure (a), the mean $\tau = 0.5$ m and the linear correlation coefficient (r^2) is 0.96664. The mean $\tau = 1$ m and $r^2 = 0.97016$ in Figure (b) and the mean $\tau = 2$ m and $r^2 = 0.91713$ in Figure (c). The solid line shows a straight line fit to the data.

8.6 Attenuation Coefficient

We assume that the wave energy, E, decays exponentially with the number of floes, i.e. $E \propto e^{-a\Lambda}$, where a is the attenuation coefficient and E is normalised with unit incidence. From Figures 8.9 and 8.10, we can see that the attenuation coefficient, a, is dependent on both $\mathcal{T}$ and τ. Figure 8.11 gives $\ln(a)$ against $\mathcal{T}$ for various τ. This figure is the cornerstone of our results. Our model provides a tool for predicting wave-attenuation in the MIZ and can be used to compare the attenuation coefficients against other, perhaps more sophisticated, models and field experiments. The figure shows that the attenuation coefficient is strongly dependent on both wave period and thickness. The attenuation coefficient for fixed period depends strongly on thickness, and the attenuation coefficient for fixed thickness depends strongly on period. This figure explains why the MIZ acts so strongly as a low-pass filter (in the sense of frequency) and how important the parameter of thickness is in determining the properties of this filtering.

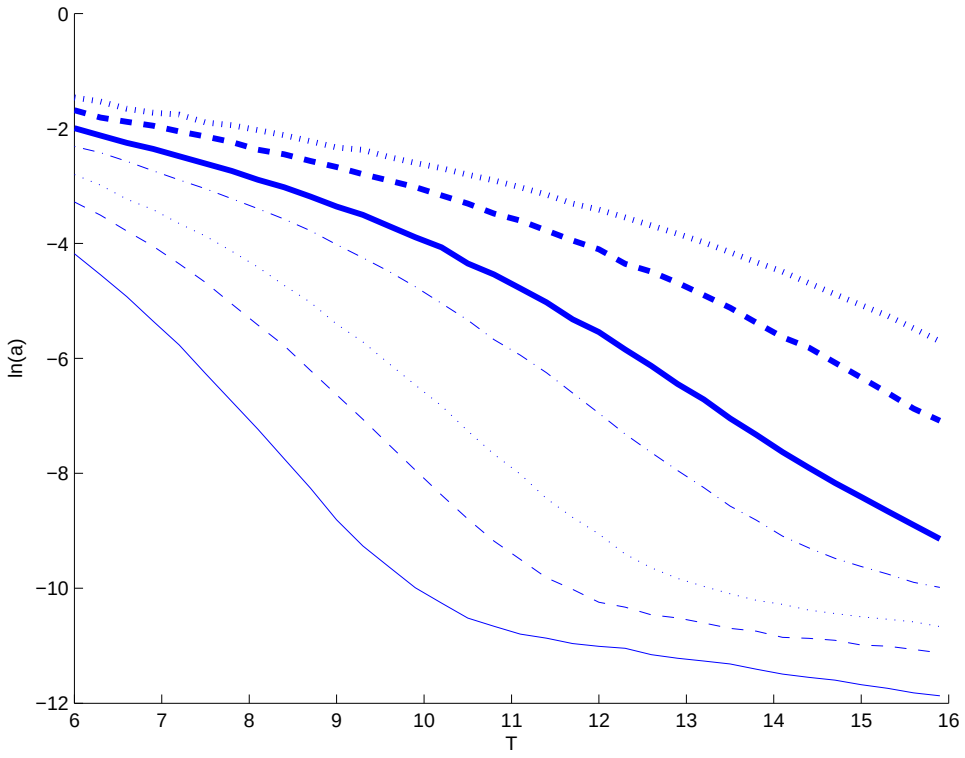

Figure 8.11: Predictions of the logarithm of the attenuation coefficient, $ln(a)$, as a function of $\mathcal{T}$ for $\tau = 0.4$ m (–), $\tau = 0.6$ m (– –), $\tau = 0.8$ m (· · ·), $\tau = 1.2$ m (– · –), $\tau = 1.6$ m (—), $\tau = 2.4$ m (— —) and $\tau = 3.2$ m (· · ·).

8.7 Strain

Given an incident wave spectrum, we can use the MEEM and our attenuation model to predict the number of floes which will be broken due to wave action. Essentially we input a given wave spectrum and calculate the number of floes which are required to reduce the wave height below which is considered minimal to induce floe breaking.

Direct measurements of sea-ice fracture took place in the Arctic, where strain gauges were fixed to the upper surface of sea-ice floes. Results from these experiments have shown an ice island to fracture at a strain of $3\text{x}10^{-5}$ (Goodman et al., 1980) and sea-ice to fracture from a strain of $4.4\text{x}10^{-5}$ to $8.5\text{x}10^{-5}$ (Squire and Martin, 1980). We assume that, in general, if the strain is less than $3\text{x}10^{-5}$, the ice will have an infinite resistance to failure (Squire, 1993; Personal correspondence with T. Haskell). Models of strain through an ice sheet combined with these experimental results can be used to predict floe breakup in a MIZ.

8.7.1 Modelling Strain

We assume we have small-amplitude waves ($\frac{\partial \eta}{\partial x}^2 \ll 1$). The strain, S, at the surface of the ice due to an incident wave is therefore

$$S(x) = \frac{\tau}{2}\frac{\partial^2 \eta(x)}{\partial x^2}, \tag{8.3}$$

where η is the displacement. Thus, S is easily derived from our expression for the displacement (4.6) and solved using the MEEM (Section 4).

In Figures 8.12 and 8.13, we plot the strain envelope (the magnitude of the complex strain) through a semi-infinite plate. Figure 8.12 is a replica of a figure produced in Fox and Squire (1991) and is included to verify our strain results. At the origin, each of these curves have zero strain and strain gradient. This is a consequence of the boundary conditions given by (3.12) and (3.13), which assume the bending moment and the shearing forces at the edges are zero. Each curve also approaches an asymptote. The asymptote value corresponds to the travelling wave due to the attenuation of the damped travelling waves and the infinite sum of evanescent waves (Fox and Squire, 1991). The strain envelope either reaches a maximum before decreasing to its asymptotic value or increases monotonically to reach the asymptote. The distance into the floe at which the maximum strain envelope occurs is more sensitive to τ than $\mathcal{T}$ (Figure 8.13a and 8.13b). This may be explained by the flexural rigidity, $D = Y\tau^3/(12(1-\nu^2))$ where Y is Young's modulus

and ν is Poisson's ratio which is proportional to τ^3 (Squire, 1993). As we would expect, small τ combined with short $\mathcal{T}$ induce the greatest strain envelope (Figure 8.14). Also, however, small τ combined with large $\mathcal{T}$ induce the least strain envelope. This suggests that the period has greatest influence on the magnitude of the strain envelope, while the floe thickness has greatest influence on the position of the maximum strain envelope (Figure 8.13).

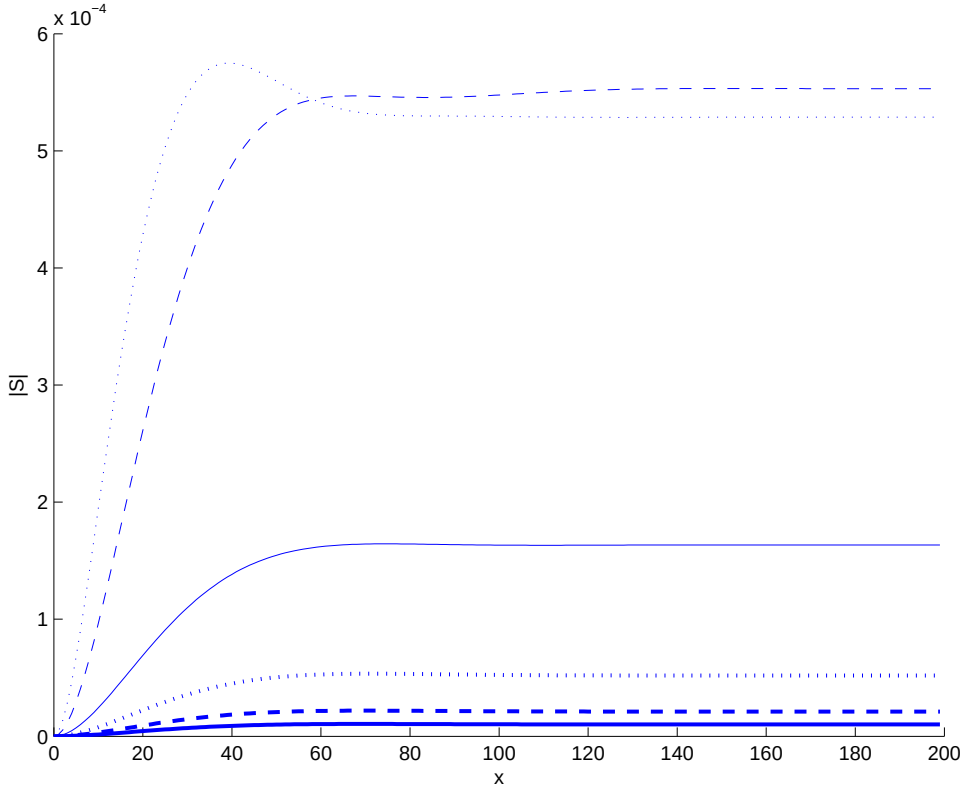

Figure 8.12: A replica of a figure produced in Fox and Squire (1991). $|S|$ as a function of x for $I = 1$, $\tau = 1$ m and $h = 100$ m. $\mathcal{T} = 5$ s $(\cdots)$, 10 s $(--)$, 15 s $(-)$, 15 s $(\cdot\cdot\cdot)$, 25 s $(--)$ and 30 s $(-)$.

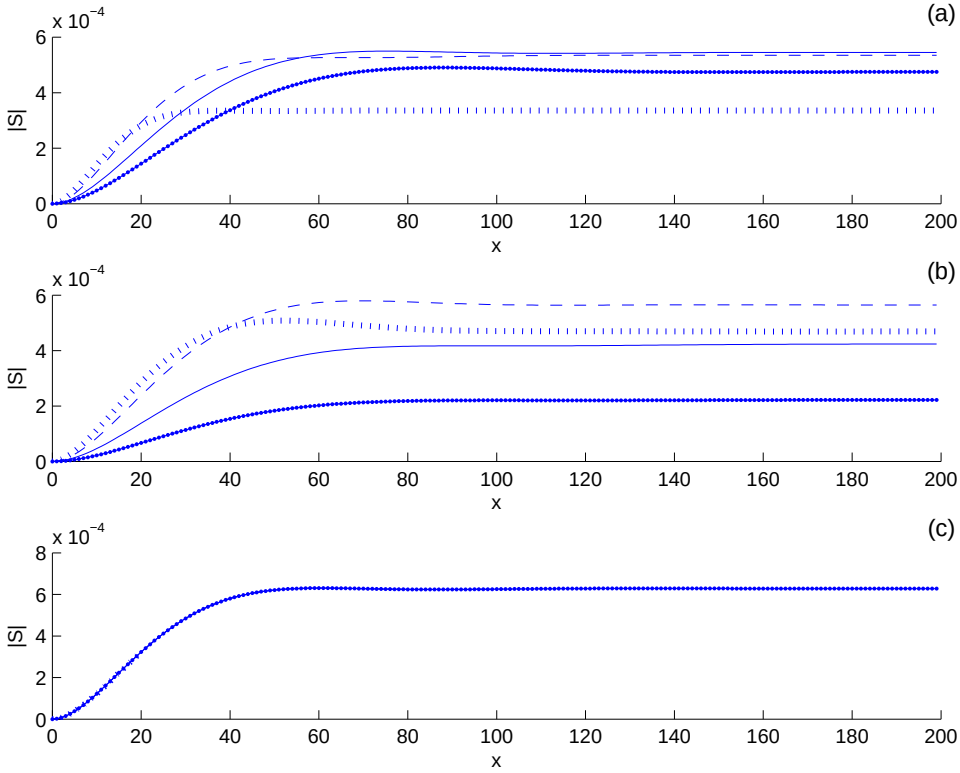

Figure 8.13: $|S|$ as a function of x for $I = 1$ and various $\mathcal{T}$, τ and L. Figure (a) has $\tau = 1.4$ m and $\mathcal{T} = 6$ s $(\cdots)$, 9 s $(- -)$, 12 s $(-)$ and 15 s $(-\circ)$. Figure (b) has $\mathcal{T} = 9$ s and $\tau = 0.4$ m $(\cdots)$, 0.8 m $(- -)$, 1.4 m $(-)$ and 2 m $(-\circ)$. Figure (c) has $\mathcal{T} = 9$ s, $\tau = 1$ and $L = 20$ m $(\cdots)$, 50 m $(- -)$, 100 m $(-)$ and 200 m $(-\circ)$.

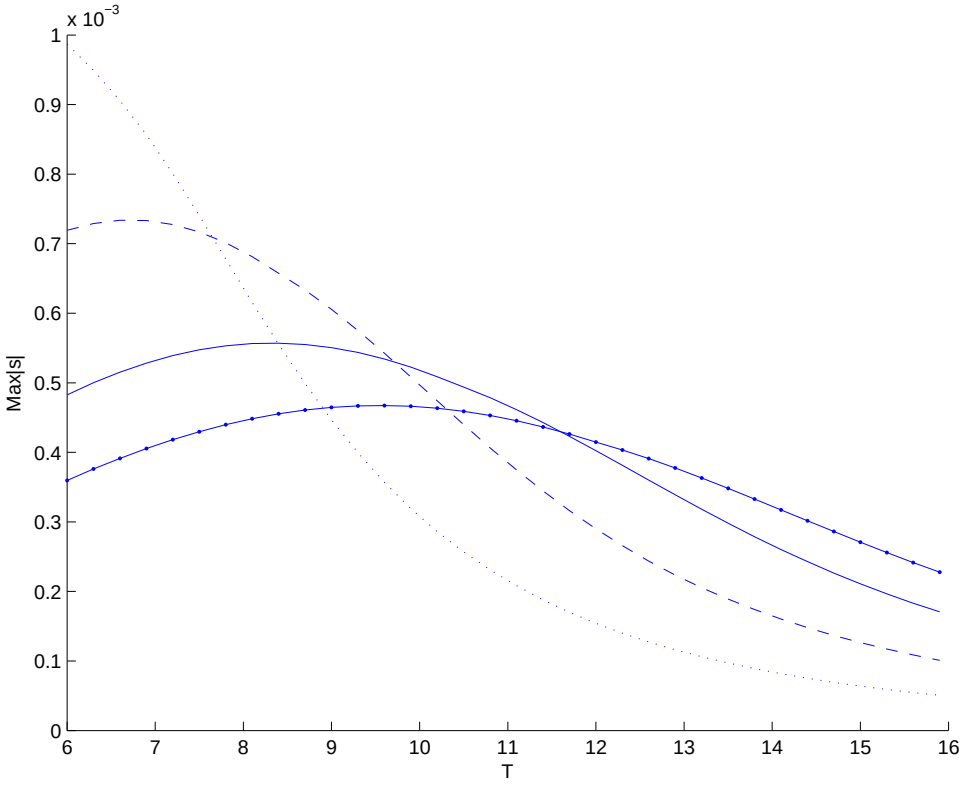

Figure 8.14: Maximum S as a function of $\mathcal{T}$ for $I = 1$ and $\tau = 0.4$ m ($\cdots$), 0.8 m ($- -$), 1.2 m ($-$) and 2 m ($-\circ$).

8.7.2 The strain for a Wave Spectrum

Section 8.7.1 considers the strain envelope for a single period only. In practice however, ocean waves consist of a power spectrum of waves, $\Upsilon(\omega)$ where ω is the frequency ($\omega = 2\pi/\mathcal{T}$), with significant energy present at periods between 4 and 20 seconds (Fox and Squire, 1991). Ideally Υ is determined from wave buoy measurements off the ice edge. Alternatively, we can use a spectral model. A model which is commonly used to describe a fully developed wind sea i.e. a storm, was developed by Pierson and Moskowitz in the early 1960's.

The Pierson–Moskowitz Spectrum

Pierson and Moskowitz (1964) made observations of fully developed wind seas using single-point time series from shipborne wave-height recorders. The Pierson–Moskowitz power spectrum formula was derived and is still the most widely used today, as it is simple to use and is one of the few based on a fully developed sea. The Pierson–Moskowitz power spectrum is given by

$$\Upsilon^p(\omega) = \zeta g^2 (2\pi) \omega^{-5} e^{\frac{5}{4}\left(\frac{\omega_m}{\omega}\right)^4}, \tag{8.4}$$

where ω_m is the peak frequency and ζ is Phillip's constant which is found experimentally to be approximately 1.2x10^{-2} (Phillips, 1977).

The JONSWAP Spectrum

During the Joint North Sea Wave Project (JONSWAP), it was found that the seas during the experiment were never fully developed (Hasselmann, 1973). In order to fit the measurements, an extra peak enhancement factor was added to the Pierson–Moskowitz spectrum. The JONSWAP spectrum is given by

$$\Upsilon^j(\omega) = \Upsilon^p(\omega) \upsilon^{e^{-\frac{(\omega-\omega_m)^2}{2\sigma^2\omega_m^2}}}, \tag{8.5}$$

where Υ^j is the JONSWAP spectrum, υ is the peak enhancement factor and σ is the peak width. υ is commonly represented by 3.3, but also can be defined as $\Upsilon_{max}/\Upsilon^p(\omega_m)$. σ is commonly defined as 0.07 for $\omega < \omega_m$ and 0.09 for $\omega > \omega_m$.

Figure 8.15 compares the Pierson–Moskowitz and JONSWAP spectrums. The examples presented herein use the Pierson–Moskowitz spectrum as it is currently the most widely used and accepted. Figure 8.16 plots the Pierson–Moskowitz spectrum for various peak

periods.

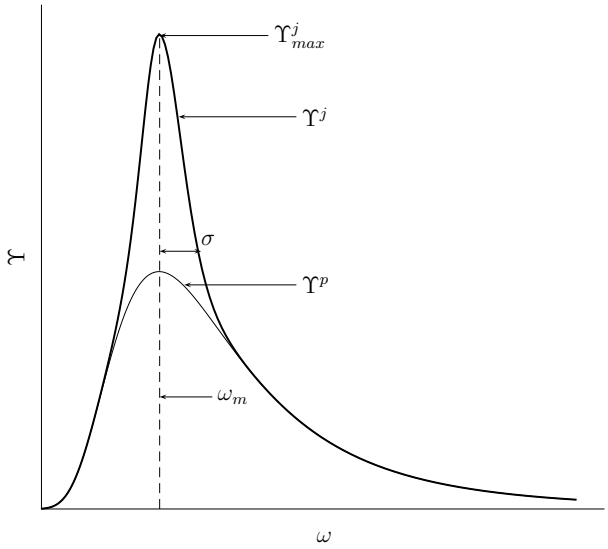

Figure 8.15: The JONSWAP (—) and Pierson–Moskowitz (−) spectrums as a function of frequency.

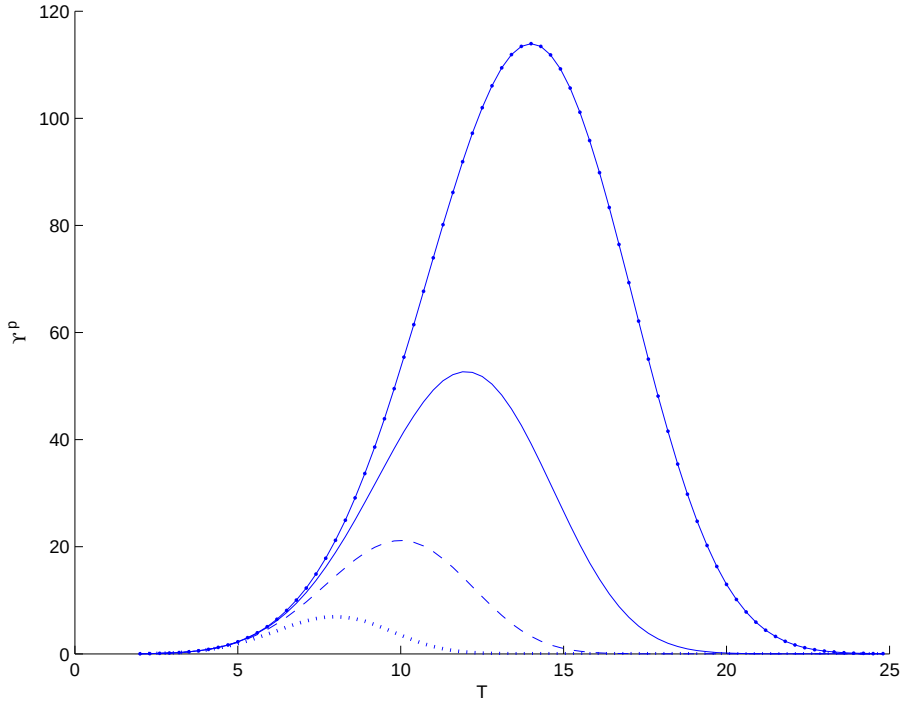

Figure 8.16: Υ^p as a function of $\mathcal{T}$ for $\mathcal{T}_m = 8$ s (· · ·), 10 s (− −), 12 s (−) and 14 s (—∘).

As the wave propagates through the ice, the wave spectrum will be altered due to dampening caused by the ice. If we can estimate the attenuation of the wave energy, we can estimate the change in the wave spectrum for a given τ and Λ so that

$$\Upsilon_\Lambda(\omega) = \Upsilon(\omega)e^{-a(\omega,\tau)\Lambda}. \tag{8.6}$$

Also, the power spectrum wave energy (E^Υ) between frequencies ω_1 and ω_2 can be expressed by $E^\Upsilon = \int_{\omega_1}^{\omega_2} \Upsilon_\Lambda(\omega)d\omega$, so that the amplitude, A, can be expressed by

$$A_\Lambda = \sqrt{\int_{\omega_1}^{\omega_2} \Upsilon_\Lambda(\omega)d\omega}. \tag{8.7}$$

Figure 8.17 shows the change in the wave spectrum with number of ice floes for a peak period of 10 s ($\omega_m = 2\pi/10$). This figure shows that there is a strong attenuation of high frequency waves and that as the thickness is increased, the cut off frequency below which there is little attenuation decreases. It is important to note that there is virtually no attenuation of the low frequency (long period) waves from our scattering model.

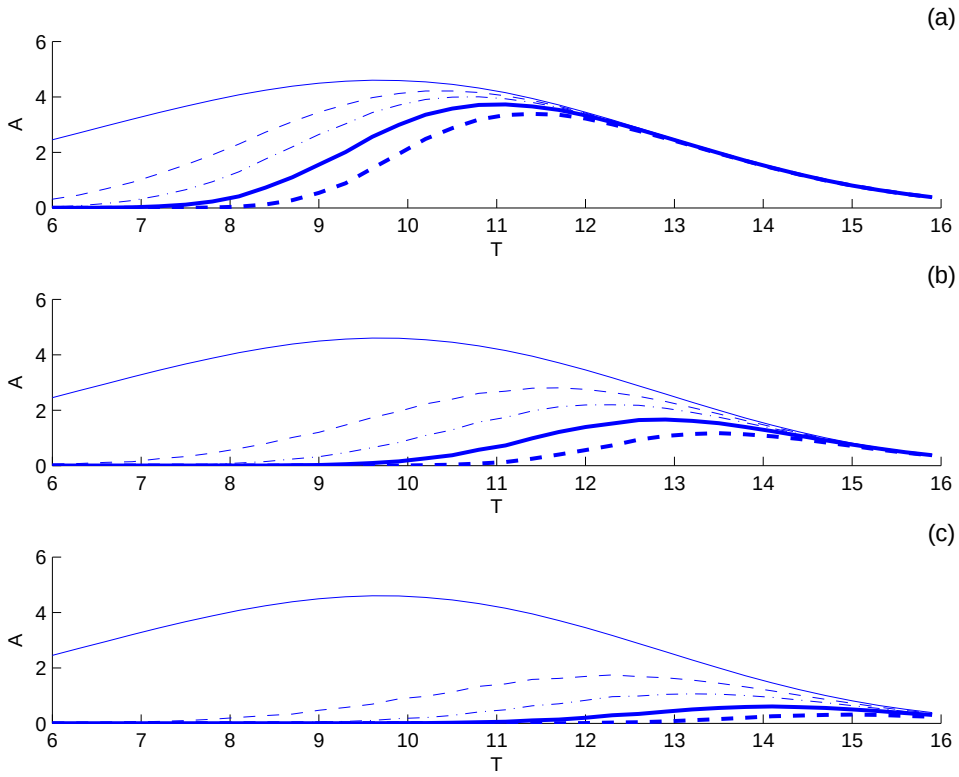

Figure 8.17: A as a function of $\mathcal{T}$ after 0 floes (–), 25 floes (– –), 50 floes (– · –), 100 floes (—) and 200 floes (— —) for $\mathcal{T}_m = 10$ s. $\tau = 1$ in Figure (a), $\tau = 2$ in Figure (b), $\tau = 3$ in Figure (c).

The strain for a particular ω as a function of time, can be calculated by multiplying $S(x,\omega)$ by $A_\Lambda(\omega)$ and by a time component such as $e^{i\omega t}$. In practice, ocean waves behave randomly. To represent this randomness, we include the phase of a wave, $e^{i\phi}$ where ϕ is a random number between 0 and 2π. We can simulate the spectral strain by summing each strain for all ω or

$$S_T = \int_0^\infty A_\Lambda(\omega) e^{i\phi} e^{i\omega t} S(x,\omega) d\omega. \tag{8.8}$$

Figure 8.18 shows that the maximum S_T can be estimated by calculating the strain envelope, which is defined as

$$S_E = \sqrt{\int_0^\infty |\Upsilon_\Lambda S|^2}. \tag{8.9}$$

Figure 8.18 also shows the effect the dampened waves have on reducing the strain.

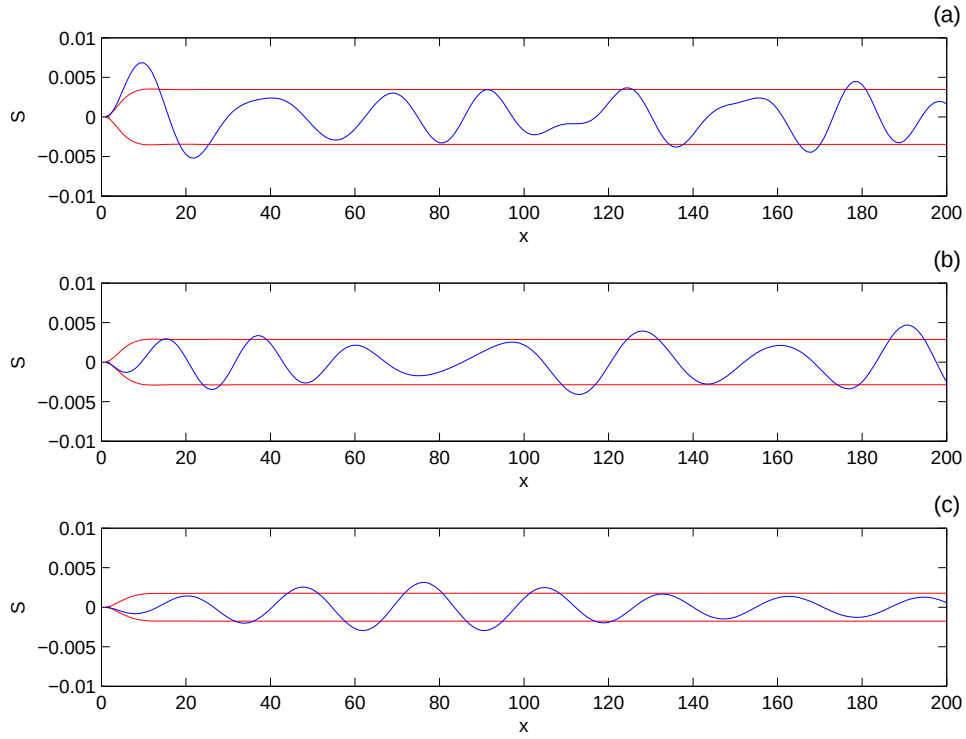

Figure 8.18: The spectral strain (S_T) and the spectral strain envelope (S_E) as a function of distance (x) with $\tau = 1$ m, $\mathcal{T}_m = 10$ s and $t = 1$. The strain in Figure (a) uses Υ_0. Figure (b) uses Υ_{20} and Figure (c) uses Υ_{200}.

Figure 8.19 shows the maximum of the strain envelope as a function of number of floes, for various floe thicknesses and an incident spectrum with peak period 8, 10 and 12 s. Also shown is the strain 3x10^{-5}, below which experiments have shown floe breakup no longer occurs. This figure implies that, for the Pierson–Moskowitz incident wave spectra with peak period, $\mathcal{T}_m$, greater than 8 s, floe breakup will occur almost indefinitely for small floe thickness. This seems anomalous and implies that our model is failing to correctly estimate the attenuation coefficient for long period waves or that the floe breaking strain is incorrectly estimated. We believe that the former is more likely due to the very small attenuation of the long period waves and conclude that our scatter model underestimates the attenuation coefficient at long periods.

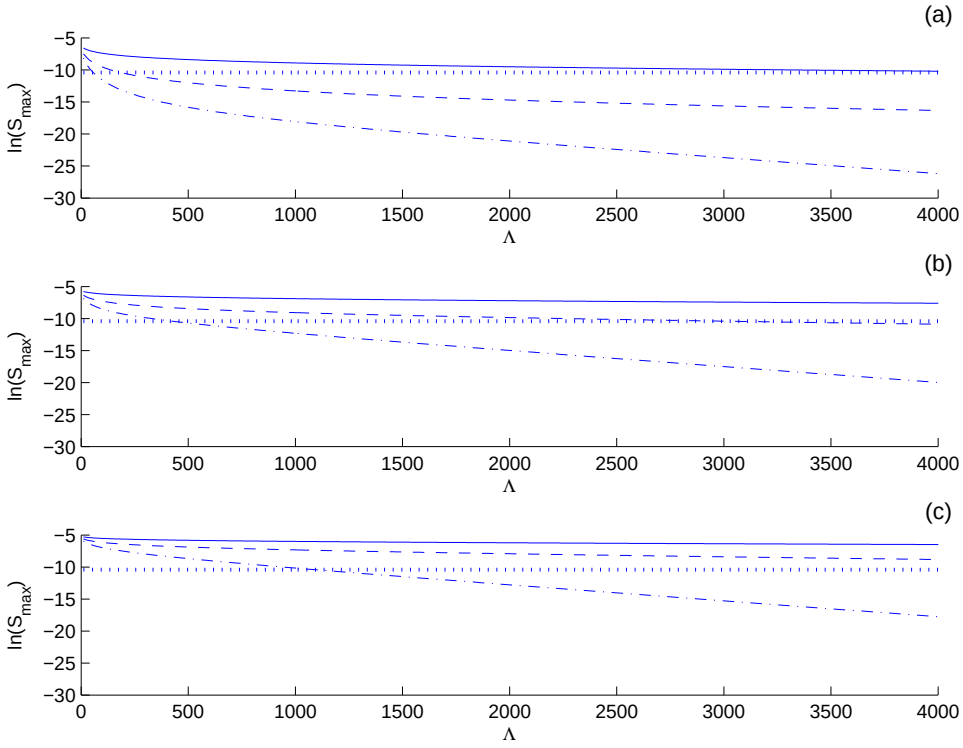

Figure 8.19: The natural logarithm of the maximum strain envelope as a function of Λ for $\tau = 1$ (−), $\tau = 2$ (− −) and $\tau = 3$ (− · −). The $MaxS_{env} = 3 \times 10^{-5}$ (· · ·) is also plotted to show the estimated strain at which floes will no longer break. Figure (a) is for $\mathcal{T}_m = 8$ s, Figure (b) is for $\mathcal{T}_m = 10$ s and Figure (c) is for $\mathcal{T}_m = 12$ s.

The significant wave height, H_s, is the most important and useful sea state parameter. The old definition of H_s was to take the mean of the one third largest waves in the sea. This, however, is not easily applied and it has become standard to define H_s as four times the standard deviation

$$H_s = 4\sqrt{\int_0^\infty \Upsilon_\Lambda(\omega)d\omega}. \tag{8.10}$$

In Figure 8.20, (8.7) is used to find H_s for a given Λ and $\tau = 1$. We find that H_s drops rapidly for increasing Λ and decreases slightly faster with increasing τ.

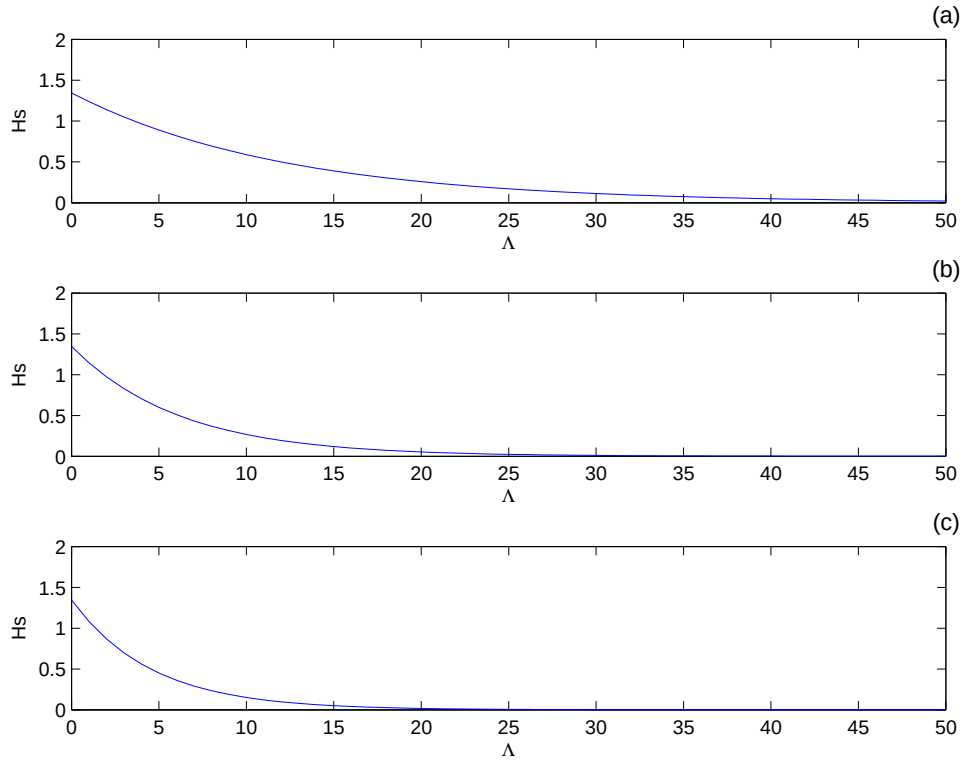

Figure 8.20: The significant wave height (H_s) as a function of the number of floes (Λ) for $T_m = 10$ s and $\tau = 1$ in Figure (a), $\tau = 2$ in Figure (b) and $\tau = 3$ in Figure (c).

9
Approximation Theory

9.1 Introduction

Our intention in this chapter is to use a theoretical approach to approximate an attenuation coefficient for multiple plates, using only the transmission and reflection coefficients from a wave travelling from a semi-infinite body of water to a semi-infinite plate. We begin this chapter by working through the theory and conclude by comparing the theory to the wave-attenuation model. The theory given in this chapter is an extension of the theory presented in Meylan and Squire (1993) and has been included in the appendix of Kohout and Meylan (2008b).

9.2 Approximation Theory

If we assume that a plate is large enough so the damped and evanescent waves diminish by the time they reach the other edge of the plate, we can consider approximations for R and T (denoted $\tilde{R}$ and $\tilde{T}$). To begin, we consider T_{pw} and R_{pw}, which are defined as the transmitted and reflected coefficients of a wave travelling from a semi-infinite plate to a semi-infinite body of water. T_{pw} and R_{pw} can be expressed in terms of T_{wp} and R_{wp}, the transmitted and reflected energy from a semi-infinite body of water to a semi-infinite

plate

$$\begin{aligned} T_{pw} &= \frac{1-|R_{wp}|}{T^*_{wp}}, \\ R_{pw} &= -\frac{R^*_{wp}T_{wp}}{T^*_{wp}} \end{aligned} \tag{9.1}$$

(Meylan, 1994) where T^* and R^* represent the conjugates of T and R. We consider the problem of a long and wide finite plate surrounded by water (Figure 9.1). We can express $\tilde{R}$ in terms of R_{wp}, b and T_{pw} (Figure 9.1), where b is the travelling wave coefficient under the plate, travelling in the negative x direction and expressed in terms of the right edge of the plate. The other terms are expressed in terms of the left edge of the plate (Figure 9.2a). Figure 9.2a, demonstrates the shift in b, so that $\tilde{R}$ can be expressed as

$$\tilde{R} = R_{wp} + be^{k_2(0)(l-r)}T_{pw}. \tag{9.2}$$

b can be expressed in terms of a and R_{pw}, where a is the travelling wave coefficient under the plate, travelling in the positive x direction and expressed in terms of the left edge of the plate. Figure 9.2b demonstrates the shift in a so that b can be expressed as

$$b = ae^{k_2(0)(l-r)}R_{pw}. \tag{9.3}$$

a can be expressed in terms of T_{wp}, R_{pw} and b. Figure 9.2c demonstrates the shift in b so that a can be expressed as

$$a = T_{wp} + be^{k_2(0)(l-r)}R_{pw}. \tag{9.4}$$

Finally, $\tilde{T}$ can be expressed in terms of T_{pw} and a. Figure 9.2d demonstrates the shift in a so that $\tilde{T}$ can be expressed as

$$\tilde{T} = ae^{k_2(0)(l-r)}T_{pw}. \tag{9.5}$$

Equating (9.3) and (9.4) gives

$$\begin{aligned} a &= \frac{T_{wp}}{1-R^2_{pw}e^{2k_2(0)(l-r)}}, \\ b &= \frac{T_{wp}R_{pw}e^{k_2(0)(l-r)}}{1-R^2_{pw}e^{2k_2(0)(l-r)}}. \end{aligned} \tag{9.6}$$

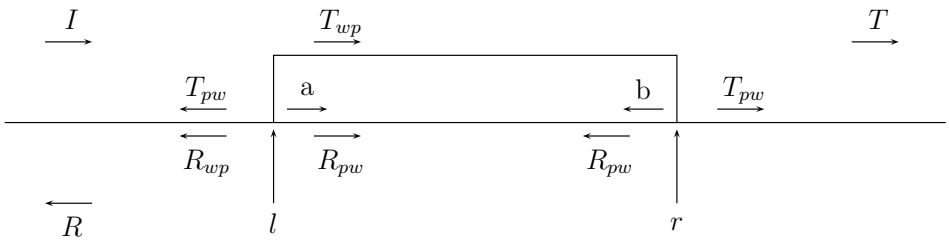

Figure 9.1: Wave propagation through a long and wide finite plate where I is the incident wave coefficient, R is the total reflected wave coefficient, T is the total transmitted wave coefficient, R_{pw} and T_{pw} are the reflected and transmitted wave coefficients from plate to water, T_{wp} and R_{wp} are the reflected and transmitted wave coefficients from water to plate, a and b are the travelling wave coefficients under the plate and l and r are the x-co-ordinates for the left and right edges of the plate.

so that (9.2) and (9.5) can be expressed as

$$\begin{aligned}\tilde{R} &= R_{wp} + \frac{T_{wp}T_{pw}R_{pw}e^{2k_2(0)(l-r)}}{1 - R_{pw}^2 e^{2k_2(0)(l-r)}},\\ \tilde{T} &= \frac{T_{wp}T_{pw}e^{k_2(0)(l-r)}}{1 - R_{pw}^2 e^{2k_2(0)(l-r)}}.\end{aligned} \tag{9.7}$$

Substituting (9.1) gives

$$\begin{aligned}\tilde{R} &= R_{wp} - \frac{R_{wp}^* T_{wp}^2 (1 - |R_{wp}|)e^{2k_2(0)(l-r)}}{T_{wp}^{*2} - R_{wp}^{*2} T_{wp}^2 e^{2k_2(0)(l-r)}},\\ \tilde{T} &= \frac{|T_{wp}|^2 (1 - |R_{wp}|)e^{k_2(0)(l-r)}}{T_{wp}^{*2} - R_{wp}^{*2} T_{wp}^2 e^{2k_2(0)(l-r)}},\end{aligned} \tag{9.8}$$

which satisfies the energy balance equation, $|\tilde{R}|^2 + |\tilde{T}|^2 = 1$. We compare the approximation theory to the MEEM and find they agree perfectly for sufficiently long plates (Figure 9.3). The point where the two plots merge, defines the point where the first evanescent mode under the plate decays enough to be negligible and the approximation theory can be applied.

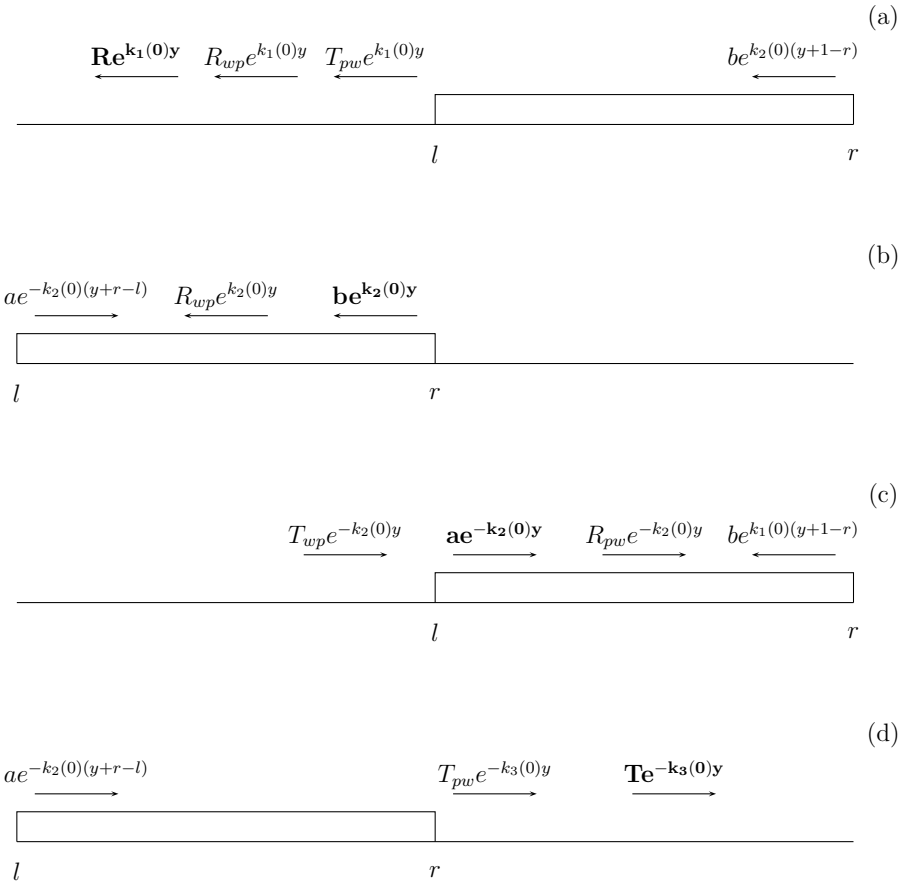

Figure 9.2: A detailed schematic diagram showing the wave reflection and transmission through a long and wide finite plate. Figure (a) shows the terms which make up the total reflected wave where $R = R_{pw} + be^{k_2(0)(l-r)}T_{pw}$ and demonstrates the shift in notation for b by letting $y = x - l$. Figure (b) shows the terms which make up b where $b = ae^{k_2(0)(l-r)}R_{pw}$ and demonstrates the shift in notation for a by letting $y = x - r$. Figure (c) shows the terms which make up a where $a = T_{wp} + be^{k_2(0)(l-r)}R_{pw}$ and demonstrates the shift in notation for b by letting $y = x - l$. Figure (d) shows the terms which make up T where $T = ae^{k_2(0)(l-r)}T_{pw}$ and demonstrates the shift in notation for T by letting $y = x - r$. $k_\mu(0)$ is the travelling wave number under the μ^{th} plate, where $\mu = 1$ is the semi-infinite open water plate on the left, $\mu = 2$ is the long finite plate, and $\mu = 3$ is the semi-infinite plate on the right.

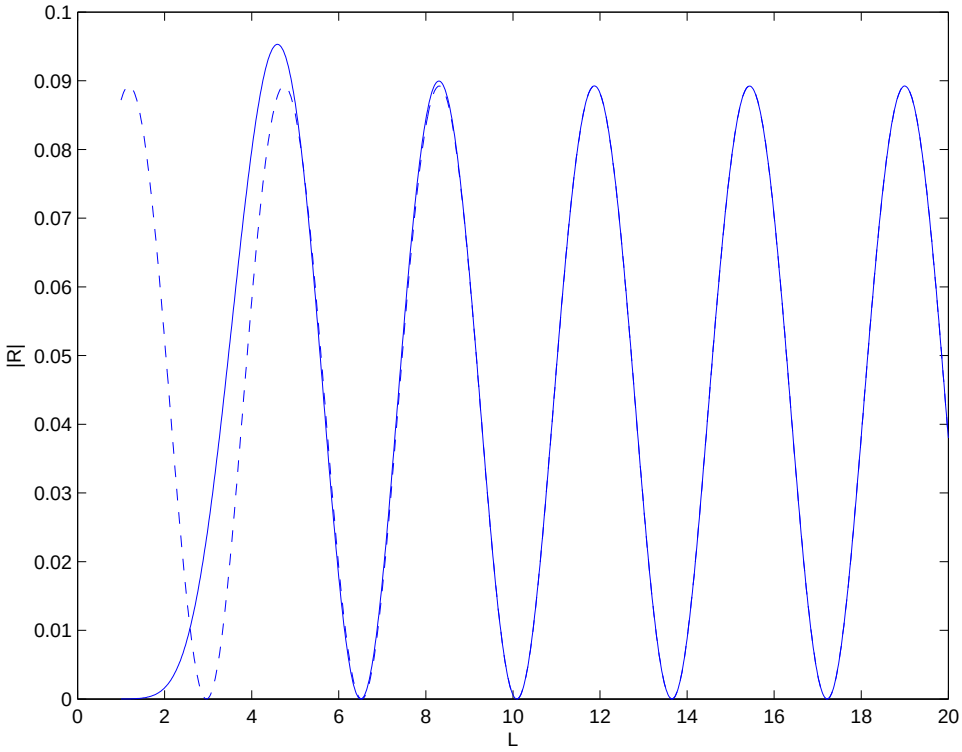

Figure 9.3: The absolute value of the reflection coefficient, $|R|$ as a function of floe length, L for a finite plate surrounded by water with $\alpha = 1$, β under the plate = 1, γ under the plate = 0, $\tau = 1$ and $h = 1$. The solid line gives $|R|$ using the MEEM for one plate and the dashed line gives $|R|$ using the approximation theory. Note the point where the two plots merge corresponds to the point at which the first evanescent mode under the plate decays enough to become negligible.

9.3 Wave Attenuation Approximation

Since, $\tilde{T}$ in (9.8) is periodic with respect to floe length, we can calculate the average of $|\tilde{T}|^2$ over one period i.e.

$$|T_{av}|^2 = \frac{1}{2\pi}\int_0^{2\pi} \frac{|T_{wp}T_{pw}e^{k_2(0)(l-r)}|^2}{|1 - R_{wp}e^{2k_2(0)(l-r)}|^2}dt \tag{9.9}$$

(Williams, 2005). We solve via complex integration and the residue theorem (see Appendix B) to give

$$|T_{av}|^2 = \frac{|T_{wp}T_{pw}|^2}{1 - |R_{wp}|^2}. \tag{9.10}$$

The approximation for $|T_{av}|^2$ for one plate can be extended to multiple plates, $E_\Lambda = (|T_{av}|^2)^\Lambda = e^{-a\Lambda}$ (Section 8.6). The approximation for the attenuation coefficient, $\tilde{a}$ can

therefore be expressed as

$$\tilde{a} = -\ln(|T_{av}|^2). \tag{9.11}$$

Note that a similar approximation for single scattering is given in Wadhams et al. (1988). The only difference is that their approximation is based on a solution for a single finite floe surrounded by water, so that T_{av} is replaced by T_3 (the transmission coefficient for a single floe). A similar approximation based on multiple scattering is presented in Wadhams (1986) and is given by

$$\tilde{a} = -\frac{1}{2}\ln\left(\frac{|T_3|^2}{2-|T_3|^2}\right). \tag{9.12}$$

Note that the approximations in Wadhams et al. (1988) and Wadhams (1986) become equal in the limit of small T_3. Figure 9.4 shows a comparison between the attenuation coefficients from our model (Section 8.6) and the attenuation coefficients from the approximations given in (9.11) and (9.12). Note that in Figure 9.4 and any subsequent comparisons, our estimate of T_{av} is used to replace T_3 in 9.12. In Figure 9.4, the approximate theories show exactly the same trends as the full scattering theory. The reason why the scattering coefficient is lower for our model is because our model allows for all scattering (and conserves energy).

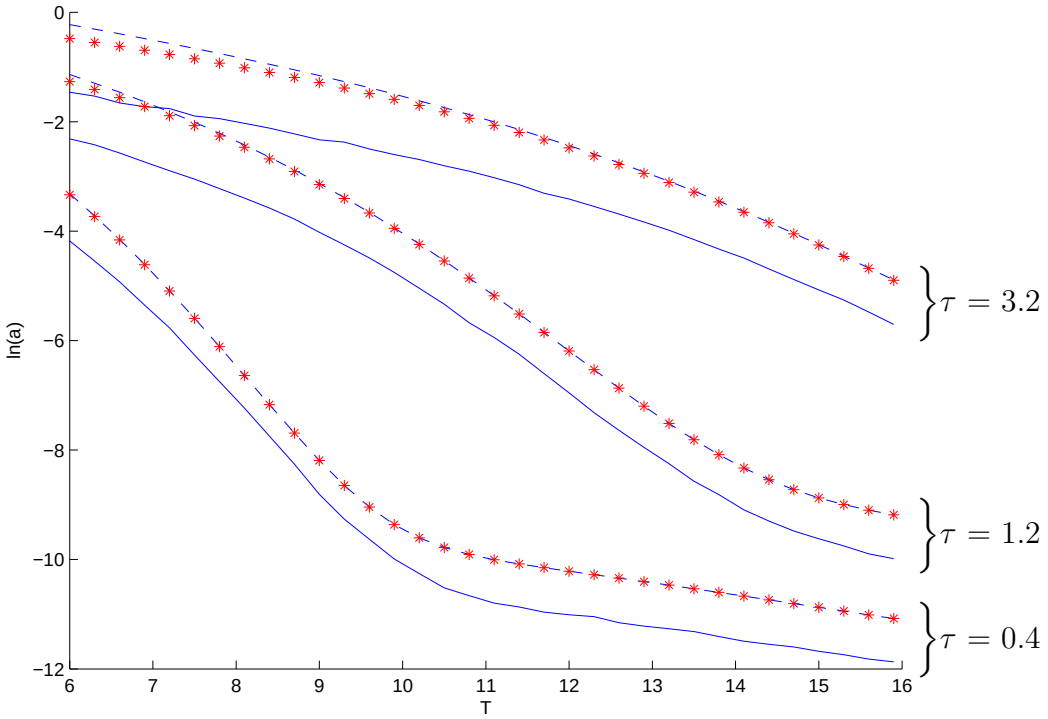

Figure 9.4: A comparison between the attenuation coefficient from the model ('-') versus the attenuation coefficients from the approximation theories, for τ = 0.4, 1.2 and 3.2 m. The dashed line (- -) give the attenuation coefficients from (9.11) and the data points (*) give the attenuation coefficients from (9.12)

10

Comparing Theory to Experiments

10.1 Introduction

Theory and experiment need to work together to understand complicated geophysical phenomena such as wave–ice interactions. It is important to realise that the present situation is one where there has been much more progress with modelling than with experiments. We are reliant on data sets which are nearly thirty years old. This is highly unsatisfactory, and from a modeller's perspective we have great need for more and better experimental results.

In this section, we compare results from the MEEM to results from a wave-tank experiment, which was designed to simulate wave propagation in the MIZ. A description of this experiment and the results have been published in Kohout et al. (2007). The next section compares our wave-attenuation model to several field experiments performed in both the Arctic and Antarctic. These experiments and results are described in Kohout and Meylan (2008b).

10.2 Wave Tank Experiment

Solutions from the MEEM are compared to a series of experiments which were performed in a two-dimensional wave-tank. These experiments were aimed at simulating wave propagation in the Marginal Ice Zone. The results concerned with determining the dispersion equation are described in Sakai and Hanai (2002).

A 26 m long, 0.8 m wide and 0.6 m deep wave-tank was used for the experiment. The waves were generated using a wave-maker at the front of the tank and an active wave absorption system was used at the far end of the tank. Elastic plates were placed on the surface of the wave-tank, with negligible gap in between the plates. The plates occupied the entire width of the tank and in total occupied 8 m in length. We will compare our theory with the experiments performed with one 8 m plate, two 4 m plates, four 2 m plates, eight 1 m plates, sixteen 1/2 m plates and 32 1/4 m plates.
The elastic plate was either 5 mm or 20 mm thick. For the 5 mm plate, the Young's modulus Y was approximately 850 MPa $(824 - 868MPa)$ and 650 MPa $(624 - 712MPa)$for the 20 mm plate. The specific gravity of the polyethylene plates was 0.914. The vertical displacement was measured at 25 different points along the plate using ultra-sonic sensors. We assume that Poisson's ratio, ν, is 0.3, g is 9.8 ms^{-2} and the density of water, ρ_w, is 1000.0 kgm^{-3}.

We found better agreement between measurement and theory for the 20 mm plates than for the 5 mm plates. Figures 10.1 and 10.2 are a sample of the 5 mm comparisons between theory and experiment. Figures 10.3 to 10.7 compare the different amplitudes of the 20 mm plate experiments. These figures show that the experimental amplitudes are within the linear regime, as only uniform linear changes occur in the measured results as the amplitude increases. Figures 10.8 to 10.13 have therefore been simplified by standardising the incident amplitude to 1. For each figure, we compare results for $\mathcal{T} = 0.8$, 1, 1.2, 1.4 and 1.6 s. These figures generally show good agreement, with a trend of increasing agreement as $\mathcal{T}$ increases and increasing agreement as Λ decreases. For $\Lambda = 32$, there is strong disagreement for all $\mathcal{T}$. There is also one surprisingly poor agreement in Figure 10.9d. We are uncertain about the origin of this inconsistency. We however suggest that as the amplitudes of the experiment seem restricted at the plate edge, the discrepancy may be due to some sort of friction at the edges which is restricting the plate's freedom of movement.

Overall the agreement between the MEEM and the experiment is good, especially consid-

ering that we are plotting the amplitude of displacement. Differences that do occur may be explained by experimental errors, such as the reflected wave not being fully dampened by the wave buoy at the end of the flume. Alternatively, the difference may be due to a measurement error such as the calculation of Young's modulus. The cusps apparent in Figure 10.10 for $\mathcal{T} = 0.8$ s, are caused by the plates being so short as to be almost rigid and by having a near zero in displacement. The effect when plotting the absolute value of displacement, is a cusp. We believe that overall these comparisons provide strong confirmation that our theory is correct for plates of uniform thickness. It would be interesting to run an experiment with the plates alternating in thickness, say between 10 mm and 30 mm thick.

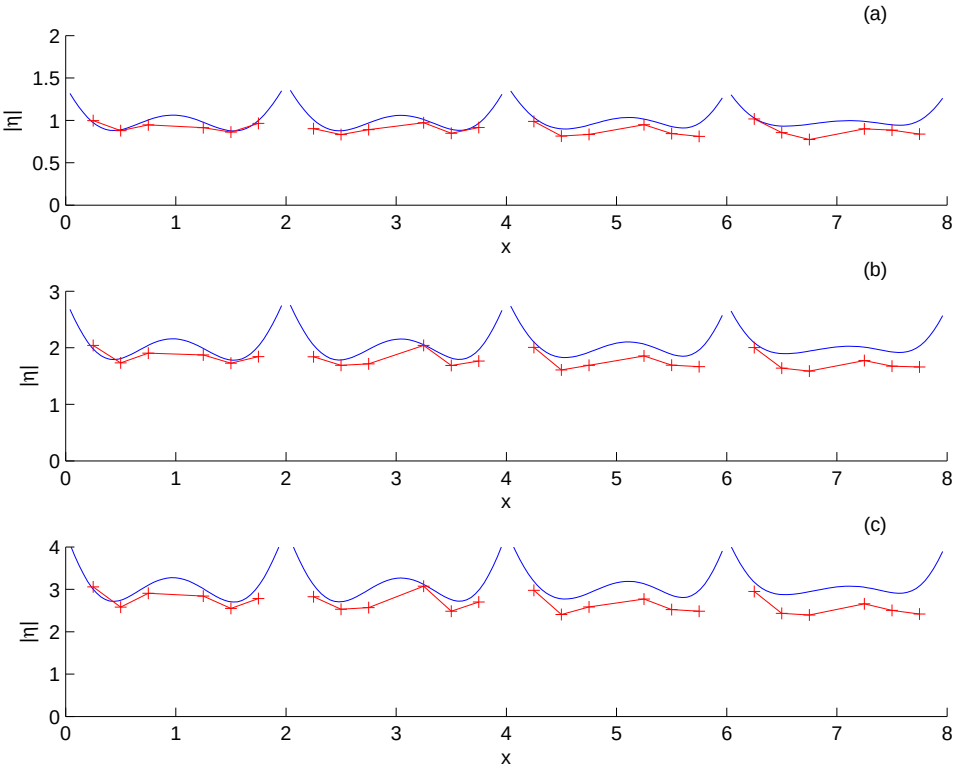

Figure 10.1: $|\eta|$ from the MEEM and from the experiment (pluses) for four plates 5 mm thick with $\mathcal{T} = 1.2$ s and incident amplitude 1.18 (a), 2.4 (b) and 3.64 (c).

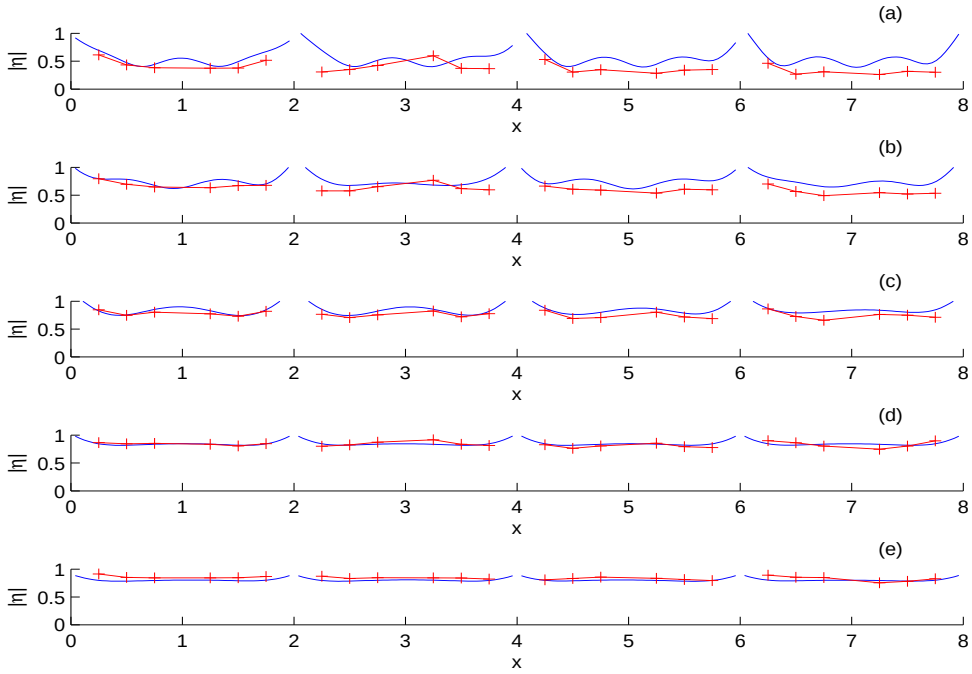

Figure 10.2: $|\eta|$ from the MEEM and from the experiment (pluses) for a single plate 5 mm thick with $A = 1$ and $\mathcal{T} = 0.8$ s (a), $\mathcal{T} = 1.0$ s (b), $\mathcal{T} = 1.2$ s (c), $\mathcal{T} = 1.4$ s (d) and $\mathcal{T} = 1.6$ s (e).

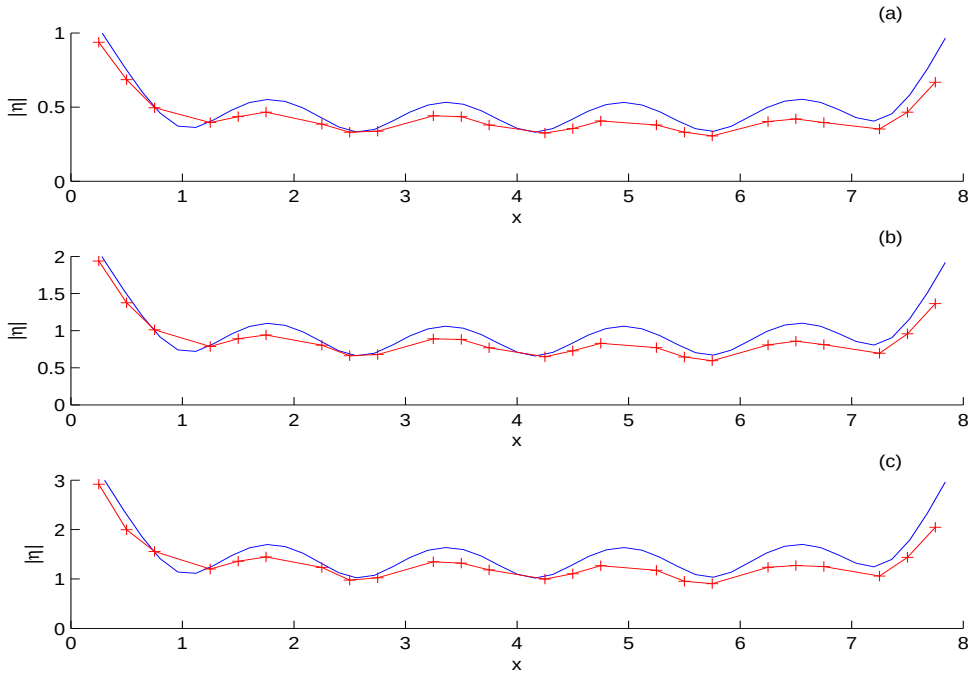

Figure 10.3: $|\eta|$ from the MEEM and from the experiment (pluses) for a single plate 20 mm thick with $\mathcal{T} = 1.2$ s and incident amplitude 1.21 (a), 2.41 (b) and 3.72 (c).

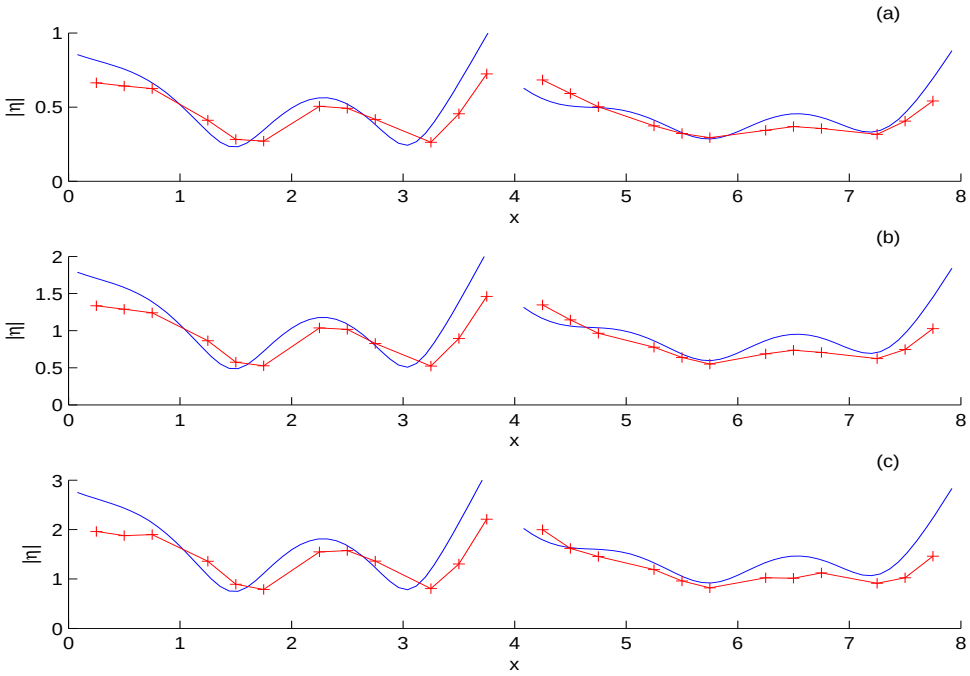

Figure 10.4: $|\eta|$ from MEEM and from the experiment (pluses) for two plates 20 mm thick with $\mathcal{T} = 1.2$ s and incident amplitude 1.18 (a), 2.47 (b) and 3.8 (c).

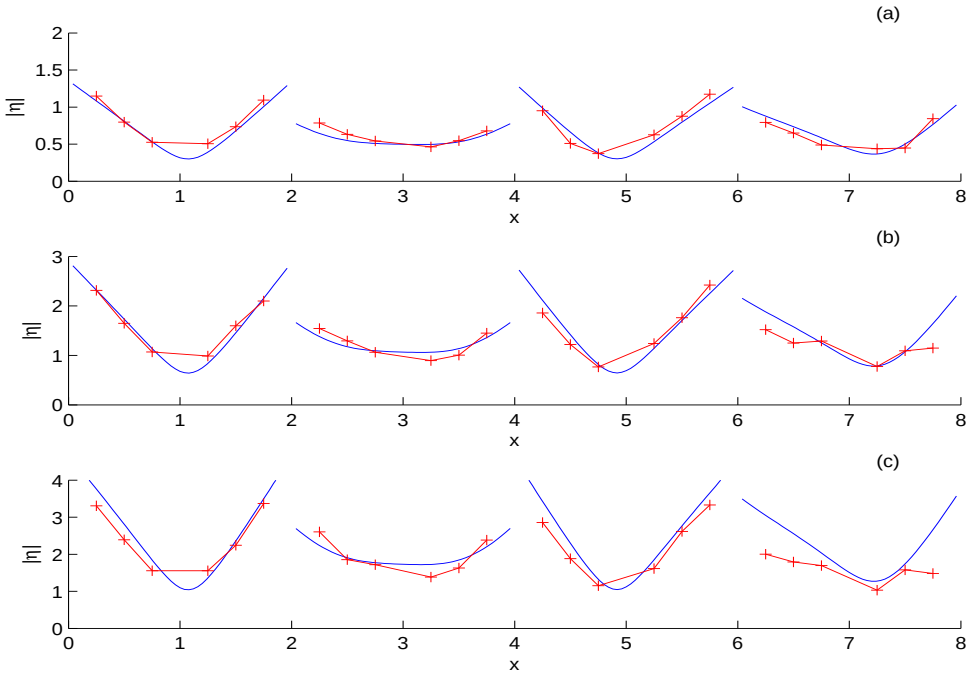

Figure 10.5: $|\eta|$ from MEEM and from the experiment (pluses) for four plates 20 mm thick with $\mathcal{T} = 1.2$ s and incident amplitude 1.12 (a), 2.4 (b) and 3.89 (c).

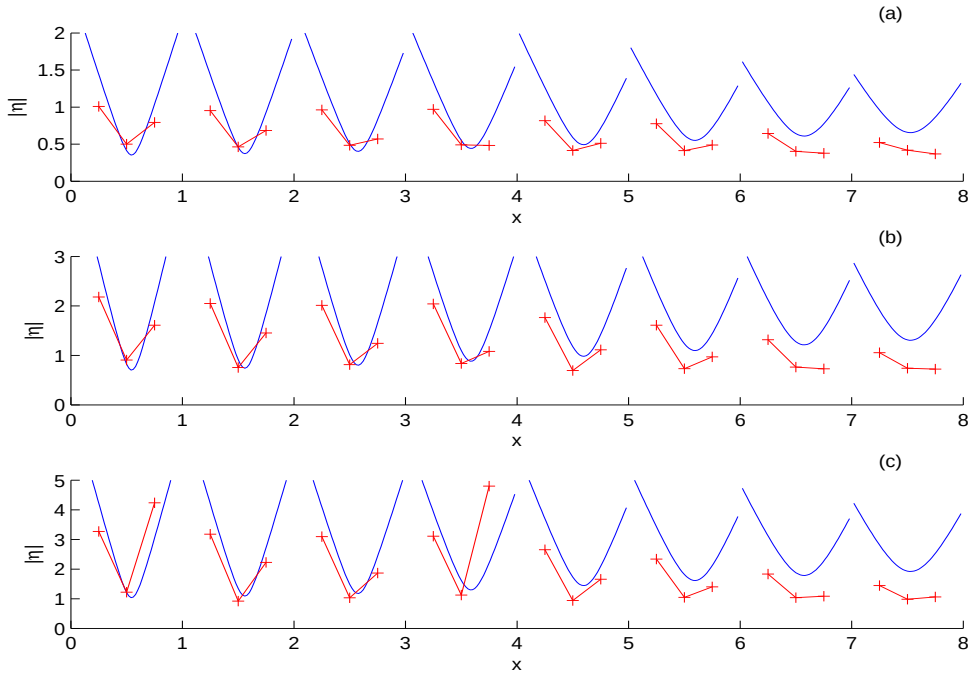

Figure 10.6: $|\eta|$ from MEEM and from the experiment (pluses) for eight plates 20 mm thick with $\mathcal{T} = 1.2$ s and incident amplitude 1.3 (a), 2.59 (b) and 3.81 (c).

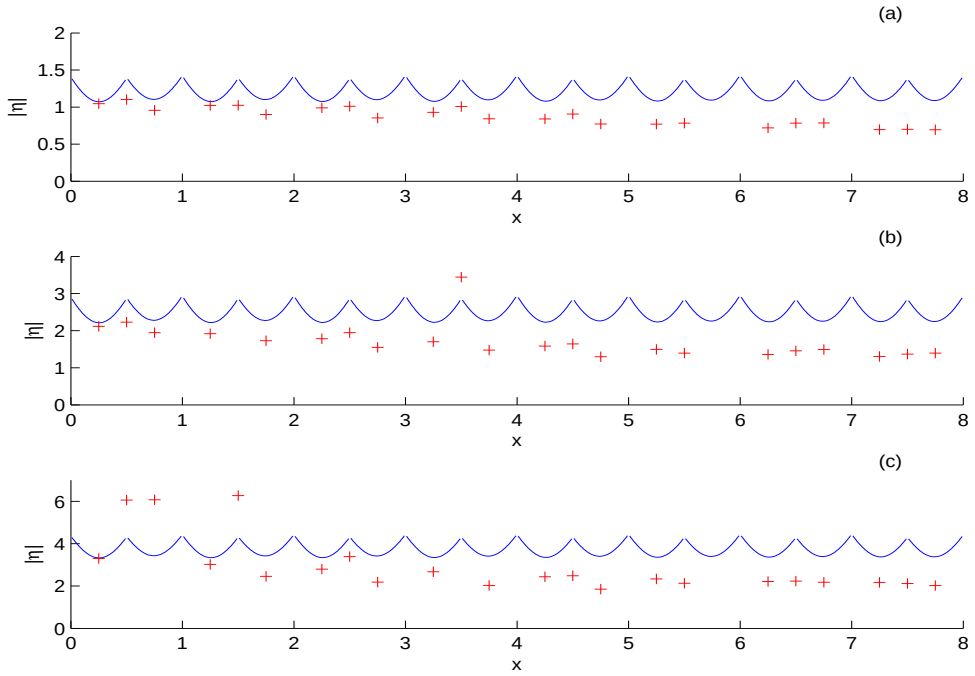

Figure 10.7: $|\eta|$ from MEEM and from the experiment (pluses) for sixteen plates 20 mm thick with $\mathcal{T} = 1.2$ s and incident amplitude 1.22 (a), 2.52 (b) and 3.79 (c).

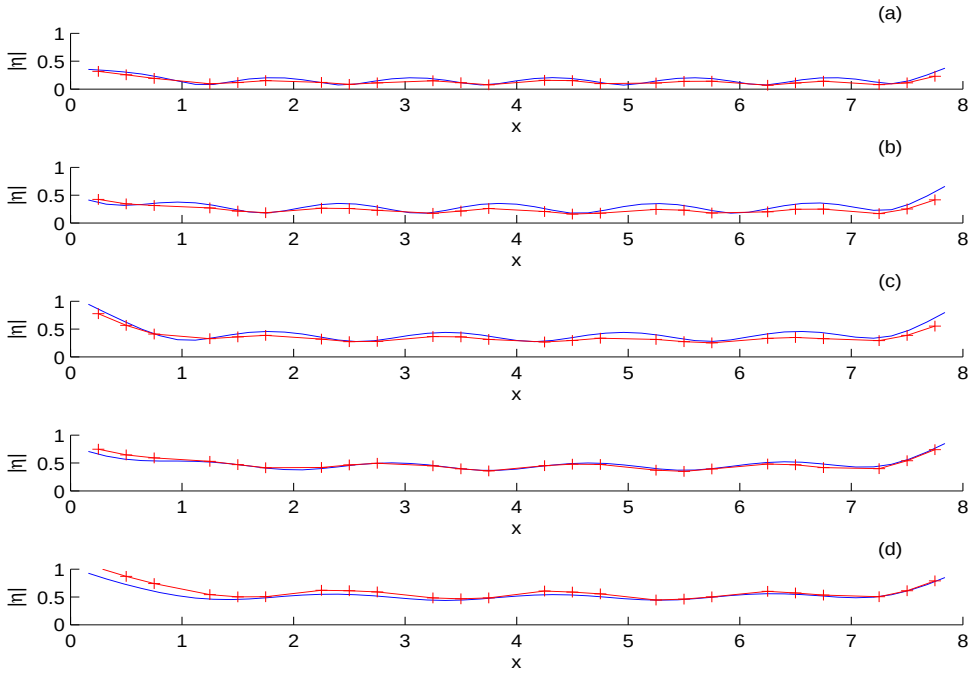

Figure 10.8: $|\eta|$ from MEEM and from the experiment (pluses) for a single plate 20 mm thick with $A = 1$ and $\mathcal{T} = 0.8$ s (a), $\mathcal{T} = 1.0$ s (b), $\mathcal{T} = 1.2$ s (c), $\mathcal{T} = 1.4$ s (d) and $\mathcal{T} = 1.6$ s (e).

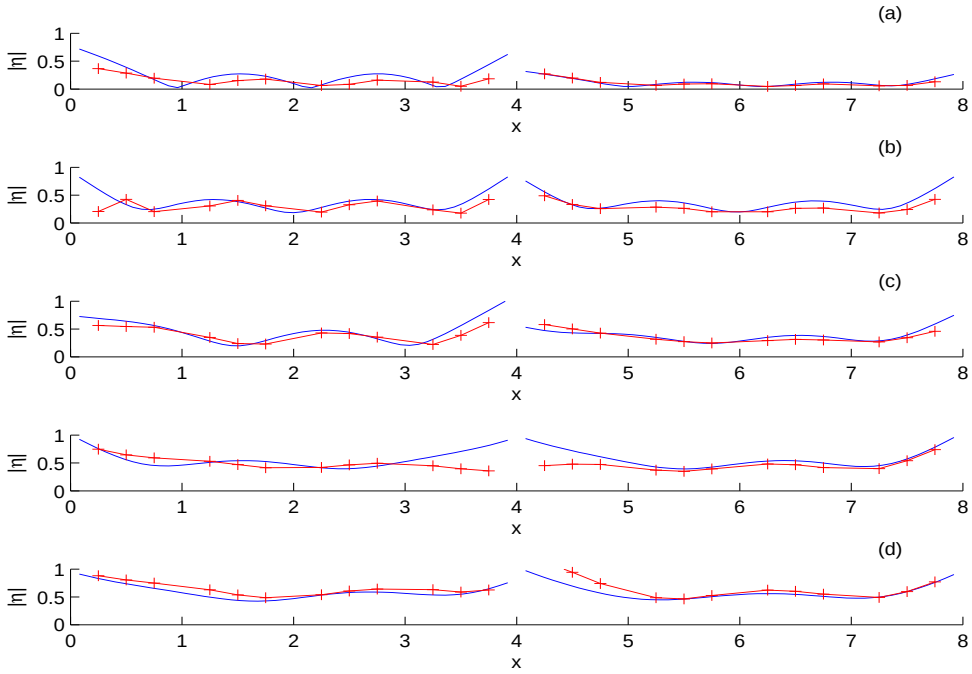

Figure 10.9: $|\eta|$ from MEEM and from the experiment (pluses) for two plates 20 mm thick with $A = 1$ and $\mathcal{T} = 0.8$ s (a), $\mathcal{T} = 1.0$ s (b), $\mathcal{T} = 1.2$ s (c), $\mathcal{T} = 1.4$ s (d) and $\mathcal{T} = 1.6$ s (e).

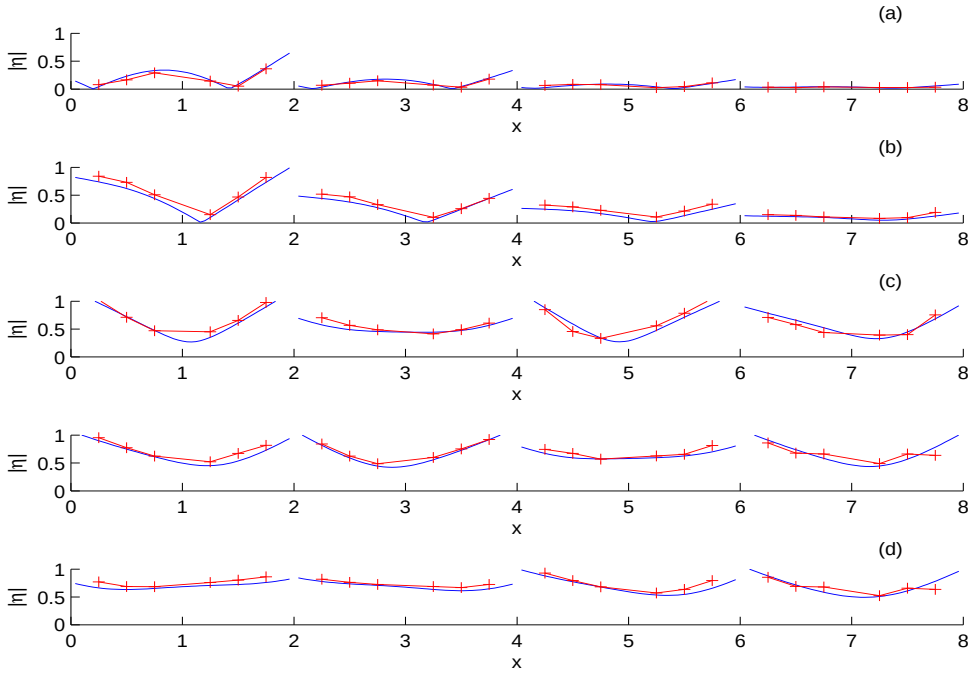

Figure 10.10: $|\eta|$ from MEEM and from the experiment (pluses) for four plates 20 mm thick with $A = 1$ and $\mathcal{T} = 0.8$ s (a), $\mathcal{T} = 1.0$ s (b), $\mathcal{T} = 1.2$ s (c), $\mathcal{T} = 1.4$ s (d) and $\mathcal{T} = 1.6$ s (e).

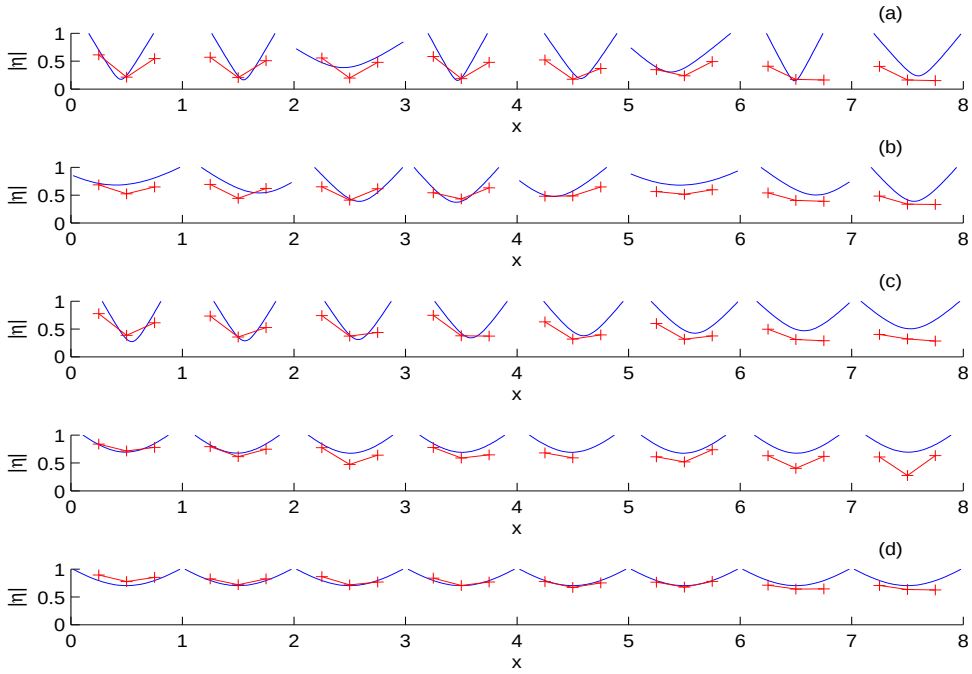

Figure 10.11: $|\eta|$ from MEEM and from the experiment (pluses) for eight plates 20 mm thick with $A = 1$ and $\mathcal{T} = 0.8$ s (a), $\mathcal{T} = 1.0$ s (b), $\mathcal{T} = 1.2$ s (c), $\mathcal{T} = 1.4$ s (d) and $\mathcal{T} = 1.6$ s (e).

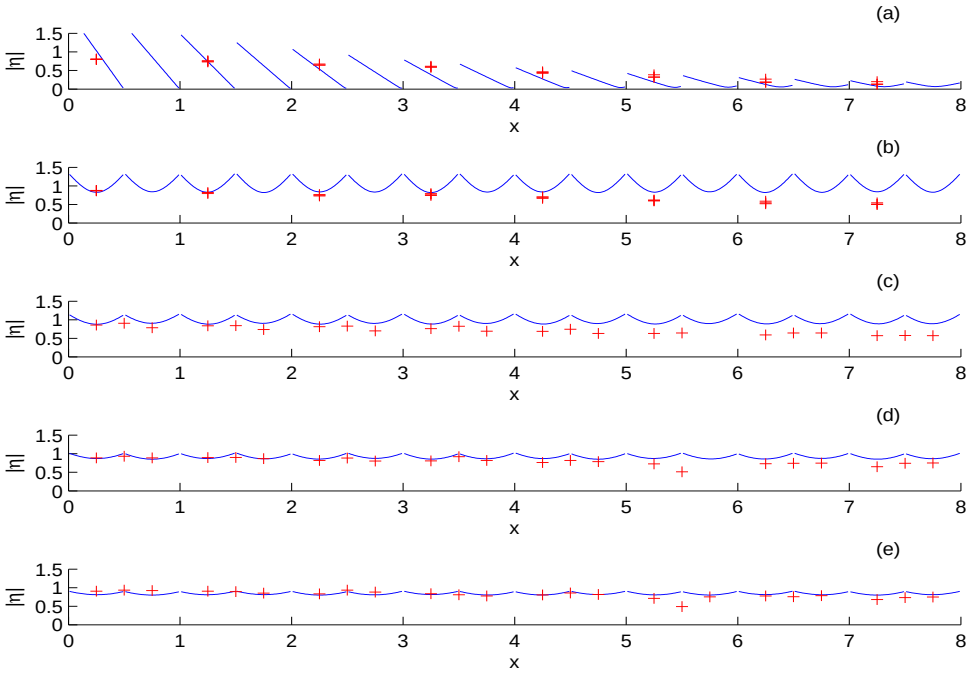

Figure 10.12: $|\eta|$ from MEEM and from the experiment (pluses) for sixteen plates 20 mm thick with $A = 1$ and $\mathcal{T} = 0.8$ s (a), $\mathcal{T} = 1.0$ s (b), $\mathcal{T} = 1.2$ s (c), $\mathcal{T} = 1.4$ s (d) and $\mathcal{T} = 1.6$ s (e).

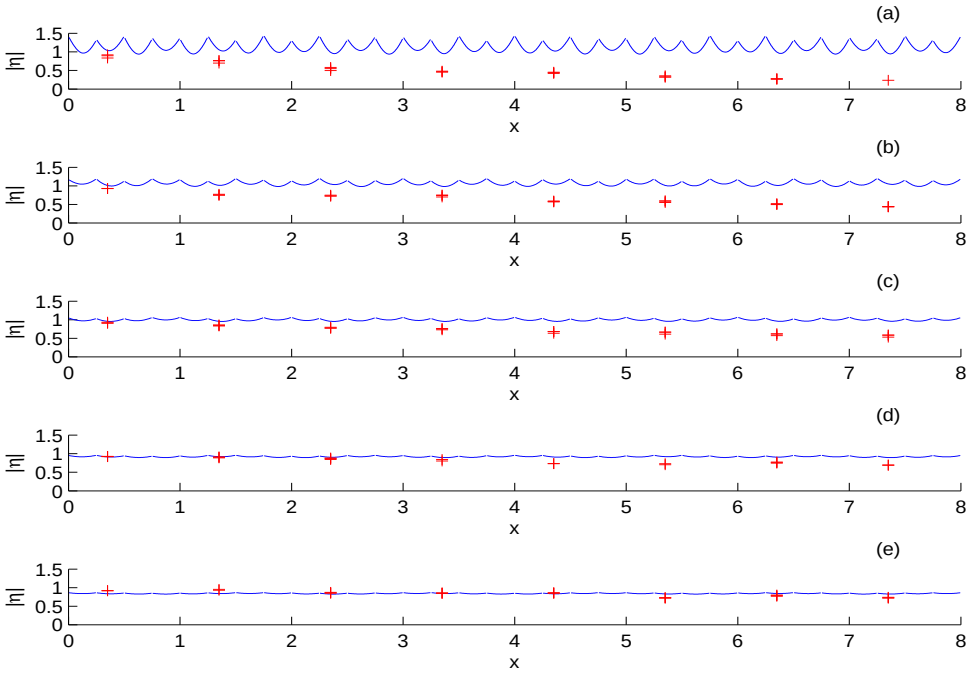

Figure 10.13: $|\eta|$ from MEEM and from the experiment (pluses) for thirty-two plates 20 mm thick with $A = 1$ and $\mathcal{T} = 0.8$ s (a), $\mathcal{T} = 1.0$ s (b), $\mathcal{T} = 1.2$ s (c), $\mathcal{T} = 1.4$ s (d) and $\mathcal{T} = 1.6$ s (e).

10.3 Field Experiments

We compare the energy attenuation coefficients from our attenuation model (Section 8.6) and the single scatter approximation given by (9.11), against the SPRI experimental data set (Section 2.3.2). We also compare the model and approximation theory to a set of experiments carried out using an autonomous underwater vehicle (AUV) in the western Bellingshausen Sea (Section 2.3.2). Although we do not expect our model to compare well against the AUV data, as it is based on ice conditions with small floe lengths and high ice concentrations, comparisons can help us define the limits of our model. In addition, we compare our model to the wave-attenuation model presented in Perrie and Hu (1996) (Section 2.3.1). It would also be beneficial to compare our model to the LIMEX data set (Section 2.3.2), but unfortunately we have been unable to obtain this data.

The measured attenuation coefficients, $\breve{a}$, provided in Wadhams et al. (1988) and Hayes et al. (2007), are calculated from fitting an exponential curve of E as a function of distance from the ice edge. Our energy attenuation coefficients, a, depends on the number of floes ($\Lambda = XC/L$ where L is the average length of the floes, C is the floe concentration (the ratio of ice floes to open water), and X is the total distance). Therefore $\breve{a} = aC/L$. We present the attenuation coefficients in Appendix C and in Figures 10.14 to 10.21. Generally, we plot the experimental data points with error bars, the predicted value from our model as a solid line, the approximation theory as a dashed line and Perrie and Hu (1996)'s model as a dashed line.

10.3.1 Greenland Sea 1979

In 1979, two experiments were made in the King Oscars Fjord area of east Greenland (Wadhams, 1979). During the first experiment on September 4^{th}, the region consisted of a reasonably uniform 30% cover of multi-year floes of typical diameter 50 – 80 m. Ice thicknesses could not be determined and we have resorted to taking the floe thickness from the 1978 data, which based on 14 measurements through smooth areas gave 3.1 m (a tenuous assumption but we have no better method). It is worth noting that Overgaard et al. (1983) suggested this value was an underestimate of the true mean thickness, but as we have no way of verifying this we select τ distributed about 3.1 m with a relatively large standard deviation of 0.4 so that 95% of the normally chosen τ are between 2.3 m and 3.9 m. This experiment was conducted in a diffuse MIZ so we expect the experiment to provide a good fit to our scatter model. The ice field also generally consisted of large floes and hence qualify for the large floe requirement given in Section 8.3.

We present the 4^{th} of September 1979 Greenland Sea data and model results in Figure 10.14 and Figure 10.15. Figure 10.14 shows the predicted value from our model with mean $\tau = 3.1$ m as a solid line and the predicted values from the single scatter approximation, given by (9.11), as a dashed line. The figure also shows the experimental data for $C = 0.3$ with $L = 50$ m ('+' data points with error bars) and $L = 80$ m ('$\circ$' data points with error bars). This figure shows the linear scaling of the attenuation coefficient with this property. Figure 10.15 shows the predicted value from our model with mean $\tau = 2$ m (solid line) and mean $\tau = 3.5$ m (dashed line), both with a large standard deviation of 0.4. It is clear from these figures that there is a great deal of uncertainty in the comparison of these experiments with our model, highlighting the importance of accurate and precise details of the ice conditions at the time of the experiment. In Figure 10.14, our model slightly over-predicts the attenuation coefficient, while the approximation theory considerably over-predicts the attenuation coefficient. Interestingly, the results in Wadhams et al. (1988) agree with the experimental data better than the approximation theory presented here does. This might be due to the error in there solution for the single floe scattering producing lower attenuation coefficients than are obtained with the correct single floe scattering as presented here. It is also worth mentioning that there is a range in the data, and in other situations the approximate theory may perform better.

On the 10^{th} of September, the ice-cover was more sparse and the floes were generally larger. This experiment was also conducted in a diffuse MIZ with large floes so we expect the experiment to provide a good fit to our scatter model. Again no record of floe thickness was recorded during this experiment and we use the floe thickness data from 1978 which estimates $\tau = 3.1$ m. Figure 10.16 shows the predicted attenuation coefficient from our model with mean $\tau = 3.1$ m with a large standard deviation of 0.4 (solid line) and its 95% confidence interval (CI) (dotted lines), and the predicted values from the approximation theory (dashed line). The figure also plots the experimental data where we estimate $L = 80$ m and $C = 0.15$. Generally the data and our model are in good agreement. They slightly disagree for small periods where a rollover (a trend of decreasing attenuation as the period becomes smaller) occurs in the field data and for longer periods where our model slightly under-predicts the attenuation coefficient. The approximation theory again over-predicts the attenuation coefficient.

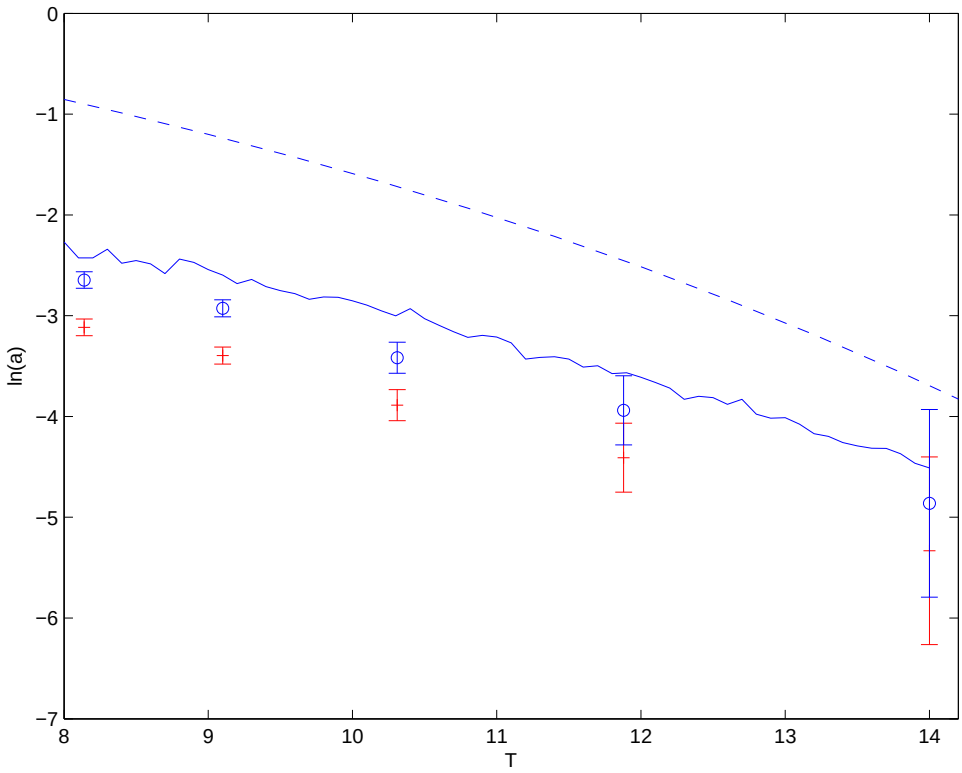

Figure 10.14: a (−) and $\tilde{a}$ (− −) for mean $\tau = 3.1$ m and the 4^{th} September 1979 Greenland Sea experiment, with error bars, for $C = 0.3$ and $L = 50$ m (+) and $L = 80$ m (∘).

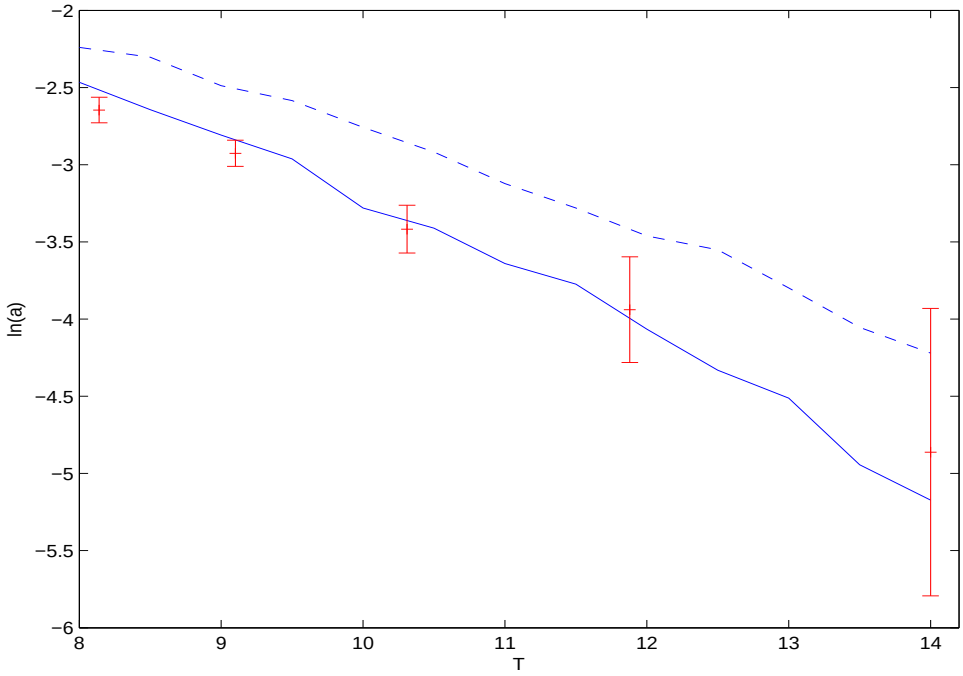

Figure 10.15: a for mean $\tau = 2$ m ($-$) and mean $\tau = 3.5$ m ($-\ -$) and the 4^{th} Sept 1979 Greenland Sea experiment, with error bars, for $L = 65$ m and $C = 0.3$ (+).

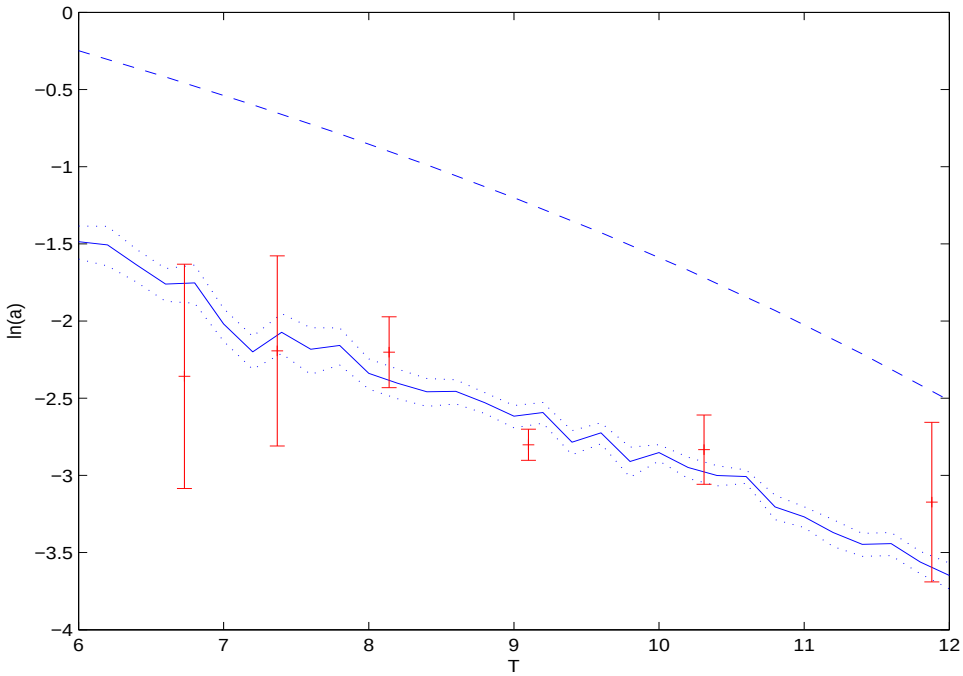

Figure 10.16: a ($-$), its 95% CI ($\cdots$), and $\tilde{a}$ ($-\ -$) for mean $\tau = 3.1$ m, and the 10^{th} Sept 1979 Greenland Sea experiment, with error bars, for $C = 0.15$ and $L = 80$ m (+).

10.3.2 Bering Sea 1979

In March 1979, experiments were performed in the Bering Sea ice margin (Squire and Moore, 1980). On the day of the experiment, the MIZ had 50% sea-ice concentration. Floe diameter increased gradually from 10 m at the ice edge to 40 m at approximately 30 km in. At 30 km, the floe size increased abruptly to more than 100 m in diameter, the typical size thereafter. Two buoys were located in the region of 10 m floe diameters, 3 in the region of 10 – 40 m floe diameters and 2 in the region of 100 m floes. We find $L = 30$ m by taking the average floe lengths. Core samples were taken from floes 10 – 20 m wide and 0.5 m thick. The section of the MIZ where this experiment took place consisted of a mixture of diffuse and compact ice conditions. We therefore expect a reasonable but not perfect comparison between the experimental data and model results.

Figure 10.17 compares the model attenuation coefficients against the experimental attenuation coefficients from the Bering Sea in 1979. Since many of the floes are in fact wider than 10 – 20 m, they are probably thicker than 0.5 m. Hence, the model attenuation coefficients are calculated with the mean $\tau = 1.5$ m (based on the thicknesses of floes from other years in the Bering Sea) with a large standard deviation of 0.4. The experimental attenuation coefficients are plotted for $C = 0.5$ and $L = 30$ m (+) and $L = 100$ m ($\circ$). Here the experimental attenuation coefficients are considerably less than the modelled coefficients. They are however decreasing at a similar rate. At periods between 12 s and 16 s, the experimental data unexpectedly increases. We suspect the increase may be due to an experimental error.

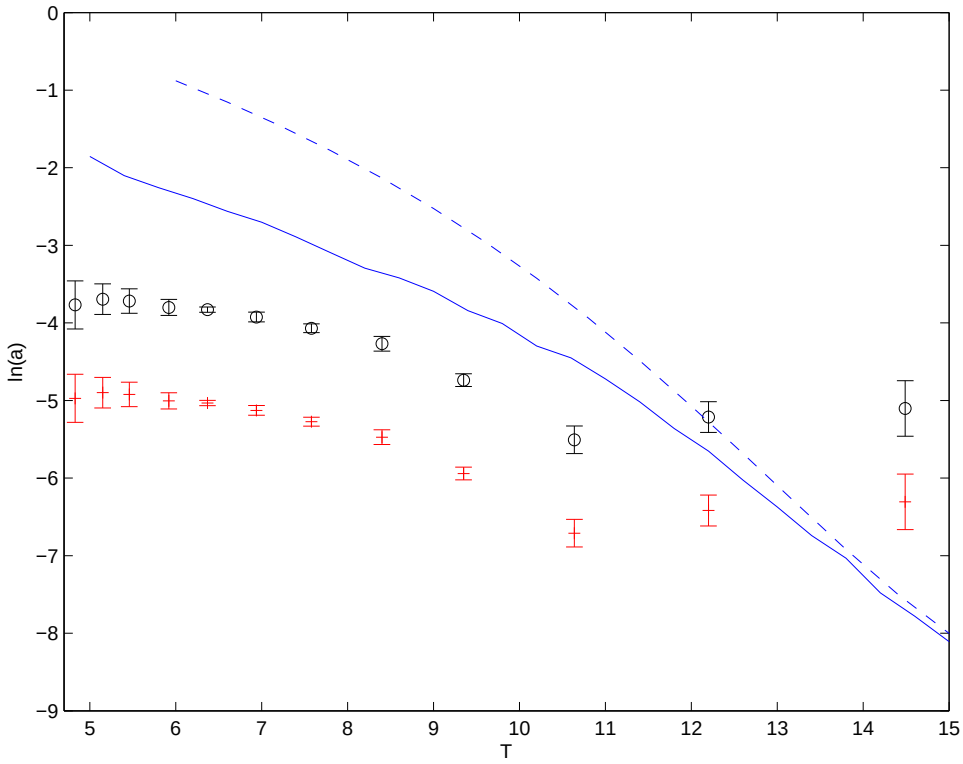

Figure 10.17: a (–) and $\tilde{a}$ (– –) for mean $\tau = 1.5$ m and the 1979 Bering Sea experiment, with error bars, for $C = 0.5$ with $L = 30$ m (+) and $L = 100$ m (∘).

10.3.3 Greenland Sea 1983

On the 26^{th} and 29^{th} July, a helicopter was used to transport a vertical accelerometer to six sites at increasing distance from the ice edge, while a buoy was measuring wave energy at the ice edge. The experiments are reported in Squire et al. (1983). Unfortunately, very little information is provided on the ice conditions at the time of these experiments.

Along the attenuation line on the 26^{th}, the ice-cover changed from compact ice into diffuse ice and the floes visited ranged between 30 m and 80 m. Very little information is provided on floe thickness; it is mentioned that one of the floes that was visited was thick.

To deal with the uncertainty in ice thickness, Figure 10.18 shows the predicted value

from our model with mean $\tau = 4$ $(-)$ with a large standard deviation of 0.5. Figure 10.18 also shows the predicted values from the approximation theory $(--)$. The estimated upper and lower boundaries of the experimental data are plotted using $C = 0.6$ with $L = 30$ m (+ data points with error bars) and $C = 0.4$ with $L = 80$ m ($\circ$ data points with error bars). Our model fits within the expected attenuation coefficient boundaries based on the experimental data. Note however, our model is not predicting the rollover at short periods. The approximation theory over-predicts the attenuation coefficient.

On the 29^{th}, the floes visited ranged between 30 m and 100 m. The freeboard was found to vary between 0.2 m and 0.5 m. We estimate τ by assuming freeboard is 1/10 of its draft (Perrie and Hu, 1997). Therefore we estimate τ is between 2.2 m and 5.5 m. We select mean $\tau = 3.9$ m with a large standard deviation of 0.8, so that 95% of the normally chosen τ's are between 2.3 m and 5.5 m.

Figure 10.19 shows the predicted values from our model $(-)$ and from the approximation theory $(--)$. The estimated upper and lower boundaries of the experimental data are plotted using $C = 0.6$ with $L = 30$ m (+ data points with error bars) and $C = 0.4$ with $L = 100$ m ($\circ$ data points with error bars). The attenuation coefficients are decaying at a much faster rate than is usual and much faster than the models prediction. This may be due to the experimental line (in direction of the incoming swell) being oblique with respect to the ice edge. This implies that any wave refraction occurring at the ice edge would have complicated the results. Although our model can allow for oblique direction of incoming swell, the oblique angle was not reported.

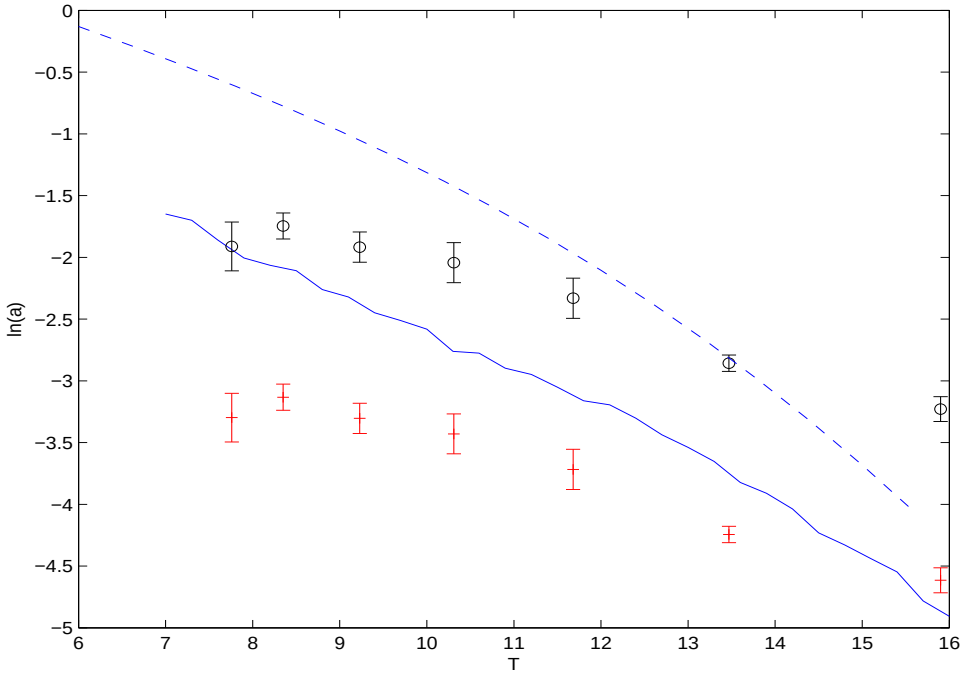

Figure 10.18: a $(-)$ and $\tilde{a}$ $(- \ -)$ for mean $\tau = 4$ m and the 26^{th} July 1983 Greenland Sea experiment, with error bars, for $C = 0.6$, $L = 30$ m (+) and for $C = 0.4$, $L = 80$ m ($\circ$).

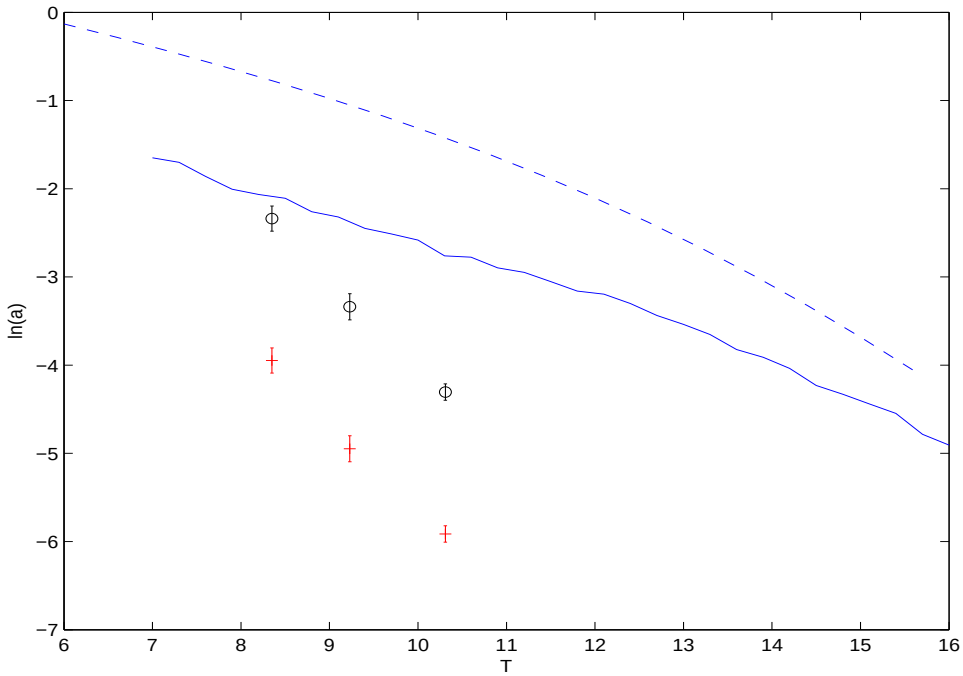

Figure 10.19: a $(-)$ and $\tilde{a}$ $(- \ -)$ for mean $\tau = 3.9$ m $(-)$ and the 29^{th} July 1983 Greenland Sea experiment, with error bars, $C = 0.6$, $L = 30$ m (+) and for $C = 0.4$, $L = 100$ m ($\circ$).

10.3.4 Bering Sea 1983

During February 1983, as part of the MIZEX West study, several experiments took place in the Bering Sea (Wadhams et al., 1988; Squire and Wadhams, 1985). The first set of experiments on the 7^{th} February was intended as an attenuation transect and only three sites were located in a straight line from the ice edge. Although three wave stations are not sufficient for a detailed study of wave decay, the wave energy was continuously monitored using radar transponders accompanied by Seadiscs. Consequently, the data from each site was collected simultaneously. The remaining experiments involved a helicopter hopping from floe to floe. Here, although the data was not simultaneously collected, a large number of wave stations were set up and included sites which were deep into the ice interior.

7^{th} *February*
On the 7^{th} of February, two experiments took place, one 12 hours after the other. The ice conditions during this study consisted of compact floes with short average floe lengths. Hence, we do not expect our model to perfectly fit the experimental data. These experiments were close to the ice edge, where the majority of floe lengths were around 10 m across and the floe thickness ranged between 0.7 m and 1.0 m. Note however, these thicknesses were measured from free board and may not be accurate. We select τ such that it is distributed about a mean of 0.85 m with a standard deviation of 0.2. The floe concentration was greater than 80%.

Figure 10.20 shows the predicted values from our model $(-)$ with mean $\tau = 0.85$ m. As the floe lengths were small in this experiment, we compare our model to the rigid floe model of Perrie and Hu (1996) $(- \ -)$. The first $(+)$ and second $(\circ)$ experimental attenuation coefficients are plotted for $C = 0.8$ and $L = 10$ m. Note that these two experiments took place on the same day with different results, despite the conditions being almost identical.

We find that our model and the Perrie and Hu (1996) model are in close agreement. This is because our model reduces to the rigid body model in the limit of small floes. Our model approximately lies between the two experiments, and it is generally a very good representation of the experimental data. Perrie and Hu (1996)'s model has slightly higher attenuation coefficients, but it represents the rollover in the first experiment very well, while ours does not represent the rollover at all. Note that the mean floe thickness used in Perrie and Hu (1996)'s model was 1.5 m rather than 0.85 m and their floe diameter was 14.5 rather than 10.

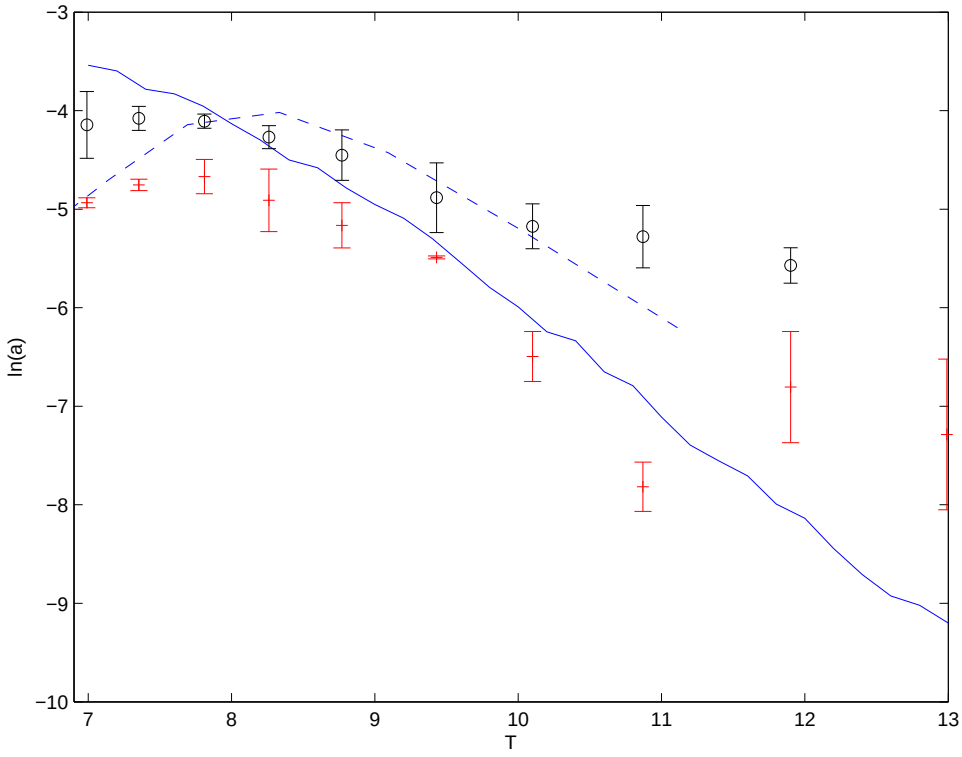

Figure 10.20: a for mean $\tau = 0.85$ m (−), the model of Perrie and Hu (1996) (− −) and the first (+) and second (○) 7^{th} February 1983 Bering Sea experiments, with error bars, for $C = 0.8$ and $L = 10$ m.

20^{th}, 22^{nd} and 26^{th} of February

A detailed account of the the ice conditions at the time of these experiments was not reported in Wadhams et al. (1988). For each experiment, we make estimates of τ, C and L.

The attenuation transect on the 20^{th} comprised of 5 stations, each 5 – 10 km apart and 50 km from the ice edge. It is expected that the data may have large errors due to the small number of sites involved, their proximity and the large drift experienced by the ship. The character of the ice-cover was considerably different from that encountered on 7^{th} February and consisted of large conglomerate floes composed of thick discrete floes. Ice concentrations were low and varied between 6% and 34%. On the 22^{nd}, the attenuation transect comprised of 7 stations, again each 5 – 10 km apart. On the 26^{th}, the attenuation transect composed of 8 stations, each 5 – 20 km apart Note that on the 26^{th}, no measurements of sea state were available near the ice edge as the seadisc was lost in rough seas. We expect that a viscous model would be a more appropriate model for the conglomerate floes and expect disagreement between our scatter model and the experi-

ment. Nevertheless, for all three experiments, we estimate $L = 100$ m, $C = 0.2$ and we select τ such that is distributed about 2 m with a large standard deviation of 0.5.

Figure 10.21 shows that for periods of more than 13 s, both the attenuation coefficients from our model and Perrie and Hu (1996)'s model decay considerably faster than the attenuation coefficients from the experimental results. Note, however, that the experiment includes periods up to 21 s, which is far longer than included in the previous experiments. This discrepancy may be a result of the increased scatter seen in figures 8.9 and 8.10. The increased scatter indicates that, for long periods, the transmitted energy does not as strongly represent an exponentially decaying function. As mentioned earlier, this increased scatter may be a result of increased coherent effects and hence our model for the attenuation coefficient may be improved by increasing the number of simulations. Figure 10.21 plots our model results for both 100 simulations ($-$) and 1000 simulations (x). The increased number of simulations smooth the results, but does not alter the rate of change of the attenuation coefficient. Alternatively, the discrepancy between the experimental data and the models may be a result of the inaccuracy of the instruments at longer periods or may be an indication that the scatter model does not predict wave-attenuation at long periods under these ice conditions.

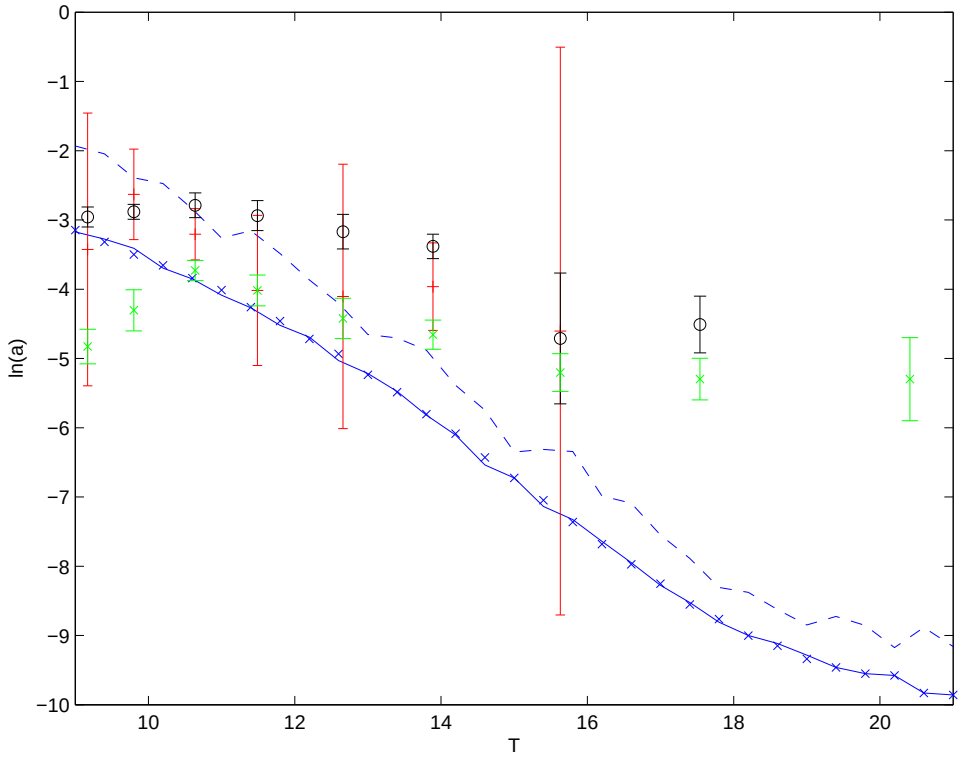

Figure 10.21: a for mean $\tau = 2$ m for 100 simulations (−) and for 1000 simulations (x), the model of Perrie and Hu (1996) (− −) and the 20^{th} (+), 22^{nd} (○) and 26^{th} (x) of February 1983 Bering Sea experiments, with error bars. For each experiment, $C = 0.2$ and $L = 100$ m.

10.3.5 Bellinghausen Sea 2003

The Autosub AUV completed four experiments west of the Antarctic Peninsula in the Bellinghausen Sea during 22^{nd} – 25^{th} March 2003. In water track mode, the Autosub's navigation frame of reference is the water rather than the seabed, hence for some experiments a mean current caused the submarine to drift from the mission plan. Consequently, the line of travel of the sub was not necessarily along the direction of the swell nor at right angles to the ice edge. Also, the attenuation coefficients for wave periods longer than 16 s may be compromised by possible surge response of the vehicle (Hayes et al., 2007). The ice conditions at the time of the experiment were recorded by video and sea ice logs and are summarised in Hayes et al. (2007). Of the four experiments, experiments 323 and 324 produced successful attenuation coefficients. During experiment 321 no records were made as the region was completely under ice at 100 m depth. During experiment 322, no wave-attenuation was recorded, as there was a region of open water 2 km from the ice edge. The AUV was not able to sense the motion of the open water surface due to the set up of the acoustic current meter. Note that the AUV, with a slightly altered

experimental design, would be capable of collecting data in regions consisting of both ice and open water. Overall, we do not expect our model to perform well against this data set as the ice is very compact and the floe lengths are small.

Experiment 323; 24^{th} *March* During experiment 323, ice-coverage was 100%; 60% first-year ice floes with diameter less than 20 m and 0.5 – 0.75 m thick, and 40% was brash ice 0.5 m thick. To simulate, we select $C = 0.6$, τ to be distributed about 0.625 with a standard deviation of 0.1 m and $L = 20$ m.

Experiment 324; 25th March On March 25, experiment 324 sampled roughly 10 km^2 of sea-ice and traversed the ice edge twice (on entering and exiting). Ice conditions were recorded from the ship at four locations several kilometres into the ice. The sea-ice was reported to consist of 100% ice-coverage, 20% brash and 80% multi-year or first-year ice of thickness 1.5 – 2 m. We therefore select $C = 0.8$ and τ such that it is distributed about 1.75 m and select a standard deviation of 0.1 m. Floe diameter was recorded to be less than 20 m, we select $L = 20$.

We present the Autosub AUV data in Figures 10.22 and 10.23. There is little agreement with our model for these ice conditions. The experimental results for short periods are of similar order of magnitude, but our model is clearly under-predicting the attenuation coefficients at long periods. Even the possible errors in the experimental data for long periods cannot account for the predicted fast attenuation rates. This is a further indication that physical factors other than wave scatter may be involved in wave-attenuation through compact ice.

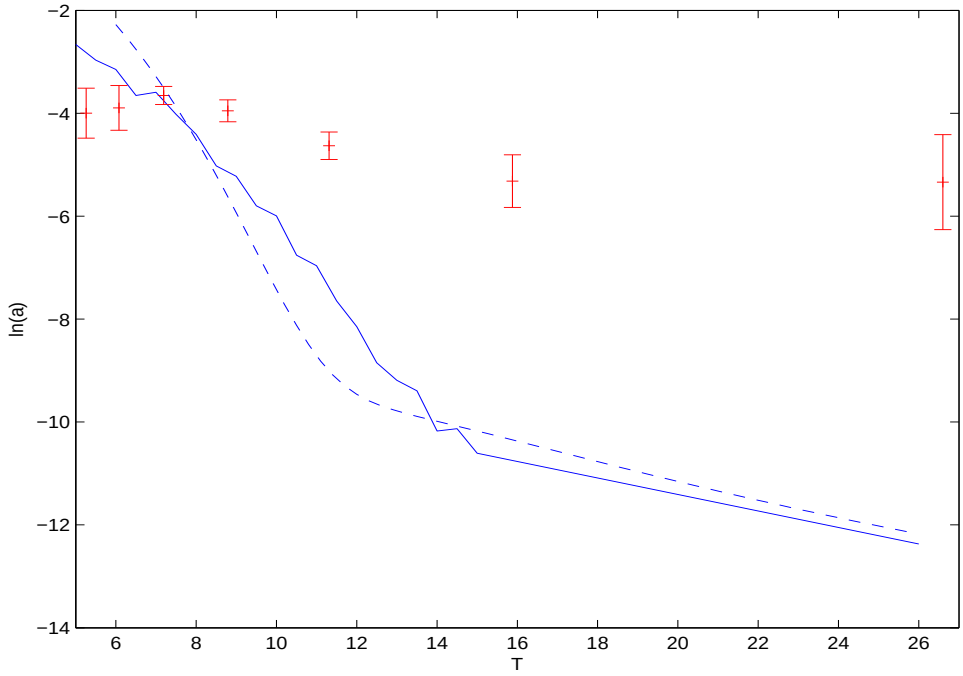

Figure 10.22: a (−) and $\tilde{a}$ (− −) with mean $\tau = 0.625$ m and the Bellinghausen Sea experiment 323, with error bars, for $C = 0.6$ and $L = 20$ m (+).

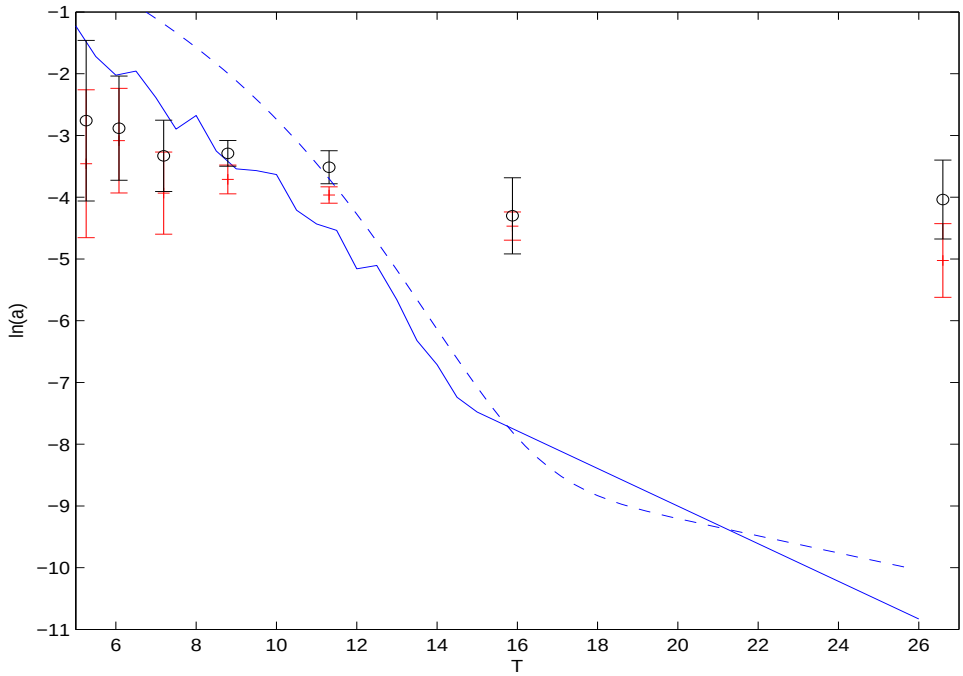

Figure 10.23: a (−) and $\tilde{a}$ (− −) with mean $\tau = 1.75$ m and the Bellinghausen Sea experiment 324, with error bars, for $C = 0.8$ and $L = 20$ m on entering (+) and exiting the ice (○).

10.3.6 Summary / Discussion

We use scatter theory to model a MIZ consisting of mainly diffuse ice. In highly concentrated ice fields, floe collisions are more likely to occur so that the pack behaves either as a collection of very large floes or as a single entity. The floes can no longer surge in response to the waves and wave-attenuation may be less associated with wave scatter and occurring more significantly in the form of viscous losses from the boundary layer under the ice (Squire et al., 1995). Our model also requires that the wave length is always 3 times the floe length so E remains independent of floe length (Section 8.3). We compare our model to some experimental data sets which do, and some experimental data sets which do not, fit these requirements. This is mainly due to the limited amount of experimental data available. We use these varied data sets to help identify the limits of our scatter model.

For the experiments carried out in diffuse ice with large floes, our model performs well (Figure 10.14 and 10.16). The 1979 Bering Sea and 1983 Greenland Sea experiments were carried out in a MIZ consisting of a mixture of diffuse and compact ice. Our model compares reasonably well to the experiments from the Bering Sea in 1979 (Figure 10.17) and from the the first experiment from the Greenland Sea in 1983 (Figure 10.18). Our model does not agree with the second experiment from the Greenland Sea in 1983 (Figure 10.19). Note that during this experiment, the data was not collected perpendicular to the direction of incoming swell.

The experiments carried out in the Bering Sea in 1983 between the 20^{th} – 26^{th} of February consisted of large conglomerate floes composed of thick discrete floes. Our model does not perform well in this case. This may be due to the fact that the ice zone consisted of conglomerate floes where wave-attenuation may be less significantly associated with wave scatter and occurring more significantly in the form of viscous losses. Also, for very large floes, extra losses can occur from reflections from pressure ridges or as creep hysteresis losses due to flexure of the ice sheet. Note that the discrepancy between the model and the experiment increases with increasing period. It is possible that the instruments are inaccurate for long periods or that scatter theory is less significant at long periods.

Three experiments were carried out in compact ice conditions with small floes. Of the three, we found surprising agreement with the 7^{th} February 1983 Bering Sea experiments (Figure 10.20). This may be due to our model reducing to the rigid body model in the limit of small floes. It is also possible that the small ice floes were close but not interacting and hence the scatter model still applied. Our model does not agree with the other two experiments carried out in compact ice (Figure 10.22 and 10.23). In this case, physical factors other than wave scatter may have contributed to the wave-attenuation.

For example, the increased attenuation loss may be due to viscous losses or the imperfect elasticity of sea-ice. Factors which will effect the anelastic properties of sea-ice include its brine-volume and crystal structure. It may be necessary to add an extra viscous or anelastic term which accentuates the attenuation. Unfortunately, however, these terms can only be determined through measurements.

Overall, we found successful agreement between our model and the experiments most applicable to our model i.e. experiments in diffuse ice with large floes. Note however, that our model never predicts the roll-over often found at short periods. Surprisingly we found that generally, even for the experiments less applicable to our model, there is some agreement between the model and the experimental data for short to medium periods. However, as the ice concentration increases and floe length decreases, the under-prediction of the attenuation coefficient increases and this is especially apparent at long periods. Note that without further experimental data, it is difficult to judge how the model would perform against experiments in diffuse ice with large floes at long periods (approximately greater than 14 seconds). It would be very profitable to compare our model to more data sets, where the details of the floe characteristics at the time of the experiments are more precise. We are, however, overall pleased with our results, which suggest that a scattering model is generally a good approximation for ice conditions consisting of large floes in diffuse ice for wave periods between 6 and 15 seconds. We also conclude that for small floe sizes and high ice concentrations, wave attenuation is not primarily due to wave scattering.

11

Summary and Conclusions

This research contributes to the theoretical and analytical study of the interaction of water waves with large floating structures. The scattering of small amplitude waves, which are obliquely incident on a set of floating elastic plates occupying the entire water surface, is considered. The plates float on a body of water of arbitrary depth and each plate is uniquely defined. The problem is solved two-dimensionally, assuming invariance in one horizontal direction. The problem is formulated by imposing boundary conditions on the eigenfunction expansion of Laplace's equation. The wave modes are generated by solving the dispersion equation, which is derived from these boundary conditions. A set of transmission and reflection coefficients is defined, which is found by matching at each plate boundary, where the number of matching conditions provides fewer equations than unknowns. The auxiliary equations arise from by the the plate boundary conditions. The problem is solved for a variety of edge conditions including: free, clamped, sliding, springed and hinged. The problem is also solved using a GFM which also solves for a set of plates, but requires that each plate is identical. This method is included as it is a useful tool to verify the results of the MEEM. The integrity of the solutions is further verified by ensuring the systems are in energy balance. The solutions and convergence of the MEEM are tested against the GFM and Meylan and Squire (1994)'s finite-floe model, where the solutions agree exactly and the convergence of the methods are almost identical. For each method, approximately 20 modes are required for the solution to converge to an accuracy

of two decimal places.

Our frozen seas play an important role in sustaining our climate and it is therefore relevant to understand the processes involved in its formation and de-formation. Wave energy has proven to penetrate surprisingly deep into an ice field and play a major role in the breakup of sea-ice. The main focus of this research was to develop our understanding of wave propagation in ice-covered seas. The MEEM is used to simulate wave–ice interaction in the Marginal Ice Zone (MIZ). The only physics included is due to the effects of an elastic plate on the water surface and all non-linear effects are neglected as well as floe collisions and viscosity. In removing the resonance effects, by averaging over a distribution of floe lengths, the model predicts that the transmitted energy, E, is independent of floe length, provided the mean floe length is above a critical value which will occur roughly when the wavelength is more than three times the floe length. The model predicts an exponential decay of wave energy with distance of propagation through the MIZ. This result is particularly significant because it agrees with the experimental findings. The attenuation coefficient, provided the floes are sufficiently large, is a function of number of floes and is independent of the average floe length. The results have been summarised in a graph with the attenuation coefficient expressed as a function of period for various floe thicknesses. We also provide an estimate of the attenuation coefficient using an approximation theory. We find the approximation approximately agrees with the model. The attenuation coefficients are used to model the strain in the ice and its consequent floe breakup. The results suggest that the model is under-predicting the attenuation rate and physics other than wave scatter may be relevant.

The displacements of the MEEM are compared against a series of laboratory experiments performed in a two-dimensional wave-tank. Overall the agreement between the theory and experiment is good. We believe this is strong confirmation that our theory is correct for plates of uniform thickness. Differences that do occur may be explained by experimental error such as the reflected wave not being fully dampened by the wave buoy at the end of the flume or alternatively by a measurement error such as the calculation of Young's modulus.

The attenuation model results are compared against field experiment results. Previous model and experimental comparisons have only been achieved by applying approximation theories or by including a tuning parameter in the model. The attenuation model results are compared against a series of field experiments carried out in the Arctic seas by the Scott Polar Research Institute and against a set of experiments carried out off the West

Antarctic Peninsula. We find successful agreement between our wave attenuation model and the experiments most applicable to our model. For highly concentrated ice with short floes, we suggest that wave attenuation is not primarily due to wave scattering. Other factors that may be involved include viscous losses from the boundary layer under the ice, reflections from pressure ridges or losses due to the anelasticity of sea-ice. Overall, we conclude that the model is applicable to large floes in a diffuse ice field, for short to medium wave periods (6 to 15 seconds). Further experiments are required to make any further conclusions.

Bibliography

Balmforth, N. and Craster, R. (1999). Ocean waves and ice sheets. *J. Fluid Mech.*, 395:89–124.

Barrett, M. D. and Squire, V. A. (1996). Ice-coupled wave propagation across an abrupt change in ice rigidity, density, or thickness. *J. Geophys. Res.*, 101(C9):20825–20832.

Bennetts, L. G., Biggs, N. R. T., and Porter, D. (2007). A multi-mode approximation to wave scattering by ice sheets of varying thickness. *J. Fluid Mech.*, 579:413–443.

Billingham, J. and King, A. C. (2000). *Wave Motion*. Cambridge University Press.

Bjørgo, E., Johannessen, O. M., and Miles, M. W. (1997). Analysis of merged SMMR–SSMI time series of Arctic and Antarctic sea ice parameters. *Geophys. Res. Lett.*, 24:413–416.

Bukatov, A. E. and Bukatov, A. A. (1999). Mass transfer by nonlinear waves in a basin with floating broken ice. *J. Phys. Oceanogr.*, 10(5):393–399.

Chakrabarti, A. (2000). On the solution of the problem of scattering of surface-water waves by the edge of an ice cover. *Proc. R. Soc. Lon. Ser-A*, 456:1087–1099.

Chou, T. (1998). Band structure of surface flexural-gravity waves along periodic interfaces. *J. Fluid Mech.*, 369:333–350.

Chung, H. (2002). *Mathematical Studies of Wave Propagation in Sea-Ice*. PhD thesis, University of Auckland, Auckland, New Zeland.

Chung, H. and Fox, C. (2002). Calculation of wave–ice interaction using the Wiener–Hopf technique. *New Zealand Journal of Mathematics*, 31:1–18.

Chung, H. and Linton, C. M. (2005). Reflection and transmission of waves across a gap between two semi-infinite elastic plates on water. *Q. J. Mech. Appl. Math.*, 58(1):1–15.

Comiso, J. C., Parkinson, C. L., Gersten, R., and Stock, L. (2008). Accelerated decline in the Arctic sea ice cover. *Geophys. Res. Lett.*, 35(1).

Dixon, T. W. and Squire, V. A. (2001). Energy transport in the Marginal Ice Zone. *J. Geophys. Res.*, 106(C9):19917–19927.

Evans, D. and Davies, T. (1968). Wave–ice interaction. Technical Report 1313, Stevens Inst. of Technology.

Evans, D. and Porter, R. (2003). Wave scattering by narrow cracks in ice sheets floating on water of finite depth. *J. Fluid Mech.*, 484:143–165.

Fox, C. and Squire, V. A. (1990). Reflexion and transmission characteristics at the edge of shore fast sea ice. *J. Geophys. Res.*, 95(C7):11629–11639.

Fox, C. and Squire, V. A. (1991). Strain in shore fast ice due to incoming ocean waves and swell. *J. Geophys. Res.*, 96(C3):4531–4547.

Fox, C. and Squire, V. A. (1994). On the oblique reflexion and transmission of ocean waves at shore fast sea ice. *Philos. T. Roy. Soc. A*, 347(1682):185–218.

Gayen, R., Mandel, B. N., and Chakrabarti, A. (2007). Water wave diffraction by a surface strip. *J. Eng. Math.*, 53(1):21–37.

Goodman, D. J., Wadhams, P., and Squire, V. A. (1980). The flexural response of a tabular ice island to ocean swell. *Ann. Glaciol.*, 1:23–27.

Greenhill, A. (1887). Wave motion in hydrodynamics. *Am. J. Math.*, 9:62–112.

Hasselmann, K. (1973). *Measurements of wind-wave growth and swell decay during the Joint North Sea Wave Project (JONSWAP).* Deutsches Hydrographisches Institute.

Hayes, D. R., Jenkins, A., and McPhail, S. (2007). Autonomous underwater vehicle measurements of surface wave decay and directional spectra in the Marginal Ice Zone. *J. Phys. Oceanogr.*, 37(1):71–83.

Hermans, A. J. (2003). Interaction of free-surface waves with a floating dock. *J. Eng. Math.*, 45:39–53.

Hermans, A. J. (2004). Interaction of free-surface waves with floating flexible strips. *J. Eng. Math.*, 49:133–147.

Isaacson, M. (1982). Fixed and floating axisymmetric structures in waves. *J. Waterw. Port Coast. Ocean Div.*, 108(2):180–199.

Johnson, R. S. (1997). *A Modern Introduction to the Mathematical Theory of Water Waves*. Cambride Texts in Applied Mathematics. Cambridge University Press.

Karmakar, D. and Sahoo, T. (2005). Scattering of waves by articulated floating elastic plates in water of infinite depth. *Mar. Struct.*, 18:451–471.

Kashiwagi, M. (2000). Research on hydroelastic response of vlfs: Recent progress and future work. *Int. J. Offshore Polar*, 10(2):81–90.

Keller, J. B. and Weitz, M. (1953). Reflection and transmission coefficients for waves entering or leaving an icefield. *Comm. Pure and App. Math.*, 6(3):415–417.

Kohout, A. and Meylan, M. H. (2006). A model for wave scattering in the Marginal Ice Zone based on a two-dimensional floating elastic plate solution. *Ann. Glaciol.*, 44:101–107.

Kohout, A., Meylan, M. H., Sakai, S., Hanai, K., Leman, P., and Brossard, D. (2007). Linear water wave propagation through multiple floating elastic plates of variable properties. *J. Fluid Struct.*, 23(4):649–663.

Kohout, A. L. and Meylan, M. H. (2008a). Articulated plates. Submitted to Marine Structures.

Kohout, A. L. and Meylan, M. H. (2008b). A model for wave scattering in the Marginal Ice Zone based on a two-dimensional floating elastic plate solution. *J. Geophys. Res.*, 113.

Kouzov, D. (1963). Diffraction of a plane hydro-elastic wave on the boundary of two elastic plates (in russian). *Prikl. Mat. Mekh.*, 27:541–546.

Langhorne, P. J., Squire, V. A., Fox, C., and Haskell, T. G. (1998). Break-up of sea ice by ocean waves. *Ann. Glaciol.*, 27:438–442.

Langhorne, P. J., Squire, V. A., Fox, C., and Haskell, T. G. (2001). Lifetime estimation for a land-fast ice sheet subjected to ocean swell. *Ann. Glaciol.*, 33:333–338.

Larouche, P. and Cariou, C. (1992). Directional wave spectra estimation in a marginal ice zone using linear prediction. *J. Phys. Oceanogr.*, 22:196–206.

Lee, C.-H. and Newman, J. N. (2000). An assessment of hydroelasticity for very large hinged vessels. *J. Fluid Struct.*, 14:957–70.

Linton, C. M. and McIver, P. (2001). *Handbook of Mathematical Techniques for Wave / Structure Interactions*. Chapman & Hall /CRC, Boca Raton, Florida. 304 pp.

Liu, A. K., Holt, B., and Vachon, P. W. (1991). Wave propagation in the Marginal Ice Zone: Model predictions and comparisons with buoy and synthetic aperture radar data. *J. Geophys. Res.*, 96(C3):4605–4621.

Liu, A. K. and Mollo-Christensen, E. (1988). Wave propagation in a solid ice pack. *J. Phys. Oceanogr.*, 18:1702–1712.

Liu, X. and Sakai, S. (2002). Time domain analysis on the dynamic response of a flexible floating structure to waves. *J. Eng. Mech.*, 128(1):48–56.

Marchenko, A. V. (1996). Swell wave propagation in an inhomogeneous ice sheet. *Fluid Dynamics*, 31(5):761–767.

Marchenko, A. V. and Voliak, K. I. (1997). Surface wave propagation in shallow water beneath an inhomogeneous ice cover. *J. Phys. Oceanogr.*, 27:1602–1613.

Masson, D. and LeBlond, P. (1989). Spectral evolution of wind-generated surface gravity waves in a dispersed ice field. *J. Fluid Mech.*, 202:111–136.

McKenna, R. F. and Crocker, G. B. (1990). Wave energy and floe collisions in Marginal Ice Zones. In Murthy, T. K. S., Paren, J. G., Sackinger, W. M., and Wadhams, P., editors, *Ice Technology for Polar Operations, Proc. 2nd Int. Conf. on Ice Tech*, pages 33–45. Boston.

Meylan, M. H. (1994). *The behaviour of sea ice in ocean waves*. PhD thesis, University of Otago, New Zealand.

Meylan, M. H. (2002). The wave response of ice floes of arbitrary geometry. *J. Geophys. Res.*, 107(C6). Art. No. 3005.

Meylan, M. H. and Masson, D. (2006). A linear Boltzmann equation to model wave scattering in the marginal ice zone. *Ocean Model.*, 11:417–427.

Meylan, M. H. and Squire, V. A. (1993). Finite floe reflection and transmission coefficients from a semi-infinite model. *J. Geophys. Res.*, 98(C7):12537–12542.

Meylan, M. H. and Squire, V. A. (1994). The response of ice floes to ocean waves. *J. Geophys. Res.*, 99(C1):891–900.

Meylan, M. H. and Squire, V. A. (1996). Response of a circular ice floe to ocean waves. *J. Geophys. Res.*, 101(C4):8869–8884.

Meylan, M. H., Squire, V. A., and Fox, C. (1997). Towards realism in modeling ocean wave behavior in Marginal Ice Zones. *J. Geophys. Res.*, 102(C10):22981–22991.

Newman, J. N. (2005). Efficient hydryodynamic analysis of very large floating structures. *Mar. Struct.*, 18:169–180.

Ogasawara, T. and Sakai, S. (2006). Numerical analysis of the characteristics of waves propagating in arbitrary ice-covered sea. *Ann. Glaciol.*, 44:95–100.

Overgaard, S., Wadhams, P., and Lepparanta, M. (1983). Ice properties in the Greenland and Barents seas during summer. *J. Glaciol.*, 29(101):142–164.

Papoulis, A. (1984). *Probability, Random Variables, and Stochastic Processes*. McGraw-Hill, 2nd edition.

Perrie, W. and Hu, Y. (1996). Air–ice–ocean momentum exchange. Part 1:Energy transfer between waves and ice floes. *J. Phys. Oceanogr.*, 26:1705–1720.

Perrie, W. and Hu, Y. (1997). Air–ice–ocean momentum exchange. Part 2: Ice drift. *J. Phys. Oceanogr.*, 27:1976–1996.

Peter, M. A. and Meylan, M. H. (2004). The eigenfunction expansion of the infinite depth free surface green function in three dimensions. *Wave Motion*, 40(1):1–11.

Peter, M. A. and Meylan, M. H. (2007). Water-wave scattering by a periodic array of arbitrary bodies. *J. Fluid Mech.*, 575:473–494.

Peter, M. A., Meylan, M. H., and Chung, H. (2004). Wave scattering by a circular elastic plate in water of finite depth: a closed form solution. *IJOPE*, 14(2):81–85.

Peter, M. A., Meylan, M. H., and Linton, C. M. (2006). Water-wave scattering by a periodic array of arbitrary bodies. *J. Fluid Mech.*, 548:237–256.

Phillips, O. M. (1977). *The Dynamics of the Upper Ocean*. Cambridge University Press, New York, 2nd edition.

Pierson, W. J. and Moskowitz, L. (1964). A proposed spectral form for full-developed wind sea based on the similarity law of S. A. Kitaigorodoskii. *J. Geophys. Res.*, 69:5202.

Porter, D. and Porter, R. (2004). Approximations to wave scattering by an ice sheet of variable thickness over undulating bed topography. *J. Fluid Mech.*, 509:145–179.

Porter, R. and Evans, D. (2006). Scattering of flexural waves by multiple narrow cracks in ice sheets floating on water. *Wave Motion*, 43(5):425–443.

Porter, R. and Evans, D. V. (2005). Embedded Rayleigh-Bloch surface waves along periodic rectangular arrays. *Wave Motion*, 43:29–50.

Robin, G. Q. (1963). Wave propagation through fields of pack ice. *Philos. Tr. R. Soc. S-A*, 255(1057):313–339.

Roethlisberger, H. (1972). Surface waves and waves in thin floating ice. *Cold Regions Research and Engineering Laboratory Monographs*, pages 105–109.

Ruddiman, W. F. (2001). *Earth's Climate: Past and Future*. W. H. Freeman and Sons, New York.

Sakai, S. and Hanai, K. (2002). Empirical formula of dispersion relation of waves in sea ice. In *Ice in the environment: Proceedings of the 16th IAHR International Symposium on Ice*, pages 327–335.

Schulz-Stellenfleth, J. and Lehner, S. (2002). Spaceborne synthetic aperature radar observations of ocean waves traveling into sea ice. *J. Geophys. Res.*, 107:3106.

Shen, H., Hibler, W., and Leppäranta, M. (1998). The role of floe collisons in sea ice rheology. *J. Geophys. Res.*, 92:7085–96.

Shen, H. H. and Squire, V. A. (1998). Wave damping in compact pancake ice fields due to interactions between pancakes. *Antarctic Research Series: Antarctic Sea Ice: Physical Processes, Interactions and variability*, 74:325–341.

Smetacek, V. and Nicol, S. (2005). Polar ocean ecosystems in a changing world. *Nature*, 437(doi:10.1038/nature04161).

Squire, V. and Moore, S. C. (1980). Direct measurement of the attentuation of ocean waves by pack ice. *Nature*, 283(5745):365 – 368.

Squire, V. and Wadhams, P. (1985). Some wave attenuation results from MIZEX-West. Special Report SR 85-06, Cold Regions Research and Engineering Laboratory.

Squire, V., Wadhams, P., Cowan, A. M., O'Farrell, S., and Weintraub, R. (1983). MIZEX 83 data summary. SPRI Technical Report 83-1, Scott Polar Research Institution.

Squire, V. A. (1993). The breakup of shore-fast sea ice. *Cold Reg. Sci. Technol.*, 21:211–218.

Squire, V. A. (2007). Of ocean waves and sea-ice revisited. *Cold Reg. Sci. Technol.*, 49:110–133.

Squire, V. A. and Dixon, A. W. (2000). An analytic model for wave propagation across a crack in an ice sheet. *Int. J. Offshore Polar*, 10:173–176.

Squire, V. A. and Dixon, A. W. (2001). How a region of cracked sea ice affects ice-coupled wave propagation. *Ann. Glaciol.*, 33:327–332.

Squire, V. A., Dugan, J. P., Wadhams, P., Rottier, P. J., and Liu, A. J. (1995). Of ocean waves and sea ice. *Annu. Rev. Fluid Mech.*, 27:115–168.

Squire, V. A. and Martin, S. (1980). A field study of the physical properties, response to swell, and subsequent fracture of a single ice floe in the winter Bering sea. Univ. Wash. Sci. Rep. 18, Dept. Atmos. Sci. and Oceanogr.

Stoker, J. J. (1957). *Water Waves: The Mathematical Theory with Applications*. Interscience.

Tkacheva, L. (2001). Surface wave diffraction on a floating elastic plate. *Fluid Dynamics*, 36(5):776–789.

Ursell, F. (1947). The effect of a fixed vertical barrier on surface waves in deep water. *Proc. Camb. Phil. Soc.*, 43:374–382.

Vaughan, G. L., Williams, T. D., and Squire, V. A. (2007). Perfect transmission and asymptotic solutions for reflection of ice-coupled waves by inhomogeneities. *Wave Motion*, 44(5):371–384.

Wadhams, P. (1972). Measurement of wave attenuation in pack ice by inverted echo sounding. In Karlsson, T., editor, *Sea Ice. Proceedings of an International Conference*, pages 255–260. National Research Council, Rejkjavik, Iceland.

Wadhams, P. (1975). Airborne laser profiling of swell in an open ice field. *J. Geophys. Res.*, 80:4520–4528.

Wadhams, P. (1978). Wave decay in the marginal ice zone measured from submarine. *Deep-Sea Res.*, 25:23–40.

Wadhams, P. (1979). Field experiments on wave–ice interaction in the Labrador and East Greenland currents, 1978. *Polar Record*, 19(121):373–379.

Wadhams, P. (1986). The seasonal ice zone. In Untersteiner, N., editor, *The Geophysics of Sea Ice*, pages 825–991. Plenum New York.

Wadhams, P. (2000). *Ice in the Ocean*. Gordon and Breach Science.

Wadhams, P., Parmiggiani, F. E., and de Carolis, G. (2002). The use of SAR to measure ocean wave dispersion in frazil-pancake icefields. *J. Phys. Oceanogr.*, 32(6):1721–1746.

Wadhams, P., Parmiggiani, F. E., de Carolis, G., Desiderio, D., and Doble, M. J. (2004). SAR imaging of wave dispersion in Antarctic pancake ice and its use in measuring ice thickness. *Geophys. Res. Lett.*, page 31.

Wadhams, P., Squire, V. A., Ewing, J. A., and Pascal, R. W. (1986). The effect of Marginal Ice Zone on the directional wave spectrum of the ocean. *J. Phys. Oceanogr.*, 16:358–376.

Wadhams, P., Squire, V. A., Goodman, D. J., Cowan, A. M., and Moore, S. C. (1988). The attenuation rates of ocean waves in the marginal ice zone. *J. Geophys. Res.*, 93(C6):6799 – 6818.

Wang, C. D., Meylan, M. H., and Porter, R. (2007). The linear-wave response of a periodic array of floating elastic plates. *J. of Engineering Maths.*, 57(1):23–40.

Watanabe, E., Utsunomiya, T., and Wang, C. (2004). Hydroelastic analysis of pontoon-type VLFS: A literature survey. *Eng. Struct.*, 26(2):245–256.

Weber, J. E. (1987). Wave attenuation and wave drift in the Marginal Ice Zone. *J. Phys. Oceanogr.*, 17:2351–2361.

Williams, T. D. (2005). *Reflections on Ice: The Scattering of Flexural-Gravity Waves by Irregularitiies in Arctic and Antarctic Ice Sheets*. PhD thesis, University of Otago, Dunedin, New Zealand.

Williams, T. D. and Squire, V. A. (2002). Wave propagation across an oblique crack in an ice sheet. *Int. J. Offshore Polar*, 12:157–162.

Williams, T. D. and Squire, V. A. (2004). Oblique scattering of plane flexural-gravity waves by heterogeneities in sea-ice. *Proc. R. Soc. Lon. Ser-A*, 460(2052):3469–3497.

Williams, T. D. and Squire, V. A. (2006). Scattering of flexural-gravity waves at the boundaries between three floating sheets with applications. *J. Fluid Mech.*, 569:113–140.

Xia, D., Kim, J. W., and Ertekin, R. C. (2000). On the hyroelastic behaviour of two-dimensional articulated plates. *Mar. Struct.*, 13:261–278.

A

The Energy Balance Equation

Based on the method used in Evans and Davies (1968), a check can be made to ensure the solutions of the floating plate problem are in energy balance. This is simply a condition that the incident energy is equal to the sum of the radiated energy. When the first and final plates have different properties, the energy balance equation is derived by applying Green's theorem to ϕ and its conjugate (Evans and Davies, 1968). We set up the problem as given in Figure A.1

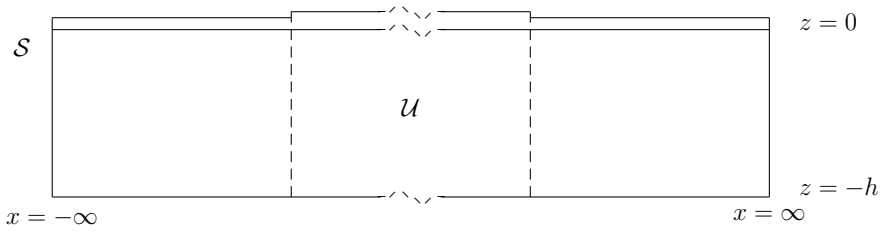

Figure A.1: A diagram depicting the area $\mathcal{U}$ which is bounded by the rectangle $\mathcal{S}$. The rectangle $\mathcal{S}$ is bounded by $-h \leq z \leq 0$ and $-\infty \leq x \leq \infty$.

Applying Green's theorem to ϕ and its conjugate ϕ^* gives

$$\int\int_{\mathcal{U}}(\phi\nabla^2\phi^* - \phi^*\nabla^2\phi)dxdz = \int_{\mathcal{S}}(\phi\frac{\partial\phi^*}{\partial n} - \phi^*\frac{\partial\phi}{\partial n})dl, \tag{A.1}$$

where n denotes the outward plane normal to the boundary and l denotes the plane parallel to the boundary. As ϕ and ϕ^* satisfy (3.24), the left hand side of (A.1) vanishes so that (A.1) reduces to

$$\Im\int_{\mathcal{S}}\phi\frac{\partial\phi^*}{\partial n}dl = 0, \tag{A.2}$$

Expanding gives

$$\xi_1 + \xi_2 + \xi_3 = 0, \tag{A.3}$$

where

$$\xi_1 = \Im\int_{-\infty}^{\infty}(\phi\frac{\partial\phi^*}{\partial z})\big|_{z=0}dx, \tag{A.4}$$

$$\xi_2 = \Im\int_{-h}^{0}(\phi\frac{\partial\phi^*}{\partial x})\big|_{x=\infty}dz, \tag{A.5}$$

and

$$\xi_3 = -\Im\int_{-h}^{0}(\phi\frac{\partial\phi^*}{\partial x})\big|_{x=-\infty}dz = 0, \tag{A.6}$$

where $\Im$ denotes the imaginary part.

Expanding ξ_1

Near $x = -\infty$, we approximate ϕ by

$$\phi \approx e^{-\kappa_1(0)(x-r_1)}\frac{\cos\left(k_1(0)(z+h)\right)}{\cos\left(k_1(0)h\right)} + R_1(0)e^{\kappa_1(0)(x-r_1)}\frac{\cos\left(k_1(0)(z+h)\right)}{\cos\left(k_1(0)h\right)}. \tag{A.7}$$

To simplify the derivation, we re-express (A.7) as

$$\phi \approx \left(e^{-i\kappa_1^I(x-r_1)} + R_1(0)e^{i\kappa_1^I(x-r_1)}\right)\frac{\cosh\left(k_1^I(z+h)\right)}{\cosh\left(k_1^Ih\right)}, \tag{A.8}$$

where $k_1^I = -\Im k_1(0)$ and $\kappa_1^I = -\Im\kappa_1(0)$, so that

$$\frac{\partial\phi}{\partial x} \approx \left(-i\kappa_1^Ie^{-i\kappa_1^I(x-r_1)} + i\kappa_1^IR_1(0)e^{i\kappa_1^I(x-r_1)}\right)\frac{\cosh\left(k_1^I(z+h)\right)}{\cosh\left(k_1^Ih\right)}. \tag{A.9}$$

Therefore,

$$\begin{aligned}
\xi_1 = \; & \Im \int_{-h}^{0} \Big[\Big(e^{-i\kappa_1^I (x-r_1)} + R_1(0) e^{i\kappa_1^I (x-r_1)} \Big) \\
& \qquad \Big(i\kappa_1^I e^{i\kappa_1^I (x-r_1)} - i\kappa_1^I R_1(0)^* e^{-i\kappa_1^I (x-r_1)} \Big) \\
& \qquad \left(\frac{\cosh^2 \left(k_1^I (z+h) \right)}{\cosh^2 \left(k_1^I h \right)} \right) \Big] \, dz, \\
= \; & \Im \left[\frac{i\kappa_1^I \left(1 - |R_1(0)|^2 \right)}{2 \cosh^2 \left(k_1^I h \right)} \int_{-h}^{0} \Big(\cosh \left(2k_1^I (z+h) \right) + 1 \Big) \, dz \right], \\
= \; & \Im \left[\frac{i\kappa_1^I \left(1 - |R_1(0)|^2 \right)}{2 \cosh^2 \left(k_1^I h \right)} \left[\frac{1}{2k_1^I} \sinh \left(2k_1^I (z+h) \right) + z \right]_{-h}^{0} \right], \\
= \; & \frac{\kappa_1^I \left(1 - |R_1(0)|^2 \right)}{2 \cosh^2 \left(k_1^I h \right)} \left(\frac{1}{2k_1^I} \sinh \left(2k_1^I h \right) \right) + h \Big), \\
= \; & \frac{\kappa_1^I \left(1 - |R_1(0)|^2 \right)}{2k_1^I} \left(\tanh \left(k_1^I h \right) + \frac{h k_1^I}{\cosh^2 \left(k_1^I h \right)} \right),
\end{aligned} \tag{A.10}$$

where $R_1(0)^*$ is the conjugate of $R_1(0)$.

Expanding ξ_2

Near $x = \infty$, we approximate ϕ by

$$\phi \approx T_\Lambda(0) e^{-\kappa_\Lambda(0)(x - l_\Lambda)} \frac{\cos \left(k_\Lambda(0)(z+h) \right)}{\cos \left(k_\Lambda(0) h \right)}, \tag{A.11}$$

and re-express as

$$\phi \approx T_\Lambda(0) e^{-i\kappa_\Lambda^I (x - l_\Lambda)}) \frac{\cosh \left(k_\Lambda^I (z+h) \right)}{\cosh \left(k_\Lambda^I h \right)}, \tag{A.12}$$

where $k_\Lambda^I = -\Im k_\Lambda(0)$ and $\kappa_\Lambda^I = -\Im \kappa_\Lambda(0)$, so that

$$\frac{\partial \phi}{\partial x} \approx -i\kappa_\Lambda^I T_\Lambda(0) e^{-i\kappa_\Lambda^I (x - l_\Lambda)}) \frac{\cosh \left(k_\Lambda^I (z+h) \right)}{\cosh \left(k_\Lambda^I h \right)}. \tag{A.13}$$

Therefore,

$$\xi_2 = \Im \int_{-h}^{0} \Bigg[(T_\Lambda(0) e^{-i\kappa_\Lambda^I (x-l_\Lambda)})(i\kappa_\Lambda^I T_\Lambda(0)^* e^{-i\kappa_\Lambda^I (x-l_\Lambda)}) \frac{\cosh^2\left(k_\Lambda^I (z+h)\right)}{\cosh^2\left(k_\Lambda^I h\right)} \Bigg] dz, \quad \text{(A.14)}$$

$$\begin{aligned} &= \frac{\kappa_\Lambda^I |T_\Lambda(0)|^2}{2\cosh^2\left(k_\Lambda^I h\right)} \left(\frac{1}{2k_\Lambda^I} \sinh\left(2k_\Lambda^I h\right) + h \right), \\ &= \frac{\kappa_\Lambda^I |T_\Lambda(0)|^2}{2k_\Lambda^I} \left(\tanh\left(k_\Lambda^I h\right) + \frac{k_\Lambda^I h}{\cosh^2\left(k_\Lambda^I h\right)} \right). \end{aligned} \quad \text{(A.15)}$$

Expanding ξ_3

The ice-covered boundary condition, (3.27), gives

$$\xi_3 = \Im \int_{-\infty}^{\infty} \left(\frac{\beta}{\alpha} \left(\frac{\partial^2}{\partial x^2} - k_y^2 \right)^2 - \gamma + \frac{1}{\alpha} \right) \frac{\partial \phi}{\partial z} \cdot \frac{\partial \phi^*}{\partial z} \bigg|_{z=0} dx. \quad \text{(A.16)}$$

Since $\dfrac{\partial \phi}{\partial z} \cdot \partial \phi^* \partial z$ is real,

$$\xi_3 = \Im \int_{-\infty}^{\infty} \left(\frac{\beta}{\alpha} \frac{\partial^2}{\partial x^2} \left(\frac{\partial^2}{\partial x^2} - 2k_y^2 \right)^2 \right) \frac{\partial \phi}{\partial z} \cdot \frac{\partial \phi^*}{\partial z} \bigg|_{z=0} dx.$$

Integration by parts gives

$$\xi_3 = \Im \Bigg[\left[\frac{\beta}{\alpha} \frac{\partial}{\partial x} \left(\frac{\partial^2}{\partial x^2} - 2k_y^2 \right) \frac{\partial \phi}{\partial z} \cdot \frac{\partial \phi^*}{\partial z} \right]_{-\infty}^{\infty} - \int_{-\infty}^{\infty} \frac{\beta}{\alpha} \frac{\partial}{\partial x} \left(\frac{\partial^2}{\partial x^2} - 2k_y^2 \right) \frac{\partial \phi}{\partial z} \cdot \frac{\partial}{\partial x} \frac{\partial \phi^*}{\partial z} dx \Bigg]. \quad \text{(A.17)}$$

As $2k_y^2 \dfrac{\partial}{\partial x} \dfrac{\partial \phi}{\partial z} \cdot \dfrac{\partial}{\partial x} \dfrac{\partial \phi^*}{\partial z}$ is real and by integration by parts, (A.17) becomes,

$$\xi_3 = \Im \Bigg[\left[\frac{\beta}{\alpha} \frac{\partial}{\partial x} \left(\frac{\partial^2}{\partial x^2} - 2k_y^2 \right) \frac{\partial \phi}{\partial z} \cdot \frac{\partial \phi^*}{\partial z} \right]_{-\infty}^{\infty} - \left[\frac{\beta}{\alpha} \frac{\partial^2}{\partial x^2} \frac{\partial \phi}{\partial z} \cdot \frac{\partial}{\partial x} \frac{\partial \phi^*}{\partial z} \right]_{-\infty}^{\infty} + \int_{-\infty}^{\infty} \frac{\beta}{\alpha} \frac{\partial^2}{\partial x^2} \frac{\partial \phi}{\partial z} \cdot \frac{\partial^2}{\partial x^2} \frac{\partial \phi^*}{\partial z} dx \Bigg]. \quad \text{(A.18)}$$

As $\frac{\partial^2}{\partial x^2}\frac{\partial \phi}{\partial z} \cdot \frac{\partial^2}{\partial x^2}\frac{\partial \phi^*}{\partial z}$ is real, (A.18) becomes

$$\xi_3 = \Im\left[\left[\frac{\beta}{\alpha}\frac{\partial}{\partial x}\left(\frac{\partial^2}{\partial x^2} - 2k_y^2\right)\frac{\partial \phi}{\partial z} \cdot \frac{\partial \phi^*}{\partial z}\right]_{-\infty}^{\infty} - \left[\frac{\beta}{\alpha}\frac{\partial^2}{\partial x^2}\frac{\partial \phi}{\partial z} \cdot \frac{\partial}{\partial x}\frac{\partial \phi^*}{\partial z}\right]_{-\infty}^{\infty}\right]. \tag{A.19}$$

Now breaking ξ_3 down,

$$\frac{\partial}{\partial x}\left(\frac{\partial^2}{\partial x^2} - 2k_y^2\right)\frac{\partial \phi(x_2,0)}{\partial z} \cdot \frac{\partial \phi(x_2,0)^*}{\partial z}$$

$$= \Big((-i\kappa_\Lambda^I)^3 k_\Lambda^I T_\Lambda(0) e^{-i\kappa_\Lambda^I(x-l_\Lambda)} \tanh(k_\Lambda^I h) - 2k_y^2(-i\kappa_\Lambda(0))k_\Lambda^I T_\Lambda(0) e^{-i\kappa_\Lambda^I(x-l_\Lambda)} \tanh(k_\Lambda^I h)\Big) \Big(k_\Lambda^I T_\Lambda(0)^* e^{i\kappa_\Lambda^I(x-l_\Lambda)} \tanh(k_\Lambda^I h)\Big),$$

$$= i\kappa_\Lambda^I (k_\Lambda^I)^2 \left((\kappa_\Lambda^I)^2 + 2k_y^2\right) \tanh^2(k_\Lambda^I h) |T_\Lambda(0)|^2.$$

$$\frac{\partial}{\partial x}\left(\frac{\partial^2}{\partial x^2} - 2k_y^2\right)\frac{\partial \phi(x_1,0)}{\partial z} \cdot \frac{\partial \phi(x_1,0)^*}{\partial z}$$

$$= \Big[i(\kappa_1^I)^3 k_1^I \left(e^{-i\kappa_1^I(x-r_1)} - R_1(0)e^{i\kappa_1^I(x-r_1)}\right)\tanh(k_1^I h) - 2ik_y^2\kappa_1^I k_1^I \left(-e^{-i\kappa_1^I(x-r_1)} + R_1(0)e^{i\kappa_1^I(x-r_1)}\right)\tanh(k_1^I h)\Big] \Big[k_1^I \left(e^{i\kappa_1^I(x-r_1)} + R_1(0)^* e^{-i\kappa_1^I(x-r_1))}\right)\tanh(k_1^I h)\Big],$$

$$= \Big[i\kappa_1^I k_1(0)((\kappa_1^I)^2 + 2k_y^2)\left(e^{-i\kappa_1^I(x-r_1)} - R_1(0)e^{i\kappa_1^I(x-r_1)}\right)\tanh(k_1^I h)\Big] \Big[k_1^I \left(e^{i\kappa_1^I(x-r_1)} + R_1(0)^* e^{-i\kappa_1^I(x-r_1))}\right)\tanh(k_1^I h)\Big],$$

$$= i\kappa_1^I (k_1^I)^2 \left((\kappa_1^I)^2 + 2k_y^2\right)\tanh^2(k_1^I h)\left(1 - |R_1(0)|^2\right).$$

$$\frac{\partial^2}{\partial x^2}\frac{\partial \phi(x_2,0)}{\partial z} \cdot \frac{\partial}{\partial x}\frac{\partial \phi^*}{\partial z}$$

$$= \left[-(\kappa_\Lambda^I)^2 k_\Lambda^I T_\Lambda(0) e^{-i\kappa_\Lambda^I (x-l_\Lambda)} \tanh\left(k_\Lambda^I h\right)\right] , \left[i\kappa_\Lambda^I k_\Lambda^I T_\Lambda(0)^* e^{i\kappa_\Lambda^I (x-l_\Lambda)} \tanh\left(k_\Lambda^I h\right)\right],$$

$$= -i(\kappa_\Lambda^I)^3 (k_\Lambda^I)^2 \tanh^2\left(k_\Lambda^I h\right) |T_\Lambda(0)|^2,$$

and finally,

$$\frac{\partial^2}{\partial x^1}\frac{\partial \phi(x_1,0)}{\partial z} \cdot \frac{\partial}{\partial x}\frac{\partial \phi^*}{\partial z}$$

$$= \left[-(\kappa_1^I)^2 k_1^I \left(e^{-i\kappa_1^I (x-r_1)} + R_1(0) e^{i\kappa_1^I (x-r_1)}\right) \tanh\left(k_1^I h\right)\right] \left[i\kappa_1^I k_1^I \left(e^{i\kappa_1^I (x-r_1)} - R_1(0) e^{-i\kappa_1^I (x-r_1)}\right) \tanh\left(k_1^I h\right)\right],$$

$$= -i(\kappa_1^I)^3 (k_1^I)^2 \tanh^2\left(k_1^I h\right) \left(1 - |R_1(0)|^2\right).$$

We can now express (A.19) as

$$\Im\left[\frac{\beta_\Lambda}{\alpha}\left[i\kappa_\Lambda^I (k_\Lambda^I)^2 \left((\kappa_\Lambda^I)^2 + 2k_y^2\right) \tanh^2\left(k_\Lambda^I h\right) |T_\Lambda(0)|^2\right] - \frac{\beta_1}{\alpha}\left[i\kappa_1^I (k_1^I)^2 \left((\kappa_1^I)^2 + 2k_y^2\right) \tanh^2\left(k_1^I h\right) \left(1 - |R_1(0)|^2\right)\right] - \frac{\beta_\Lambda}{\alpha}\left[-i(\kappa_\Lambda^I)^3 (k_\Lambda^I)^2 \tanh^2\left(k_\Lambda^I h\right) |T_\Lambda(0)|^2\right] + \frac{\beta_1}{\alpha}\left[-i(\kappa_1^I)^3 (k_1^I)^2 \tanh^2\left(k_1^I h\right) \left(1 - |R_1(0)|^2\right)\right]\right]$$

$$= \frac{\beta_\Lambda}{\alpha}\left[2\kappa_\Lambda^I (k_\Lambda^I)^2 ((\kappa_\Lambda^I)^2 + k_y^2) \tanh^2\left(k_\Lambda^I h\right) |T_\Lambda(0)|^2\right] - \frac{\beta_1}{\alpha}\left[2\kappa_1^I (k_1^I)^2 ((\kappa_1^I)^2 + k_y^2) \tanh^2\left(k_1^I h\right) (1 - |R_1(0)|^2)\right].$$

Solving the Energy Balance Equation

Pulling it all together, (A.3) becomes

$$\begin{aligned}\frac{\beta_\Lambda}{\alpha}\left[2\kappa_\Lambda^I(k_\Lambda^I)^2((\kappa_\Lambda^I)^2+k_y^2)\tanh^2(k_\Lambda^I h)|T_\Lambda(0)|^2\right]\\ -\frac{\beta_1}{\alpha}\left[2\kappa_1^I(k_1^I)^2((\kappa_1^I)^2+k_y^2)\tanh^2(k_1^I h)(1-|R_1(0)|^2)\right]\\ +\frac{\kappa_\Lambda^I|T_\Lambda(0)|^2}{2k_\Lambda^I}\left(\tanh(k_\Lambda^I h)+\frac{k_\Lambda^I h}{\cosh^2(k_\Lambda^I h)}\right)\\ -\frac{\kappa_1^I(1-|R_1(0)|^2)}{2k_1^I}\left(\tanh(k_1^I h)+\frac{hk_1^I}{\cosh^2(k_1^I h)}\right)=0.\end{aligned}$$

Re-arranging gives

$$\begin{aligned}\kappa_\Lambda^I\tanh(k_\Lambda^I h)\left(\frac{\beta_\Lambda}{\alpha}2(k_\Lambda^I)^2((\kappa_\Lambda^I)^2+k_y^2)\tanh(k_\Lambda^I h)\right.\\ \left.+\frac{1}{2k_\Lambda^I}+\frac{h}{2\sinh(k_\Lambda^I h)\cosh(k_\Lambda^I h)}\right)|T_\Lambda(0)|^2\end{aligned}$$

$$\begin{aligned}-\kappa_1^I\tanh(k_1^I h)\left(\frac{\beta_1}{\alpha}2(k_1^I)^2((\kappa_1^I)^2+k_y^2)\tanh(k_1^I h)\right.\\ \left.+\frac{1}{2it}+\frac{h}{2\sinh(k_1^I h)\cosh(k_1^I h)}\right)(1-|R_1(0)|^2)=0\end{aligned}$$

which can be expressed as

$$\mathcal{D}|T_\Lambda(0)|^2+|R_1(0)|^2=1, \tag{A.20}$$

where D is given by

$$\begin{aligned}\mathcal{D}=\left(\frac{\kappa_\Lambda^I k_1^I\cosh^2(k_1^I h)}{\kappa_1^I k_\Lambda^I\cosh^2(k_\Lambda^I h)}\right)\\ \left(\frac{\frac{\beta_\Lambda}{\alpha}4(k_\Lambda^I)^3((\kappa_\Lambda^I)^2+k_y^2)\sinh^2(k_\Lambda^I h)+\frac{1}{2}\sinh(2k_\Lambda^I h)+k_\Lambda^I h}{\frac{\beta_1}{\alpha}4(k_1^I)^3((\kappa_1^I)^2+k_y^2)\sinh^2(k_1^I h)+\frac{1}{2}\sinh(2k_1^I h)+k_1^I h}\right)\end{aligned} \tag{A.21}$$

B

Deriving $|T_{av}|^2$

In this appendix, we solve $|T_{av}|^2$ via complex integration and the residue theorem. This solution is part of the derivation of the approximation theory presented in Chapter 9. The intention of the theory is to approximate an attenuation coefficient for multiple plates and is an extension of the theory presented in Meylan and Squire (1993).

Firstly,

$$|T|^2 = \frac{|T_{wp}T_{pw}e^{k_2(0)(l-r)}|^2}{|1 - R_{pw}^2 e^{2k_2(0)(l-r)}|^2}. \tag{B.1}$$

Rearranging gives

$$|T|^2 = |T_{wp}T_{pw}|^2 \frac{1}{|1 - |R_{pw}^2|e^{2(k_2(0)(l-r)+ir_{pw})}|^2}, \tag{B.2}$$

where $|e^{k_2(0)(l-r)}| = 1$ and $R_{pw} = |R_{pw}|e^{ir_{pw}}$. Since $|z|^2 = zz^*$,

$$|T|^2 = |T_{wp}T_{pw}|^2 \frac{1}{(1 - |R_{pw}^2|e^{it})(1 - |R_{pw}^2|e^{it})^*}, \tag{B.3}$$

where $it = 2(k_2(0)(l-r) + ir_{pw})$. Expanding gives

$$|T|^2 = |T_{wp}T_{pw}|^2 \frac{1}{1 + |R_{pw}^2|^2 - |R_{pw}^2|(e^{it} + e^{-it})}. \tag{B.4}$$

The average of $|T|^2$ can be found by integrating over one period and then dividing by the length of one period i.e.

$$|T_{av}|^2 = \frac{1}{2\pi}\int_0^{2\pi} |T|^2 dt = \frac{|T_{wp}T_{pw}|^2}{2\pi}\int_0^{2\pi} \frac{1}{1 + |R_{pw}^2|^2 - |R_{pw}^2|(e^{it} + e^{-it})} dt. \tag{B.5}$$

To solve, we let $z = e^{it}$, so $dz = ie^{it}dt$ which gives

$$|T_{av}|^2 = \frac{|T_{wp}T_{pw}|^2}{2\pi i}\oint_{|z|=1} \frac{1}{z(1 + |R_{pw}^2|^2 - |R_{pw}^2|(z + z^{-1}))} dz. \tag{B.6}$$

Factorising via the quadratic formula gives

$$|T_{av}|^2 = \frac{|T_{wp}T_{pw}|^2}{2\pi i}\oint_{|z|=1} \frac{1}{\left(z - |R_{pw}^2|\right)\left(-|R_{pw}^2|z + 1\right)} dz, \tag{B.7}$$

which gives two simple poles. Only the pole at $z = |R_{pw}^2|$ is within the contour $|z| = 1$. Therefore, by the residue theorem

$$|T_{av}|^2 = \frac{|T_{wp}T_{pw}|^2}{2\pi i} 2\pi i \mathrm{Res}_{z=|R_{pw}^2|}, \tag{B.8}$$

which gives

$$|T_{av}|^2 = \frac{|T_{wp}T_{pw}|^2}{1 - |R_{pw}^2|}, \tag{B.9}$$

since $\mathrm{Res}_{z=|R_{pw}^2|} = -|R_{pw}^2|^2 + 1$.

C

The Attenuation Data

In this appendix, we simply list all the attenuation data used in this thesis. Each table includes the raw attenuation data from the experiments, the scaled attenuation data from the experiments and the attenuation coefficients from our model.

Table C.1: Comparison of the attenuation coefficients from the 4^{th} of September 1979 Greenland Sea experiment ($\breve{a}$) (obtained from Wadhams et al. (1988)), the scaled attenuation coefficients and the model attenuation coefficients (a). The $\pm$ values given represent the margin of error provided in Wadhams et al. (1988).

$\mathcal{T}$	$\breve{a}$ $(m^{-1} \times 10^{-4})$	$\breve{a}\times$ 65/.3 $(\times 10^{-2})$	a $(\times 10^{-2})$
8.14	2.66 ± 0.22	5.76 ± 0.48	9.22
9.10	2.01 ± 0.17	4.35 ± 0.37	7.29
10.31	1.23 ± 0.19	2.67 ± 0.41	4.92
11.88	0.73 ± 0.25	1.58 ± 0.54	2.77
14.03	0.29 ± 0.27	0.63 ± 0.59	1.02

Table C.2: Comparison of the attenuation coefficients from the 10^{th} of September 1979 Greenland Sea experiment ($\breve{a}$) (obtained from Wadhams et al. (1988)), the scaled attenuation coefficients and the model attenuation coefficients (a). The $\pm$ values given represent the margin of error provided in Wadhams et al. (1988).

$\mathcal{T}$	$\breve{a}$ $(m^{-1} \times 10^{-4})$	$\breve{a}\times$ $80/0.17$ $(\times 10^{-2})$	a $(\times 10^{-2})$
6.73	2.01 ± 1.46	9.46 ± 6.87	19.58
7.37	2.37 ± 1.46	11.15 ± 6.87	13.37
8.14	2.35 ± 0.54	11.06 ± 2.54	11.54
9.10	1.29 ± 0.13	6.07 ± 0.61	9.43
10.31	1.25 ± 0.28	5.88 ± 1.32	5.91
11.88	0.89 ± 0.46	4.19 ± 2.16	2.77

Table C.3: Comparison of the attenuation coefficients from the 7^{th} of February 1983 Bering Sea experiment 1. ($\breve{a}$) (obtained from Wadhams et al. (1988)), the scaled attenuation coefficients and the model attenuation coefficients (a). The $\pm$ values given represent the margin of error provided in Wadhams et al. (1988).

$\mathcal{T}$	$\breve{a}$ $(m^{-1} \times 10^{-4})$	$\breve{a}\times$ $14.5/0.72$ $(\times 10^{-2})$	a $(\times 10^{-2})$
6.99	3.57 ± 0.18	0.72 ± 0.04	2.60
7.35	4.28 ± 0.25	0.86 ± 0.05	2.54
7.81	4.66 ± 0.81	0.94 ± 0.16	1.71
8.26	3.66 ± 1.16	0.74 ± 0.23	1.16
8.77	2.84 ± 0.65	0.57 ± 0.13	0.77
9.43	2.05 ± 0.03	0.41 ± 0.01	0.50
10.10	0.75 ± 0.19	0.15 ± 0.04	0.26
10.87	0.20 ± 0.05	0.04 ± 0.01	0.15
11.90	0.55 ± 0.31	0.11 ± 0.06	0.05
12.99	0.34 ± 0.26	0.07 ± 0.05	0.02

Table C.4: Comparison of the attenuation coefficients from the 7^{th} of February 1983 Bering Sea experiment 2. ($\breve{a}$) (obtained from Wadhams et al. (1988)), the scaled attenuation coefficients and the model attenuation coefficients (a). The $\pm$ values given represent the margin of error provided in Wadhams et al. (1988).

$\mathcal{T}$	$\breve{a}$ $(m^{-1} \times 10^{-4})$	$\breve{a}\times$ $14.5/0.72$ $(\times 10^{-2})$	a $(\times 10^{-2})$
6.99	7.87 ± 2.67	2.597 ± 0.54	2.60
7.35	8.41 ± 1.02	2.538 ± 0.21	2.54
7.81	8.17 ± 0.59	1.710 ± 0.12	1.71
8.26	6.95 ± 0.81	1.156 ± 0.16	1.16
8.77	5.79 ± 1.48	0.771 ± 0.30	0.77
9.43	3.76 ± 1.33	0.499 ± 0.27	0.50
10.10	2.81 ± 0.64	0.263 ± 0.13	0.26
10.87	2.53 ± 0.80	0.155 ± 0.16	0.15
11.90	1.89 ± 0.34	0.049 ± 0.07	0.05

Table C.5: Comparison of the attenuation coefficients from the 20^{th} of February 1983 Bering Sea experiment ($\breve{a}$) (obtained from Wadhams et al. (1988)), the scaled attenuation coefficients and the model attenuation coefficients (a). The $\pm$ values given represent the margin of error provided in Wadhams et al. (1988).

$\mathcal{T}$	$\breve{a}$ $(m^{-1} \times 10^{-4})$	$\breve{a}\times$ $100/0.2$ $(\times 10^{-2})$	a $(\times 10^{-2})$
9.17	0.65 ± 1.28	3.25 ± 6.40	4.19
9.80	1.44 ± 0.94	7.20 ± 4.70	3.31
10.64	0.81 ± 0.30	4.05 ± 1.50	2.12
11.49	0.36 ± 0.39	1.80 ± 1.95	1.40
12.66	0.33 ± 0.63	1.65 ± 3.15	0.65
13.89	0.38 ± 0.24	1.90 ± 1.20	0.30
15.63	0.20 ± 0.82	1.00 ± 4.10	0.07

Table C.6: Comparison of the attenuation coefficients from the 22^{nd} of February 1983 Bering Sea experiment ($\breve{a}$) (obtained from Wadhams et al. (1988)), the scaled attenuation coefficients and the model attenuation coefficients (a). The $\pm$ values given represent the margin of error provided in Wadhams et al. (1988).

$\mathcal{T}$	$\breve{a}$ $(m^{-1} \times 10^{-4})$	$\breve{a}\times$ $100/0.2$ $(\times 10^{-2})$	a $(\times 10^{-2})$
9.17	1.04 ± 0.15	5.20 ± 0.75	4.19
9.80	1.12 ± 0.12	5.60 ± 0.60	3.31
10.64	1.23 ± 0.22	6.15 ± 1.10	2.12
11.49	1.06 ± 0.23	5.30 ± 1.15	1.40
12.66	0.84 ± 0.21	4.20 ± 1.05	0.65
13.89	0.68 ± 0.12	3.40 ± 0.60	0.30
15.63	0.18 ± 0.17	0.90 ± 0.85	0.07
17.54	0.22 ± 0.09	1.10 ± 0.45	0.02

Table C.7: Comparison of the attenuation coefficients from the 26^{th} of February 1983 Bering Sea experiment ($\breve{a}$) (obtained from Wadhams et al. (1988)), the scaled attenuation coefficients and the model attenuation coefficients (a). The $\pm$ values given represent the margin of error provided in Wadhams et al. (1988).

$\mathcal{T}$	$\breve{a}$ $(m^{-1} \times 10^{-4})$	$\breve{a}\times$ $100/0.2$ $(\times 10^{-2})$	a $(\times 10^{-2})$
9.17	0.16 ± 0.04	8.00 ± 0.20	4.19
9.80	0.27 ± 0.08	1.35 ± 0.40	3.31
10.64	0.48 ± 0.07	2.40 ± 0.35	2.12
11.49	0.36 ± 0.08	1.80 ± 0.40	1.40
12.66	0.24 ± 0.07	1.20 ± 0.35	0.65
13.89	0.19 ± 0.04	0.95 ± 0.20	0.30
15.63	0.11 ± 0.03	0.55 ± 0.15	0.07
17.54	0.10 ± 0.03	0.50 ± 0.15	0.02
20.41	0.10 ± 0.06	0.50 ± 0.30	0.01

Table C.8: Comparison of the attenuation coefficients from the 26^{th} of July 1983 Greenland Sea experiment ($\breve{a}$) (obtained from Wadhams et al. (1988)), the scaled attenuation coefficients and the model attenuation coefficients (a). The $\pm$ values given represent the margin of error provided in Wadhams et al. (1988).

$\mathcal{T}$	$\breve{a}$ $(m^{-1} \times 10^{-4})$	$\breve{a}\times$ $55/0.5$ $(\times 10^{-2})$	a $(\times 10^{-2})$
7.76	7.39 ± 1.46	8.13 ± 1.61	14.52
8.35	8.72 ± 0.92	9.59 ± 1.01	12.41
9.23	7.35 ± 0.90	8.08 ± 0.99	9.23
10.31	6.48 ± 1.05	7.13 ± 1.16	6.32
11.68	4.86 ± 0.79	5.35 ± 0.87	4.24
13.47	2.87 ± 0.19	3.16 ± 0.21	2.18
15.90	1.98 ± 0.20	2.18 ± 0.22	0.74

Table C.9: Comparison of the attenuation coefficients from the 29^{th} of July 1983 Greenland Sea experiment ($\breve{a}$) (obtained from Wadhams et al. (1988)), the scaled attenuation coefficients and the model attenuation coefficients (a). The $\pm$ values given represent the margin of error provided in Wadhams et al. (1988).

$\mathcal{T}$	$\breve{a}$ $(m^{-1} \times 10^{-4})$	$\breve{a}\times$ $65/0.5$ $(\times 10^{-2})$	a $(\times 10^{-2})$
8.35	3.86 ± 0.55	5.02 ± 0.72	12.41
9.23	1.42 ± 0.21	1.85 ± 0.27	9.23
10.31	0.54 ± 0.05	0.70 ± 0.07	6.32

Table C.10: Comparison of the attenuation coefficients from the 24^{th} of March 2003 Bellinghausen Sea experiment 323 ($\breve{a}$) (Hayes et al., 2007), the scaled attenuation coefficients and the model attenuation coefficients (a). The $\pm$ values given represent the margin of error provided in Wadhams et al. (1988).

$\mathcal{T}$	$\breve{a}$ $(m^{-1} \times 10^{-4})$	$\breve{a}\times$ $20/0.6$ $(\times 10^{-2})$	a $(\times 10^{-2})$
5.26	5.50 ± 2.67	1.83 ± 0.89	6.06
6.08	6.10 ± 2.65	2.03 ± 0.88	4.23
7.19	7.76 ± 1.36	2.59 ± 0.45	2.37
8.79	5.76 ± 1.23	1.92 ± 0.41	0.59
11.31	2.92 ± 7.81	0.97 ± 0.26	0.07
15.88	1.47 ± 7.52	0.49 ± 0.25	0.00
26.60	1.44 ± 1.33	0.48 ± 0.44	0.00

Table C.11: Comparison of the attenuation coefficients from the 25^{th} of March 2003 Bellinghausen Sea experiment 324 ($\breve{a}$) (Hayes et al., 2007), the scaled attenuation coefficients and the model attenuation coefficients (a). The $\pm$ values given represent the margin of error provided in Wadhams et al. (1988).

$\mathcal{T}$	$\breve{a}$ $(m^{-1} \times 10^{-4})$	$\breve{a}\times$ $20/0.8$ $(\times 10^{-2})$	a $(\times 10^{-2})$
5.26	12.6 ± 15.1	3.15 ± 3.78	23.61
6.08	18.3 ± 15.5	4.58 ± 3.88	13.21
7.19	7.83 ± 5.21	1.96 ± 1.30	7.72
8.79	9.77 ± 2.27	2.44 ± 0.57	3.29
11.31	7.59 ± 1.00	1.90 ± 0.25	1.12
15.88	4.59 ± 1.05	1.15 ± 0.26	0.01
26.60	2.63 ± 1.57	0.66 ± 0.39	0.00

Table C.12: The attenuation coefficients from our model (a), the measured attenuation coefficients ($\breve{a}$) and the scaled measured attenuation coefficients from the 25^{nd} March 2003 Bellinghausen Sea experiment 324 on exiting the ice.

$\mathcal{T}$	$\breve{a}$ $(m^{-1} \times 10^{-4})$	$\breve{a}\times$ $20/0.8$ $(\times 10^{-2})$	a $(\times 10^{-2})$
5.26	25.3 ± 32.9	6.33 ± 8.23	23.61
6.08	22.4 ± 18.9	5.60 ± 4.73	13.21
7.19	14.3 ± 8.26	3.58 ± 2.01	7.72
8.79	14.9 ± 3.1	3.73 ± 0.78	3.29
11.31	11.9 ± 3.18	2.98 ± 0.80	1.12
15.88	5.42 ± 3.34	1.36 ± 0.84	0.01
26.60	7.06 ± 4.51	1.77 ± 1.13	0.00